SOLUTION-BASED AND SOLUTION COMBUSTION-BASED PROCESSING TECHNIQUES FOR METALLIC AND METAL OXIDE THIN FILMS FOR OPTOELECTRONIC APPLICATIONS

Thesis

Submitted in partial fulfilment of the requirements for the degree of

DOCTOR OF PHILOSOPHY

By

PAVAN PUJAR

(Registration No: 155013MT15F03)

DEPARTMENT OF METALLURGICAL AND MATERIALS
ENGINEERING
NATIONAL INSTITUTE OF TECHNOLOGY KARNATAKA
SURATHKAL

September, 2019

D E C L A R A T I O N

I hereby *declare* that the Research Thesis entitled "**Solution-based and solution combustion-based processing techniques for metallic and metal oxide thin films for optoelectronic applications**" which is being submitted to the National Institute of Technology Karnataka, Surathkal in partial fulfillment of the requirements for the award of the Degree of **Doctor of Philosophy** in the Department of **Metallurgical and Materials Engineering**, is a *bonafide report of the research work carried out by me*. The material contained in this Research Thesis has not been submitted to any University or Institution for the award of any degree.

PAVAN PUJAR

Registration number: 155013MT15F03

Department of Metallurgical and Materials Engineering

Place: NITK, Surathkal

Date:

CERTIFICATE

This is to certify that the Research Thesis entitled "**Solution-based and solution combustion-based processing techniques for metallic and metal oxide thin films for optoelectronic applications**" submitted by Mr. Pavan Pujar (Register Number: 155013MT15F03) as the record of the research work carried out by him, is *accepted as the Research Thesis submission* in partial fulfillment of the requirements for the award of degree of Doctor of Philosophy.

Research Supervisors

Dr. Saumen Mandal

Assistant Professor

Department of Metallurgical and

Materials Engineering

NITK Surathkal

Dr. Dipti Gupta

Associate Professor

Department of Metallurgical

Engineering and Materials Science

IIT Bombay

Chairman- DRPC

DEDICATED TO
THE ALMIGHTY GOD…

I am thankful to all teaching and non-teaching staff of the Department of Metallurgical and Materials Engineering, National Institute of Technology Karnataka Surathkal for constant support and help in various aspects of my course. Special thanks to Mrs. Sharmila Dinesh for helping me in necessary documentation at various stages of Ph.D. I extend my special thanks to Ms. Rashmi Banjan for her support in conducting Scanning Electron Microscopic studies.

Finally, I thank all those who directly and indirectly helped me to complete the Ph.D. research work.

PAVAN PUJAR

NITK Surathkal

ABSTRACT

Despite the enormous dependency of human life on silicon-based electronic devices, there exists a constant urge for new materials and processing techniques for targeted applications. The specific areas demanding mechanical flexibility and optical transparency in the devices require a new set of materials and processing methodologies; thin films of metal oxides are of one such category of materials depicting the properties mentioned above. In the present study, a series of functional metal oxides along with their applications in Thin Film Transistors (TFTs) is addressed. Initially, two distinct transparent conducting oxides, namely, titanium-doped indium oxide (ITiO: $In_{14}TiO_{23}$) and zinc and tin co-doped indium oxide (IZTO: $In_{1.4}Sn_{0.3}Zn_{0.3}O_3$) are fabricated at low temperatures using solution combustion technique. The method involves molecular precursors of fuel, oxidizer and the exothermicity of the reaction between them. The film of IZTO deposited via low-temperature (200 °C) solution combustion is found to be electrically conductive (10^2 Scm^{-1}) and optically transparent (~83 %) in the visible spectrum. Similarly, thin films of ITiO have shown an electrical conductivity of 20 Scm^{-1} and optical transparency of ~100 %. However, the molecular precursor-based depositions are advantageous over nano-dispersion based ones. The morphological irregularities of the films deposited via nano-dispersions is addressed by a simple technique of tailoring the dwell-time: the time-elapse between the drop-casting and the thermal annealing. A uniform silver deposit is achieved at a temperature of 200 °C with a dwell-time of 10 min. Also, spraying of combustible precursors of silver resulted in the uniform and electrically conductive (10^7 Sm^{-1}) films at 160 °C.

The applications of transparent and conducting IZTO as a gate electrode with pentacene-semiconductor has shown saturation mobility (μ_{sat}), on:off ratio ($I_{on}:I_{off}$), and the threshold voltage (V_{th}) of 0.44 $cm^2V^{-1}s^{-1}$, 10^3 and -12.5 V respectively. In addition, the fuel-free solution combustion is realized in fabricating thin film of semiconducting IZTO ($In_4Sn_4ZnO_{15}$) at 200 °C. The TFTs with SiO_2 dielectric and IZTO (~45 nm) semiconductor has shown μ_{sat}, $I_{on}:I_{off}$, and the V_{th} of 0.50 ± 0.02 cm^2 V^{-1} s^{-1}, 1.25 × 10^4

and 6.6 ± 0.79 V respectively. In addition, the voltage operation (< 3 V) is realized by replacing conventional SiO_2 by ~106 nm thick solution processed high dielectric permittivity (~21) sodium β-alumina and the TFTs have revealed a μ_{sat}, $I_{on}:I_{off}$ and V_{th} of 4.21 ± 0.18 cm^2 V^{-1} s^{-1}, 1.4×10^2 and 0.47 ± 0.08 V respectively.

CONTENTS

Page left intentionally blank

NOMENCLATURE

a:Si-H	:	Amorphous hydrogenated silicon
Ac	:	Acetylacetone
AFM	:	Atomic Force Microscopy
t	:	Annealing time
BGTC	:	Bottom Gate Top Contact
e	:	Charge of an electron
N	:	Carrier concentration
C.T	:	Compatibility triangle
C	:	Capacitance
ΔH	:	Change in enthalpy
η	:	Combustion efficiency
κ	:	Dielectric constant
DC	:	Direct Current
DSC	:	Differential Scanning Calorimetry
DTA	:	Differential Thermal Analysis
DFT	:	Density Functional Theory
σ	:	Electrical conductivity
m*	:	Effective mass of a charge carrier
ρ	:	Electrical resistivity
ϕ	:	Fuel to Oxidizer ratio
C_{SS}	:	Fraction of solid-solid interface
C_{SV}	:	Fraction of solid-vapor interface
FESEM	:	Field Emission Gun-Scanning Electron Microscope
K	:	Grain growth parameter
G	:	Grain size after annealing
K_{SS}	:	Grain growth parameter of solid-solid interface
K_{SV}	:	Grain growth parameter of solid-vapor interface
GIAXRD	:	Grazing Incidence Angle X-Ray Diffraction
μ_H	:	Hall mobility

ITO	:	Indium Tin Oxide
ITiO	:	Indium Titanium Oxide
IZTO	:	Indium Zinc Tin Oxide
IGZO	:	Indium Gallium Zinc Oxide
LTPS	:	Low Temperature Polycrystalline Silicon
LNO	:	Lithium doped Nickel Oxide
μ_c	:	Mobility of charge carriers
MOS	:	Metal Oxide Semiconductor
2-ME	:	2-Methoxyethanol
$I_{on}{:}I_{off}$	:	On:off ratio
V_O	:	Operating voltage
OV	:	Oxidizing Valency
G_o	:	Original grain size
λ_p	:	Plasma wavelength
ε_o	:	Permittivity of free space
PLD	:	Pulsed Laser Deposition
T_P	:	Processing temperature
τ	:	Relaxation time
R.F	:	Radio Frequency
RV	:	Reducing Valency
SAM	:	Self-assembled monolayer
μ_{sat}	:	Saturation mobility
V_{th}	:	Threshold voltage
d	:	Thickness of the dielectric
TFT	:	Thin Film Transistor
TCO	:	Transparent Conducting Oxide
TGA	:	Thermogravimetric Analysis
TEM	:	Transmission Electron Microscopy
υ	:	Valency of a metal cation
XRD	:	X-Ray Diffraction
XPS	:	X-ray Photoelectron Spectroscopy

Page left intentionally blank

Page left intentionally blank

CHAPTER 1

INTRODUCTION

Silicon-based electronic industries have evolved with time. The importance of silicon in modern electronics is tremendous and forms the building block of transistors, complementary circuits, sensor-arrays, flat-panel displays etc. The use of silicon in various applications made it more attractive and it is continuously gaining importance due to increased human dependency on electronic gadgets. Apart from the popularity of silicon, there are challenges in specialized applications, where mechanical flexibility and optical transparency in the devices are desired. Owing to its brittleness and opaqueness, the application of the silicon is limited. Also, the urge for large area electronic gadgets such as flat-panel displays calls for an additional challenge to single crystal silicon. Either the entire panel embodies single crystal silicon or the assemblage of many single crystals, the former faces challenge during the fabrication and the latter increases the cost of the product. Thus, there is a constant drag for low-cost, high-throughput processes added with the search for new functional materials, which are optically transparent and mechanically flexible as well.

Alternative materials satisfying the requirement of mechanical flexibility fall in the category of organics. After the discovery of conducting polymers the new area - 'organic electronics' grabbed enormous popularity. The mechanically flexible, readily processable, low-cost devices based on active organic materials have got severe challenges, considering electronic properties and environmental stability. Thus, the applications of organic electronics are limited to organic light emitting diodes and sensors. A constant search of alternate materials has revealed possibilities in inorganics, especially oxides of transition metal cations. Owing to high band-gaps (> 3 eV) of metal oxides, they are optically transparent and electrically insulative in their thin film forms. However, the tunable defect chemistry of metal oxides provides a luxury of maintaining desired charge concentration leading to conducting/semiconducting behaviour (Facchetti and Marks 2010). Also, the transition metal cation-based oxides depict high

spatial distribution of s-orbitals leading to an unaltered percolation of charge carriers even in their amorphous forms. The metal oxides with transition metal cations such as indium oxide, tin oxide, zinc oxide, gallium oxides and combinations thereof are few such examples depicting s-orbital transport of charge carriers (Nomura et al. 2004). With the advantages such as large area deposition and low-cost processing, amorphous metal oxides gained great scientific attention resulting in commercialization by leading electronic industries such as TOSHIBA, SHARP, LG, DELL and so on (Wager 2016). In addition, the transparent and conducting metal oxide thin films such as tin doped indium oxide (ITO) have been employed in touch surfaces of the mobile phones, energy efficient windows and solar cells.

Currently, the fabrication of thin films of functional metal oxides is accomplished by high-vacuum, capital intensive evaporative techniques. There exists a constant drag for the development of low-cost, simple deposition techniques with retained electronic properties. A possible remedy for the same is 'solution processing' (Pasquarelli et al. 2011), where a precursor solution comprising of metal salts, stabilizers is deposited onto the substrate of interest using various low-cost, simple techniques such as spin coating, spray coating, inkjet printing, dip coating etc. The subsequent thermal processing of the as-deposited films results in the elimination of undesired organic ligands leaving behind a dense, continuous and uniform metal oxide thin film (Pasquarelli et al. 2011). A thumb rule in choosing the temperature of processing is mainly guided by the decomposition temperatures of the constituents. The minimum temperature of processing turns out to be 400 °C, which is incompatible with the thermal sensitive substrates (Kang et al. 2014). The reduction in the processing temperature can be accomplished by the technique called 'solution combustion', where the exothermic reaction between a fuel and an oxidizer is utilized with a minimum supplied heat input (Kim et al. 2011b; Patil et al. 2008a). The additional advantages of solution combustion embody the compositional tunability, low processing temperature and time. Another variant in the solution processing is the usage of colloidal solution loaded with nanoparticles of the desired material. The evaporation of the colloidal solution results in the formation of the film due to the sintering of nanoparticles under the supplied thermal energy (Pasquarelli et al. 2011). But the process has an additional

challenge regarding the morphological development of the film. The evaporation of the solvent guides the movement of nanoparticles within the deposited drop, which lead to undesired coffee-ring (Deegan et al. 1997) or center deposit (Hu and Larson 2006). Thus, it is crucial to design proper film deposition parameters.

Further, the various functional materials form components of the transistor are being utilized in their thin film forms. The thin film transistors (TFTs) are the electronic switches and current amplifiers used to control or amplify the flow of electric current. The thin films of functional materials such as semiconductors, conductors, and the dielectrics are the building blocks of the TFTs. The present thesis is not only limited to the new functional materials but also for the fabrication of the same by employing low-temperature solution combustion technique. Transparent conducting oxides (TCOs) such as titanium-doped indium oxide (ITiO: $In_{14}TiO_{23}$), zinc and tin co-doped indium oxide (IZTO: $In_{1.4}Sn_{0.3}Zn_{0.3}O_3$) are developed at the low processing temperatures. Also, the feasibility of solution combustion processing is extended to the fabrication of metallic-silver films. As an extension, the simplest way of achieving uniform deposition through the colloidal solution of silver is accomplished. Also, the compositionally distinct thin film of semiconducting amorphous zinc and tin co-doped indium oxide (a-IZTO: $In_4Sn_4ZnO_{15}$) is fabricated and characterized. Further, the applications of functional metal oxides in TFTs as (a) gate electrode and the (b) active layer are analysed. Finally, the low voltage operation of the TFTs comprising a-IZTO and β-phase of sodium incorporated alumina (sodium β-alumina) as an active and the passive dielectric layers is addressed. The following paragraph explains the flow of the thesis.

CHAPTER 2 deals with existing literature in the area of the research. **CHAPTER 3** is dedicated to the low-temperature fabrication of two TCOs, namely ITiO ($In_{14}TiO_{23}$) and IZTO ($In_{1.4}Sn_{0.3}Zn_{0.3}O_3$). **CHAPTER 4** addresses the challenges and possible solution to overcome the morphological irregularities. It also addresses the utilization of aqueous based combustible precursors in depositing metallic-silver films. **CHAPTER 5** is dedicated to the fabrication and characterization of thin films of semiconducting a-IZTO and the applications of both conducting and semiconducting

3

IZTO in the TFTs. Finally, **CHAPTER 6** is devoted to the conclusion and the future scope of the present study.

CHAPTER 2

LITERATURE REVIEW

2.1 Introduction

The current demand in the functional electronic materials is concerned mainly on the new conducting, semiconducting, and dielectric materials, which are readily processable with facile techniques. Presently, silicon is the building block of almost all electronic devices, owing to its high carrier mobility it is the first choice as an active component in TFTs and solar cells. Due to opaqueness and brittleness of the silicon, it fails to serve the desired purpose of device transparency and mechanical flexibility. Especially in the case of components of TFTs, there is a great opportunity for different materials with simple and economical processing techniques. The materials used as the active and passive components of the TFTs need to be transparent and electronically robust, under mechanical bending stresses. Forthcoming sections of the present chapter are dedicated to the selection of materials as different components of TFTs and processing techniques. Before the core discussion on the details of materials and processing techniques, a brief introduction with the history of TFTs is worth elucidating.

2.2 Thin Film Transistors

Transistors are the oldest electronic devices having a long history of around 80 years. The concept of the working principle of transistors was patented in 1930 by J.E. Lilienfeld (Edgar 1930). The first patent on the transistor was the concept, and presently it is known as the Metal-Semiconductor-Field-Effect-Transistor (MESFET). After three years of the first conceptual patent in 1930, so-called Metal-Insulator-Semiconductor-Field-Effect-Transistor (MISFET) had come into limelight, which proposed the design of the device with copper sulfide as the semiconducting material sandwiched between aluminum oxide-insulator and the aluminum-electrode (Edgar 1933). The reported designs of MESFET and MISFET have presented in Appendix I,

fig. I-a. The above patents were initial discoveries, but due to unavailability of adequate materials and the processing techniques, it took several years to produce the first TFT, which was based on cadmium sulfide semiconductor and reported by RCA laboratories (Weimer 1962). The architecture of the proposed TFT was comprised of polycrystalline n-type cadmium sulfide placed between the silicon monoxide-insulator and the gold-contact electrodes. The films of the TFTs were deposited using vacuum based techniques and the resulting characteristics of the TFTs were termed as 'beautiful characteristics' (Weimer 1962) and got tremendous recognition worldwide through IEEE proceedings. The device architecture and the output characteristics of the first TFT by Weimer are shown in Appendix I, fig. I-b. By this time, from the work of Weimer on cadmium sulfide, it was known that the semiconductor is something which can achieve a modulated electrical conductivity due to the induced charges, and electrode contacts on it can measure the current flowing through it. Further, cadmium selenide-based devices were demonstrated by Weimer.

Post these successful events, metal oxides such as tin oxide (SnO_2), and zinc oxide (ZnO) were tested for their semiconducting action in the TFTs. SnO_2 was used in TFTs along with aluminum oxide (Al_2O_3) as an insulator and aluminum as electrode (Klasens and Koelmans 1964). Further, the lithium doped ZnO was used as the semiconductor with evaporated silicon oxide (SiO_x)-insulating layer with aluminum-electrode (Boesen and Jacobs 1968). The performance was poor in the case of ZnO and SnO_2 based TFTs, after several years of trials the best performance of TFTs with antimony-doped SnO_2 (Prins et al. 1996) and indium oxide (In_2O_3) (Seager et al. 1996) was obtained. After these innovations and achievements in the device performance, several new technologies concerning improvement in the device architecture, performance was reported. Some of which are: (a) use of radio frequency (R.F) sputtering to deposit ZnO thin films at room temperature without compromising with the performance (Carcia et al. 2003), (b) adopting nanowires of ZnO and SnO_2 as active layers of TFTs (Fan et al. 2004; Zhang et al. 2003), (c) vacuum-free techniques for the deposition of the thin films of ZnO (Norris et al. 2003). In recent years, multi-component metal oxides have been reported with improved performance parameters such as saturation mobility, the on:off ratio, and threshold voltage. Indium Gallium

Zinc Oxide (IGZO) is the most widely accepted among all amorphous multi-component metal oxide semiconductors. The maximum saturation mobility obtained in the case of IGZO is nearly 80 $cm^2V^{-1}s^{-1}$ with on:off ratio of ~10^7, which is first reported in the year 2004 (Nomura et al. 2004). Apart from amorphous metal oxide semiconductors, a series of semiconducting materials such as hydrogenated amorphous silicon (a:Si-H) and organic molecule etc., are reported in the literature. Fig. 2.1 shows the milestones achieved in TFTs right from its first invention to the current high-performance transparent TFTs based on IGZO.
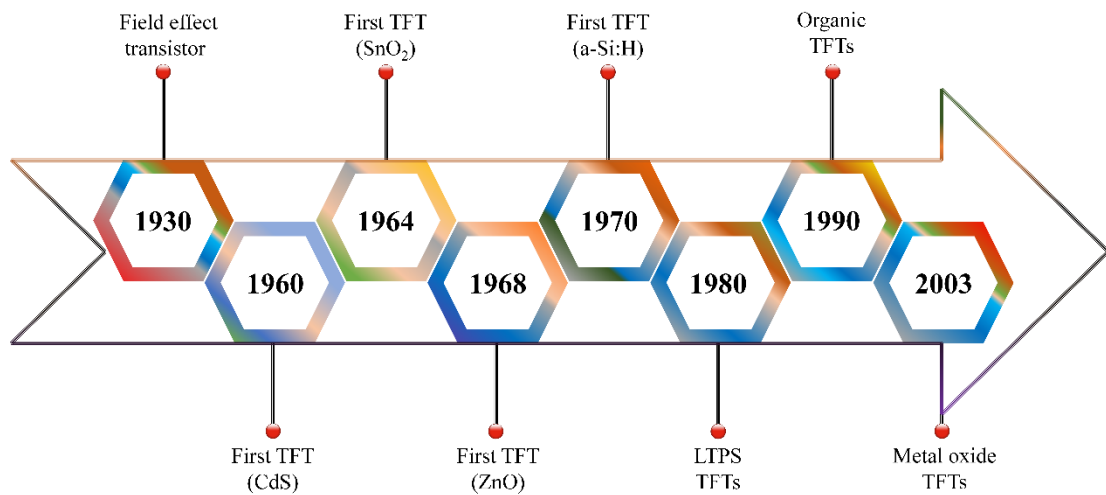
Fig. 2.1 Milestones of TFTs (LTPS: low-temperature polycrystalline silicon).

The performance of metal oxide based TFTs is much higher than a:Si-H and organic molecule-based semiconductors (Martins et al. 2009; Fortunato et al. 2012). Also, the amorphous metal oxide semiconductors are viable and low-cost alternatives to the TFTs, where high transparency and the significant electronic properties are desired.

2.3 Architecture and characteristics of TFTs

As per the definition, the TFTs are the three terminal devices, in which the semiconductor as an active layer is sandwiched between the dielectric material and the transversal gate electrode (simply termed as 'gate'). The fundamental principle in the mode of operation of the TFT is dependent on the modulation of flow of the current through the semiconductor, which is achieved through injection of charges at or near to semiconductor-dielectric interface and the phenomenon is called 'field-effect' (Tickle

and Approach 1969). Further, it is essential to know the terminologies being used worldwide: (a) semiconductor layer – active layer/channel layer, (b) electrode – source and drain, gate, top contacts, bottom contacts (based on the architecture of the TFTs), (c) dielectric – passive layer. Based on the placing of semiconductor and the source-drain contacts the TFTs are classified into two different categories, namely staggered and the coplanar (Wallmark and Johnson 1966) with subclassification, called top-gate and bottom-gate depending on the position of the gate electrode, as shown in the fig. 2.2.
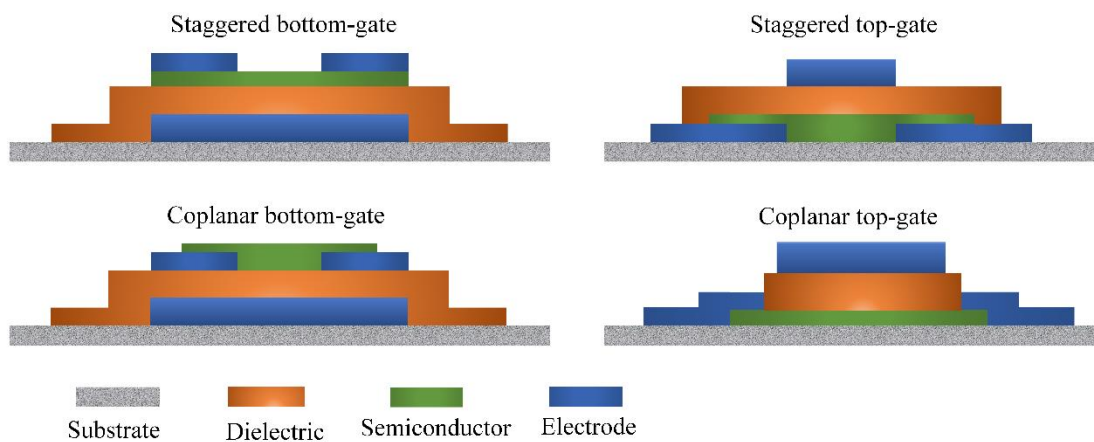
Fig. 2.2 Architectures of TFTs based on the positions of semiconductor and electrode.

The intention of having different architectures is to ease the processing of each layer of the TFTs. As an example, staggered bottom gate is employed in the case of a-Si:H TFTs because of photosensitive nature of a-Si:H and to avoid back-light in displays. Also, LTPS TFTs require coplanar top-gate architecture because the process of crystallization of LTPS may damage other components of TFTs (Fortunato et al. 2012)). Furthermore, in the case of bottom-gate configurations (staggered or coplanar), the semiconductor is exposed to the ambient atmosphere which leads to detrimental moisture contamination. Thus, to protect the top layer of the semiconductor, an additional insulating layer is commonly used, which disintegrates the surface of the semiconductor and the ambient atmosphere and imparts both chemical and mechanical protection to the semiconductor. Also, the top insulating layer helps the process of etching the electrode contacts without damaging the semiconductor surface (Kim et al. 2007).

In continuation, the supporting material holding all components of the TFTs is called the 'substrate'. It is a passive component of the TFT which does not undergo any structural, chemical and physical change during the processing of the components. Thus, for the polymeric substrates, the maximum temperature of film deposition should be lower than the glass transition temperature. Also, the substrate should not undergo mechanical deformation due to induced bending stresses during its service. Thus, there are challenges in the fabrication of flexible TFTs.

The TFTs are characterized in two distinct ways: (a) output characteristics: measures the current flow through the semiconductor, called output drain current (I_D) as the function of the voltage difference between the source and drain, called output voltage (V_D) at a fixed input called 'gate voltage' (V_G). (b) Transfer characteristics: transfers the output characteristics at a fixed V_D and plot of I_D vs. V_G gives an idea about the voltage at which transistor switches its state from 'OFF' to 'ON' or vice versa. The corresponding voltage at which the switching takes place is termed as on-voltage (V_{on}), and if V_{on} is calculated from a mathematical operation, as the intercept of the tangent of $(I_D)^{0.5}$ vs. V_G, then it is called threshold voltage (V_{th}). Nature of output and transfer characteristics along with the schematic of a TFT is presented in the fig. 2.3. Further, there are few derived static characteristics of the TFTs namely field effect mobility (μ), the on:off ratio (I_{on}:I_{off}) and subthreshold swing (S) which are explained as follows:

Field effect mobility (μ): It is an important parameter depicting the ease with which charge carriers flow in the semiconductor material (Fortunato et al. 2012). If it is calculated at the saturation region of the output characteristics, then it is termed as saturation mobility (μ_{sat}), which is significantly affected by several aspects such as structural defects, grain boundaries, impurities (Schroder 2006). In the case of TFTs, the flow of charge carriers is restricted to geometrically a narrow path resulting in additional scattering of charges thereby reducing the μ_{sat}. Such scattering mechanisms have resulted from the roughness (Schroder 2006) of the deposited semiconductor film and the quality of the dielectric-semiconductor interface. A widely accepted equation of μ_{sat} embodies different parameters, such as I_D, capacitance of the dielectric and the channel dimentions, is presented in equation 2.1

$$\mu_{sat} = \frac{\left(\frac{d\sqrt{I_D}}{dV_G}\right)^2}{1/2\, C_i \frac{W}{L}} \tag{2.1}$$

where C_i is the capacitance of the dielectric and W/L is the ratio of channel width to the channel length of the TFTs (fig. 2.3).
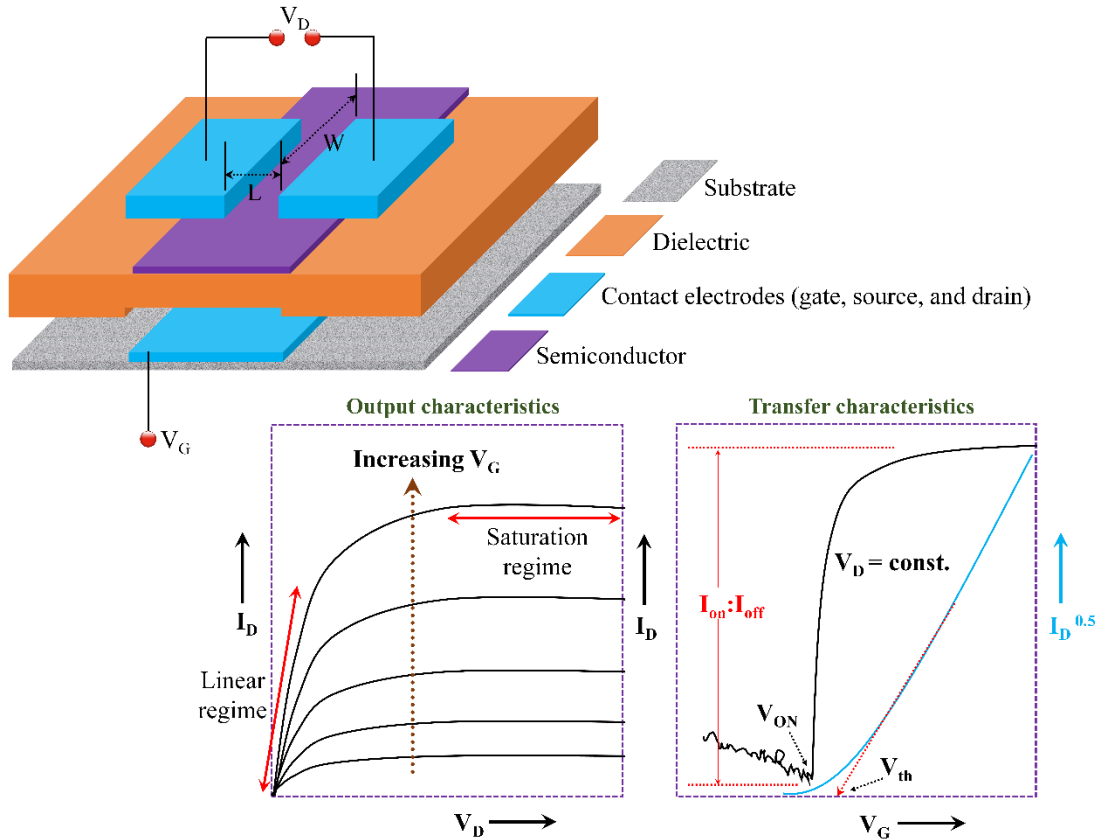
Fig. 2.3 The architecture of TFT with nature of output and transfer characteristics.

On:off ratio ($I_{on}:I_{off}$): The ratio of maximum achievable current (I_D) to the minimum current level. The minimum current can be attributed to the current flowing through the semiconductor, when it is in 'off' state can also be linked to the leakage current (I_G). This parameter conveys the switching ability of the TFTs. Higher the magnitude of $I_{on}:I_{off}$ larger will be the switching frequency of the TFT.

Subthreshold swing (S): The reciprocal of the maximum slope of transfer characteristic attributed to 'S' (equation 2.2). Smaller the magnitude of 'S', signifies the faster operation added with minimum power consumption. The ideal value of 'S' should be $<< 1$ typically 0.1-0.3 V dec^{-1} (Fortunato et al. 2012).

$$S = \left(\frac{d(logI_D)}{dV_G}\right)^{-1} \hspace{3cm} (2.2)$$

2.4 Flexible and transparent electronic devices

The widely accepted silicon technology fails to serve the purpose, where mechanical flexibility and optical transparency in the electronic devices is desired. To nullify the same, a-Si:H was proposed (Spear and Le Comber, (1975)) with a maximum field effect mobility of ~1 cm^{2}V^{-1}s^{-1}. Although it possesses a hundred times lower field-effect mobility than single crystal silicon, but suffices the requirement of displays. Another alternative along with a-Si:H is LTPS, which has greater advantages as far as the μ and I$_{on}$:I$_{off}$ are concerned (Lee and Joo 1996; Wager 2014). Since LTPS offers a μ as high as 100 cm^{2}V^{-1}s^{-1}(Wager 2014) and secures an opportunity of being an active material for TFTs. Owing to its high performance, LTPS is capable of replacing a-Si:H but fails to achieve low leakage currents. LTPS imposes additional process complexity compared to a-Si:H. LTPS demands significant modifications in the production line and the process flow, replacement of existing a-Si:H becomes demands economic influx. Thus, LTPS it is not widely accepted. In this regard, there is an urge for new materials and processes (Wager, (2014)).

There are two main categories of materials: organic and inorganic. After the discovery of conducting polymers, the organic materials became the front runner in the field of flexible electronics due to their low-temperature processability. The processing temperature goes well with flexible electronics due to its compatibility with thermal sensitive polymeric substrates (Lee et al. 2003; Choi et al. 2004). However, organic materials are facing a severe challenge in terms of their poor electronic properties and the environmental stability (Dimitrakopoulos Mascaro 2001). The maximum reported μ with organic semiconductor is not more than 10 cm^{2}V^{-1}s^{-1} (Shaw and Seidler 2001; Dimitrakopoulos and Malenfant 2002). Inorganic materials such as metal oxide, chalcogenides are other such options where retainment of electronic properties is much on the higher side compared to organic materials (Hosono 2006). In the queue of a large number of alternatives in both organic and inorganic materials, metal oxides have shown promising electronic properties added with an additional advantage of environmental stability. Both unary and doped metal oxides have been investigated in

the literature (Nomura et. al. 2004; Hosono 2006). The first candidate discovered is In_2O_3 as the semiconductor in metal oxide based TFTs (Nomura et al. 2004). However, In_2O_3 is relatively more conducting due to inherent anion point defects-vacancies. The formation of oxygen vacancies result in the generation of free charge carriers, due to which the off-currents of the TFTs shoots-up, thereby reducing the switching frequency ($I_{on}:I_{off}$). The generation of vacancies is due to the removal of oxygen from the crystal, the ease with which the oxygen leaves the crystal is mainly dependent on its binding energy with the cation (indium in the case of In_2O_3). Thus, it is essential to search for different cations which can replace indium. In other words, the urge for selection of particular substitutional dopant which has higher binding energy with oxygen. The choices proposed were zinc and gallium. Due to high binding energy of gallium and oxygen (Ga-O), the doped In_2O_3 based TFTs have shown improved $I_{on}:I_{off}$. This combination of cations emerged out as Indium-Gallium-Zinc-Oxide (IGZO). The first report on IGZO has shown μ_{sat} and $I_{on}:I_{off}$ ratios of the order 6-9 $cm^2V^{-1}s^{-1}$ and ~10^3 respectively (Nomura et al. 2004).

2.5 Amorphous metal oxide semiconductors

Interestingly, IGZO is a multi-component metal oxide with three cations indium, gallium, and zinc. The intention behind the selection of a ternary system is appreciable because, it essentially increases the configurational entropy of the system and enhances the crystallization temperature. The thin films of polycrystalline metal oxides result in the decreased μ due to scattering of the charge carriers. In addition, the crystallinity restricts the mechanical flexibility of the thin films. Thus, it is important to retain the amorphous nature of the film.

In the case of sp^3 hybridized covalent single crystal silicon, the transport of the charge carriers takes place through p-orbitals (fig. 2.4). Thus, any disturbance in the crystallinity of the silicon, results in the fluctuations of bond angles leading to the scattering of charge carriers and thereby reducing the μ, thus the maximum achieved μ in the case of a-Si:H was not more than 1 $cm^2V^{-1}s^{-1}$ (Hosono 2006). Further, for ionic solids, such as metal oxides with post-transition metal cations possess entirely different transport mechanism. The charge carriers prefer s-orbitals than p-orbitals due to the

broad spatial distribution of ns-orbitals. The isotropy of ns-spherical orbitals lead to the direct overlap with neighboring metal ns-orbitals and the intensity of overlap increases with wrenching of M-O-M bonds (fig. 2.4) (Hosono et al. 2008; Nomura et al. 2008). Thus, metal oxides can retain significant magnitude of μ in the amorphous state (Nomura et al. 2004; Hosono 2006). The concept was first demonstrated with amorphous IGZO (In:Ga:Zn = 1.1:1.1:0.9) on polyethylene terephthalate substrates at room temperature pulsed laser deposition technique (Nomura et al. 2004). Thus, amorphous metal oxide semiconductors have emerged as the potential alternatives to a-Si:H and LTPS in terms of processability and device performance. Table 2.1 shows the difference between a-Si:H, LTPS, and IGZO.
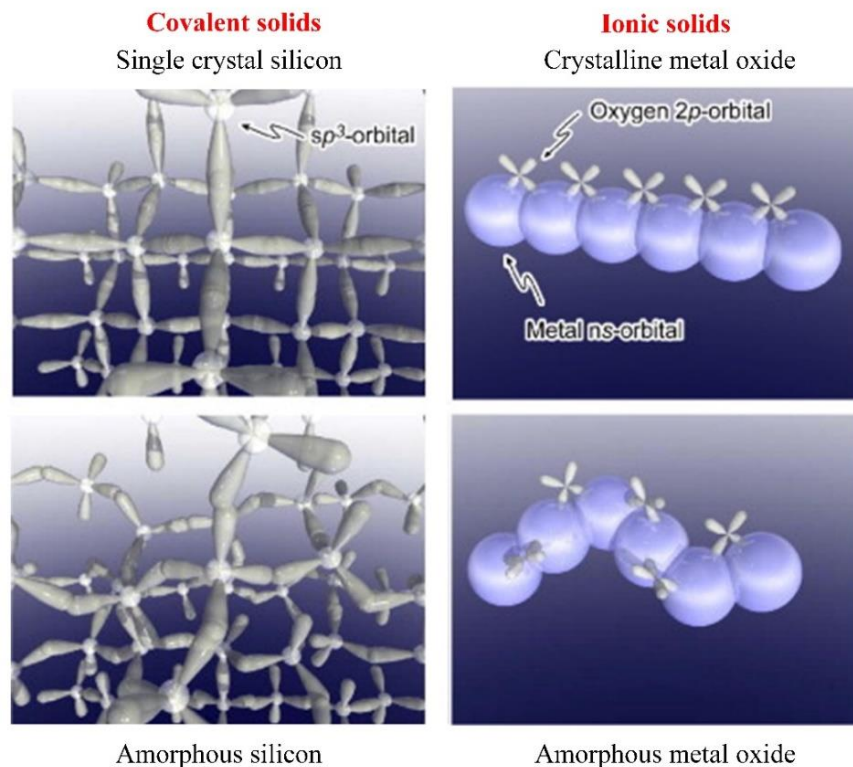
Fig. 2.4 Schematic showing orbitals, carrier transport pathways in crystalline and amorphous covalent-silicon and ionic-metal oxides (Nomura et al. 2008).

Owing to the high mobility of amorphous IGZO compared to a-Si:H, the size of TFTs can be reduced and high-resolution displays can be achieved (fig. 2.5). Soon after the discovery of easily processable IGZO, various electronic industries (SHARP, LG, TOSHIBA, DELL, NEC, APPLE, MEIZU, ZTE) initiated the manufacturing of

flat panel displays and many other electronic gadgets with IGZO based TFTs (Wager 2016). Further series of glass forming oxides having variable valent transition metal cations have been tested for their semiconducting action, and the field of research was named as "glassy semiconductors" (Austin and Mott 1969).

Table 2.1 Properties of a-Si:H, LTPS, and IGZO.

Property	a-Si:H	LTPS	IGZO
Microstructure	Amorphous	Polycrystalline	Amorphous
Mobility ($cm^2V^{-1}s^{-1}$)	~1	~100	~10-30
V_{th} stability	Poor	Good	Fair
Process complexity	Low	High	Low
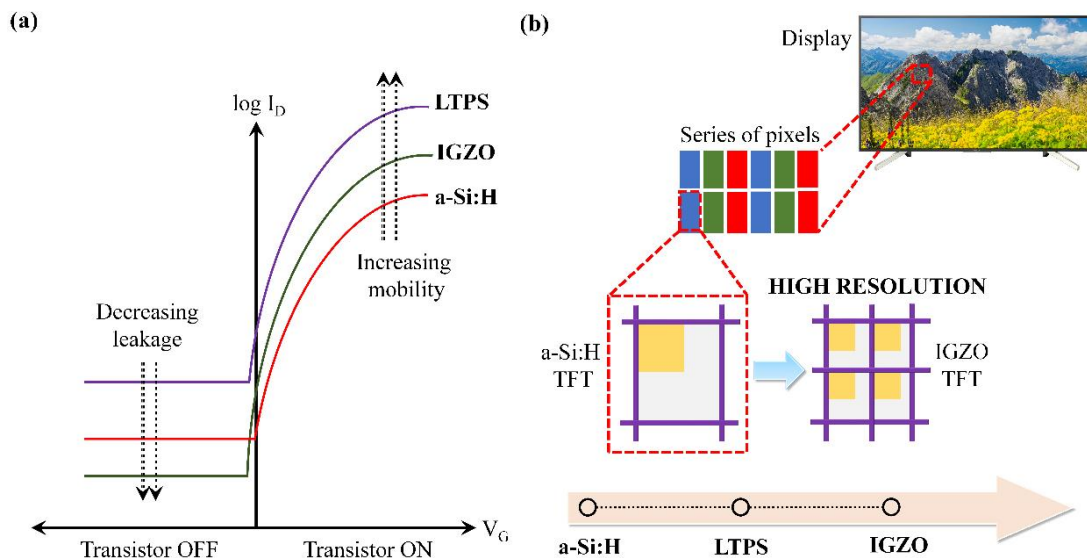
Fig. 2.5 Difference between a-Si:H, LTPS, and IGZO: (a) nature of transfer characteristics, (b) Schematic showing the reduction in pixel size.

During these years' concepts were taking shape but no application and proper material design were presented (Hosono 2006). The discovery of a-Si:H in 1975 made the researchers acquire a significant interest in the amorphous semiconductors (Spear and Le Comber 1975). The area "giant micro-electronics" was the outcome of the discovery of a-Si:H due to its capability to maintain reproducible and uniform characteristics

when deposited on the large substrates. The demand for transparent and flexible electronics started booming from the year 1994, after the failure of a-Si:H in few applications where optical transparency and mechanical flexibility were prime essentials with acceptable electronic properties (Ohta and Hosono 2004; Kamiya and Hosono 2005; Hosono et al. 2006).

Table 2.2 List of commercial products with IGZO TFTs (Wager 2016).

Product	Maker	Display
Phone		
Aquos Zeta SH-01	SHARP	5.5", 1080×1920, 415 ppi
M1 note	MEIZU	5.5", 1080×1920, 401 ppi
Readmi 2 prime	XIAOMI	4.7", 720×1280, 315 ppi
Laptop and desktop		
Radius 12	TOSHIBA	12.5", 3840×2160, 352 ppi
XPS 15	DELL	15.6", 3840×2160, 282 ppi
Skylake NS850	NEC	15.6", 3840×2160, 282 ppi

The proposed material design for the selection of multi-component post-transition metal cation-based amorphous oxides having an electronic configuration (n-1) d^{10} ns^0 turned out to be the breakthrough, which accomplishes almost all requirements such as large area deposition, optical transparency, and the mechanical flexibility. Large area deposition is due to the amorphous nature of the thin films of metal oxides, optical transparency is due to the wide band gap (3 to 4 eV), and mechanical flexibility is due to deposited thin films on flexible thermal sensitive substrates added with improved electronic properties compared to previously reported amorphous semiconductors. The band gap of the semiconductor plays a vital role in deciding its semiconducting nature which is affected by the nature of the bond and the bond angle. Also, the crystallinity is an active function of bond angle, and any fluctuation in the bond angles distorts the periodicity. Thus, there is a trade-off between the type of bond and the band gap of the amorphous semiconductor. In this trade-off, the amorphous ionic metal oxides gained an opportunity due to wide bandgap added with the sizeable spatial distribution of s-

orbitals, which completely nullifies the effect of distorted bond angles and do not impose any hindrance to the movement of charge carriers. The trade-off between the band gap and the type of bond is presented for various amorphous semiconductors in the fig. 2.6.
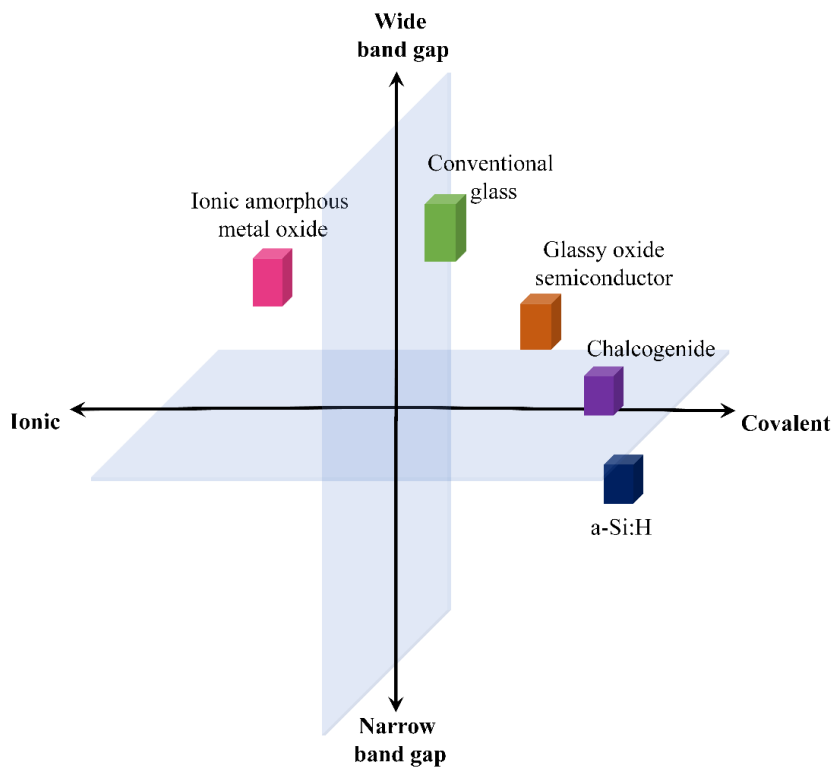
Fig. 2.6 Amorphous semiconductors with different bond types and the band gaps.

Further, the selection of post-transition metal cations having an electronic configuration (n-1) d^{10} ns^0 is mandatory because the value of principal quantum number (n) dictates the spatial distribution of s-orbitals and which in turn guides the transport efficacy of the charge carriers. This leads the selection of In_2O_3, ZnO, and gallium oxide (Ga_2O_3) systems with proper stoichiometry.

In addition to the above mentioned, other metal oxides such as SnO_2 can also play a similar role. The conduction band minimum in these metal oxides is mainly composed of a considerable number of vacant s-orbitals of metal cations with small valance band minimum of oxygen 2p-orbitals, which results in the extensive overlapping of vacant s-orbitals of cations along with the minimum contribution of 2p orbitals of anion (Hosono et al. 1996b; Hosono 2006). This phenomenon is perceived

in three widely accepted metal oxide systems. Namely, In_2O_3, ZnO, and SnO_2 and these are categorized as 'transparent conducting oxides', abbrevated as TCOs. Discussion of which is presented in the next section. Series of metal oxides obeying above mentioned electronic configuration were reported and proved the hypothesis of spatial overlapping of s-orbitals, which helps in building large percolation paths with distorted bond angles. $AgSbO_3$ (Yasukawa et al. 1995), $CdO-PbO_2$ (Hosono et al. 1996a), IGZO (Orita et al. 2001) are few such examples (Hosono 2006).

The concept of amorphous metal oxide semiconductors has been tested first ever with IGZO. Due to toxic cadmium and costly silver, the candidates containing these elements such as $CdO-PbO_2$ and $AgSbO_3$ were not selected for the hypothesis. The maximum field effect mobilities in case of IGZO were obtained for high indium compositions. It is due to perfectly obeying of the electronic configuration of In^{3+}, (n-1) d^{10} ns^0 with $n \geq 5$. Another critical aspect of an amorphous metal oxide semiconductor is to control the carrier concentration. The free charge carriers especially electrons make the semiconductor to increase its inherent conductivity, which contributes in the enhancing off-currents. Initial understanding on the same came into the picture during the deposition of IGZO semiconductor at room temperature. The well-known TCO, indium zinc oxide with a high concentration of indium needed to be suppressed; with same deposition conditions, the carrier concentration of sputter deposited films of amorphous-$InGaZnO_4$, and amorphous-$In_2Zn_3O_6$ found out to be $<$ 10^{13} cm^{-3} and 10^{18} cm^{-3} respectively (Nomura et al. 2004; Hosono 2006). The TFTs fabricated with amorphous-$InGaZnO_4$ and yttrium oxide as the dielectric has yielded μ_{sat} of 12 $cm^2V^{-1}s^{-1}$ with $I_{on}:I_{off} > 10^6$ (Nomura et al. 2004). These results have revealed that the Ga^{3+} is an efficient carrier (electrons) suppressor, due to its strong binding with oxygen. Amorphous metal oxides with heavy transition metal cation without a carrier suppressor can be a good candidate as TCOs. In other words, the demarcation of carrier concentration classifies metal oxides as semiconductors and conductors. This leads to the realization of transparent TFTs. The high-performance IGZO has grabbed considerable scientific attention and results of which can be seen in the near exponential increase of Scopus indexed scientific articles between 2006 and 2018 (fig. 2.7).
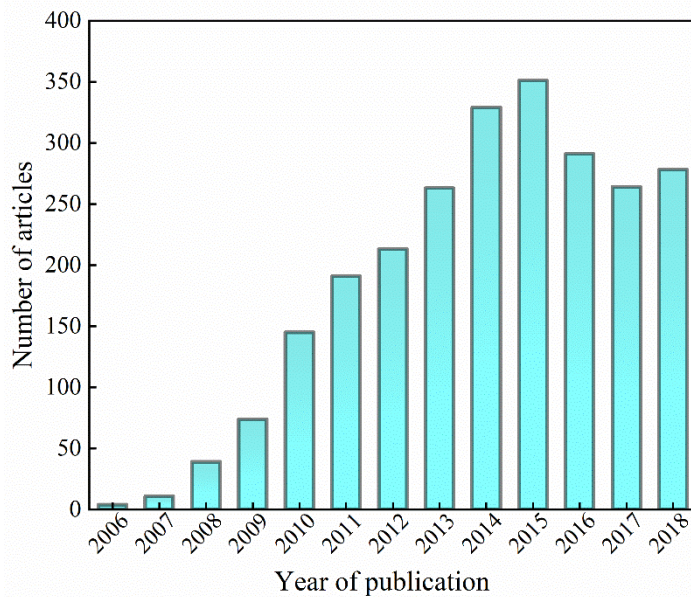
Fig. 2.7 The number of Scopus indexed articles published on IGZO based TFTs.

Apart from well-known IGZO, there are several n-type amorphous metal oxides have been investigated over the years namely ZnO (Li et al. 2007; Meyers et al. 2008), SnO_2 (Lee et al. 2007), zinc tin oxide (Chang et al. 2007; Park et al. 2009), indium zinc oxide (Park et al. 2010), indium zinc tin oxide (Kim et al. 2010; Bukke et al. 2018). Similarly, several p-type metal oxides have also been investigated; mention a few, copper oxide (Kim et al. 2013b), nickel oxide (Wang et al. 2016c), tin mono-oxide (Fortunato et al. 2012). The fundamental hypothesis all mentioned metal oxides remain unaltered, which is maintaining low carrier concentration $< 10^{13}$ cm^{-3}. Among all reported n-type amorphous materials, Indium-Zin-Tin-Oxide (IZTO) has shown remarkable performance in terms of μ_{sat} having a maximum value of 100 $cm^2V^{-1}s^{-1}$ (Kim et al. 2010). The IZTO has the luxury of tunable property between its semiconductivity and electrical conductivity. Thus, it is considered to be a potential candidate of TCO having comparatively minimum indium compared to conventional ITO.

2.6 Transparent conducting oxides

Optical transparency and metallic conductivity are two distinct characteristics, an amalgamation of these diverse properties in a single material is contradictory (Chopra et al. 1983; Hartnagel et al. 1995; Fortunato et al. 2007). Optically transparent

materials are insulators and possess high band gap, but metallically conductive materials own the Fermi level within the band giving rise to large density of states resulting in high carrier concentration. A TCO can be regarded efficient, if an optimum combination of these properties is achieved. In handful of metal oxides (ZnO, In_2O_3, CdO and SnO_2) the electrical conductivity can be imparted by degenerate doping, which displaces the Fermi level into the conduction band (Burstein 1954; Moss 1954) (fig. 2.8).
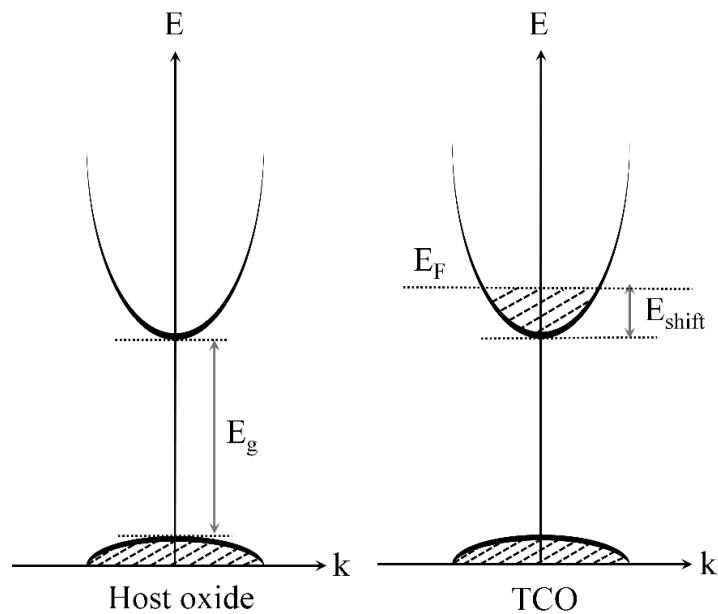
Fig. 2.8 Electronic band structures of host oxide and the TCO. Where, E_g = band gap and E_F = Fermi level.

The displacement of the Fermi level (E_F in fig. 2.8) can result in: (a) enhancement of the mobility of the additional charge carriers-electrons due to small effective mass and (b) alteration in the absorption (or the retainment of transparency) of the host metal oxide, due to low density of states (Fan and Goodenough 1977; Mryasov and Freeman 2001). The optimization of TCOs for their acceptable electrical conductivity and the optical transparency is challenging because of the absorption of the incident light by charge carriers (Frank and Köstlin 1982). The absorption of short wavelengths results in the inter-band transition and the absorption of long wavelengths results in the intra-band transitions thereby reducing the optical transparency. Further, the plasma oscillations result in the reflectivity and presence of substitutional ionic dopant

impurities results in the scattering (Facchetti and Marks 2010). From above mentioned adverse and detrimental effects, the achievement of a proper combination of optical transparency and the electrical conductivity becomes challenging and competitive.

The underlying mechanism of transport of charges is not straight forward in TCOs, the host metal oxides with electronic configuration (n-1) d^{10} ns^0 have four or six coordination numbers (Facchetti and Marks 2010). As mentioned above, the general host reported in the literature are ZnO, In_2O_3, CdO and SnO_2 have close-packed structures due to which they ensure a strong overlap of metal-ns and oxygen-2p orbitals. The oxygen-2p orbitals form the valance band and strong interaction between metal-ns and oxygen-2p results in the conduction band. Thus, the new carriers due to impurity doping results in a large number of available metal-ns and oxygen-2p interactions in the 3D space, enhances the electrical conductivity (Hamberg et al. 1984; Facchetti and Marks 2010).

2.6.1 Generation of charge carriers in TCOs

Altering the band structure by injecting the carriers will impart electrical conductivity into the host metal oxide. There are few crucial aspects which a TCO must qualify to achieve a suitable combination of electrical conductivity and optical transparency. They are: (a) the dopant must have complete solubility and should not promote the formation of non-conducting secondary phases (b) there should not be clustering of the defects, which arrest the charge carriers leading to the formation of defect pairs with neutral charge.

2.6.2 Doping into host metal oxide

Substitutional doping helps in the enhancement of the electrical conductivity of the host metal oxide (Minami 2000). The size of the dopant affects the lattice parameter. The shrinkage in the lattice parameter is significant, if the dopant ion is smaller than that of the host metal cation (Vegard 1921). The shrinkage in the lattice parameter can be theoretically predicted from the weighted average concept or the Vegard's rule (Vegard 1921). But, it may so happen in few cases that the anti-bonding nature of conduction band formed by the ns-orbital of the metal cation and the oxygen-2p results

in the expansion of the lattice rather than the contraction; as an example: yttrium doped CdO (Dou et al. 1998) and indium doped CdO (Morozova and Komarov 1995). Whereas, the gallium doped CdO show shrinkage due to smaller ionic radii of gallium (0.76 Å) compared to cadmium (1.09 Å). The effect of shrinkage also affects the optical properties (Jin et al. 2004; Yang et al. 2005; Jin et al. 2007). Aliovalent dopants in place of host cations, result in the generation of charge carriers. As an example, doping of Al^{3+} in the place of Zn^{2+} in ZnO crystal results in the generation of two electrons (equation 2.3).

$$Al_2O_3 \longrightarrow 2Al_{Zn}^{\cdot} + 2O_O^x + \frac{1}{2}O_2(g) + 2e^- \qquad (2.3)$$
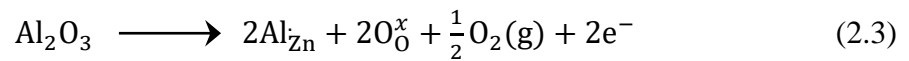
where 'x' represents the zero charge '$\cdot$' represents the positive charge.

2.6.3 Removal of oxygen from the crystal

In addition to the doping, generation of oxygen vacancies during thermal annealing can alter the defect chemistry. The removal of oxygen from the metal oxide is possible through: (a) thermal annealing and (b) annealing in oxygen deficient atmosphere. The elimination of oxygen from the metal oxide crystal leaves behind two free electrons. The left-out electrons stay in the crystal and they are bound to the vacant site of the oxygen (Facchetti and Marks 2010). These electrons can localize or free to move in the crystal. The formation of oxygen vacant site with two electrons bound to it can be represented by Kröger–Vink notation (equation 2.4).

$$(null) \; O_O^x \longrightarrow V_{\ddot{O}} + \frac{1}{2}O_2(g) + 2e^- \qquad (2.4)$$
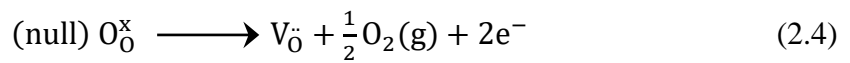
Metal oxides having high formation energy such as Al_2O_3 (-1582.3 KJ·mol^{-1}) makes electrons to get localized around the vacant site otherwise the electrons are free to move in the crystal (Reed 1971). The TCOs such as ZnO having low formation energy (-320.5 KJ·mol^{-1}) promotes substantial deficiencies of oxygen leading to the generation of carriers of the order $\sim 10^{19}$ cm^{-3} of the crystal (Schmalzried 1964; De Wit et al. 1977). Presence of oxygen deficient regions renders the significant change in the electronic band structure (Lany and Zunger 2007; Medvedeva and Hettiarachchi 2010). To

illustrate the same, the electronic band structures of host-In_2O_3, In_2O_3 with oxygen deficiency is presented in fig. 2.9.
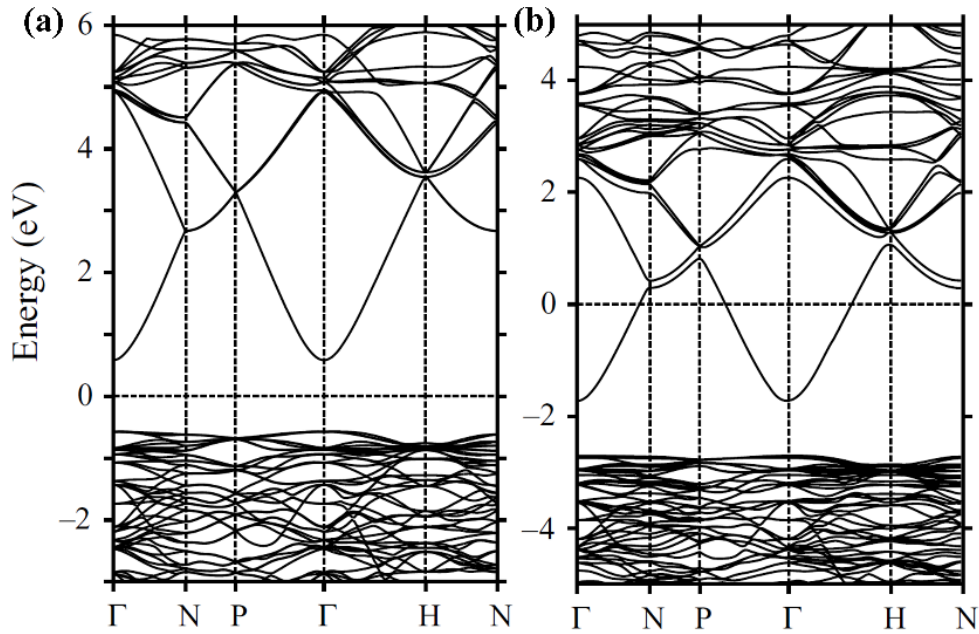
Fig. 2.9 Electronic band structures of (a) host-In_2O_3 (Medvedeva 2007) and (b) host In_2O_3 with oxygen deficiency (Medvedeva 2006).

2.6.4 Concept and characteristics of TCOs

The widely accepted commercial grade TCOs is ITO. The thin films of ITO have a wide range of applications in displays, light emitting diodes (LEDs), solar cells, automobiles, energy efficient windows etc. The maximum achieved transparency around 90 % in the visible region and conductivity of the order 10^3 S/cm (Gordon 2000) with 10 wt.% doping of tin in In_2O_3. The highest electrical conductivity with acceptable transparency possessed by ITO is mainly due to carrier concentration ($\sim 10^{21}$ cm^{-3}).

2.6.4.1 The electrical conductivity of TCOs

The electrical conductivity (σ) is a direct function of carrier concentration (N) and mobility of the charge carriers (μ_c) (equation 2.5)

$$\sigma = N\, e\, \mu_c \qquad (2.5)$$

where e is a charge of the electron (= 1.602×10^{-19} C). Increase in the value of N and μ_c increases the σ. The value of N can be increased by impurity doping and by generating native point defects such as vacancies. Anion vacancies give rise to electrons, and the cation vacancies give rise to holes. The classification of n- and p-type TCOs depends on the type of charge carriers. The mobility of the charge carriers does depend on a series of factors such as the effective mass of charge carrier (m*), relaxation time (τ), size and type of impurity-dopant, and grain boundaries. An equation which takes care of these entities is presented in equation 2.6

$$\mu = \frac{e\,\tau}{m^*} \qquad\qquad (2.6).$$

To increase the mobility, the scattering time must be increased and the effective mass must be decreased. The effective mass is material specific and the scattering time is depending on the quality of the thin film of TCO deposited (Pasquarelli et al. 2011). The latter can be depicted based on the type of scattering phenomena. In other words, anything in the path of charge carries inhibiting the movement, decreases the magnitude of τ. According to Matthiessen's rule (Pasquarelli et al. 2011), the obstacles in the movement of charge carriers independently affect the electrical resistivity. The summing up of different scattering sites such as grain boundaries, impurities, and the defects can be represented in equation 2.7.

$$\frac{1}{\mu_{total}} = \frac{1}{\mu_{grain\ boundaries}} + \frac{1}{\mu_{impurity}} + \frac{1}{\mu_{defects}} + \cdots \qquad (2.7)$$

The effect of individual scattering sites depends on both types of material and type of processing. For example, ionized impurity scattering is prominent in case of semiconducting oxides; grain boundary scattering becomes dominant for nano-granular structure or if the size of the grain is smaller than the mean free path of the charge carriers. If the thin film of the TCOs is prepared by solution processing, then the porous structure of the film can result in the scattering. The above-mentioned concepts of TCOs and conductivity mechanisms well account for crystalline TCOs, but due to non-periodicity of amorphous TCOs the precise mechanism of conduction through impurity doping or native point defects is unclear (Mason et al. 2002; Fergus 2003).

2.6.4.2 Optical transparency of TCOs

According to the Drude free electron model, the electric field component of the light interacts with the electrons present in the material, resultant of which the light can get either absorbed, transmitted or reflected. The typical nature of the curves of transmission, reflection, and the absorbance is presented in fig. 2.10.
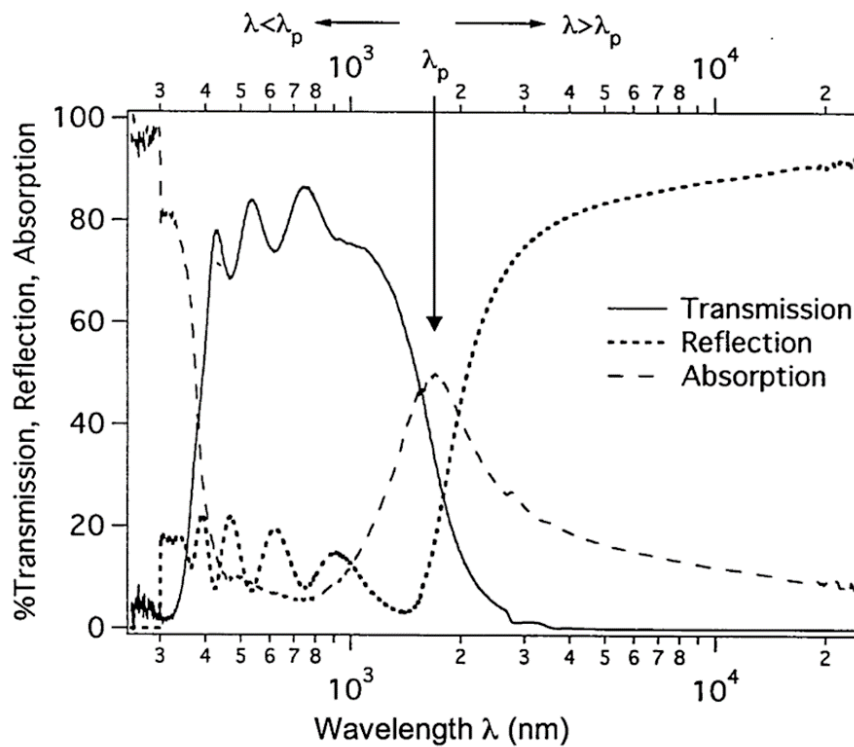
Fig. 2.10 UV-visible-near IR spectra of an ideal TCOs (Pasquarelli et al. 2011).

The analogies derived from spectra are (a) the thin film of TCO is transparent in the visible region of the spectrum i.e., 400 nm to 750 nm (hυ = 3.1 to 1.7 eV), (b) Incident light with the wavelength < 350 nm or 3.5 eV gets absorbed and results in the band transitions reduce the transparency drastically, (c) The increase in the reflection and reduction in the transmission at higher wavelengths (> 1500 nm). Thus, a typical TCO possesses a bandgap of more than 3 eV. If the oscillation of electrons, which are in phase with the electric field component of the incident light, results in the maximum absorption; the corresponding wavelength of maximum absorption is called plasma wavelength (λ_p). Any wavelength smaller than the plasma wavelength ($\lambda < \lambda_p$) gets transmitted and wavelength larger than the plasma wavelength ($\lambda > \lambda_p$) gets reflected.

There is an interdependency between the optical and electrical properties of TCOs through λ_p (Calnan and Tiwari 2010). The λ_p shares an inverse relation with the carrier concentration, thus any attempt to increase the carrier concentration lead to the decrement in the optical transparency. In other words, an increase in electrical conductivity demands reduction in optical transparency in the visible range. Thus, there exists a trade-off between these properties. The remedy of which can be derived from equation 2.5 of electrical conductivity, which states that the dependency of electrical conductivity is also pronounced with an increase in mobility. The search of dopants should be made in the way that these dopants should not contribute to the conductivity but the mobility. Example of such dopants is molybdenum and titanium. Owning to their high binding energies with oxygen results in the minimum generation of carriers results in the faster movement of carriers, which gives rise to high mobility (Van Hest et al. 2005; Van Hest et al. 2006; Pasquarelli et al. 2011). Table 2.3 lists the various TCOs and their electrical and optical properties.

Table 2.3 List of different TCOs and their properties

TCO	σ (S/cm)	t (nm)	Transparency (%)	Reference
F:ZnO	1531.4	1306	90	Hu and Gordon 1991
Al:ZnO	300	750	85	Hu and Gordon 1992
Cd:SnO$_2$	4900	200	90	Mamazza et al. 2005
Mo:In$_2$O$_3$	1369	--	90	Seo and Park 2005
Sn:In$_2$O$_3$	5000	170	92	Kim et al. 1999
Nb:TiO$_2$	1136	40	97	Furubayashi et al. 2005
Ga:ZnO	1000	300	85	Choi et al. 1990
F:SnO$_2$	4546.8	1100	85	Rakhshani et al. 1998
Ti:In$_2$O$_3$	800	200	90	Heo et al. 2009

t = thickness of the film

2.6.5 TCO hosts and dopants

Series of hosts and dopants available which can give a significant combination of electrical conductivity and optical transparency. The well-established hosts are In_2O_3, SnO_2, ZnO, CdO and Ga_2O_3. The material design concept for both conducting and semiconducting metal oxides is the same. But, the additional requirement of the TCOs is that the host metal oxide should promote the generation of charge carriers naturally. The charge carrier generation could be by impurity doping or by thermal assisted native point defects. If the TCO hosts reside at the corners of a hexahedron, then the edges of hexahedron show the binary systems and the faces depict the ternary systems s shown in fig. 2.11.
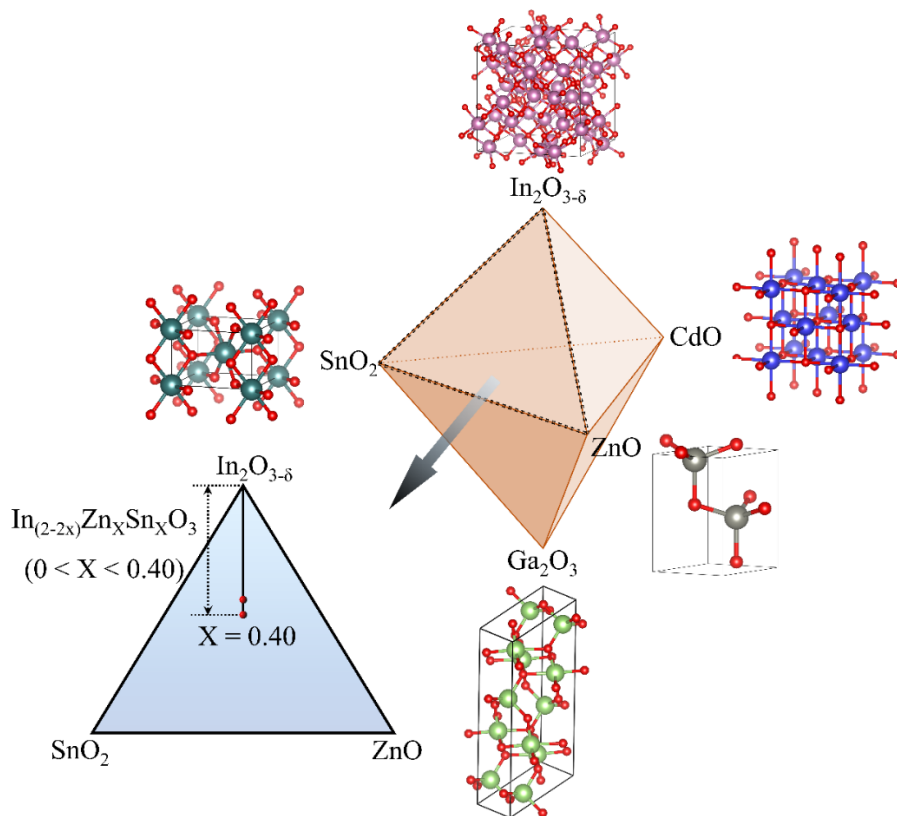
Fig. 2.11 Hexahedron is representing TCO hosts at its corners along with their unit cells (color codes: red-oxygen, magenta- indium, blue-cadmium, green-gallium, and cyan-tin) and Gibb's triangle of In_2O_3-SnO_2-ZnO ternary system at 1275 °C (Harvey et al. 2008b).

Due to strong Ga-O bonding and high Gibb's formation energy, the creation of point defects in Ga_2O_3 system is inferior. CdO exhibit highest electrical conductivity due to strong hybridization Cd-s and O-2p orbitals, but it is less popular due to its toxic nature. The remaining options are ZnO, In_2O_3 and SnO_2, in which tin doped In_2O_3 accepted commercially. Due to multivalences of tin (4+ and 2+), the standalone tin oxide without doping can generate electrons. Above mentioned TCOs are n-type in nature due to their ease of formation of electrons over holes.

Further, the type of dopants plays a crucial role and are the ultimate decision makers in generating charge carriers. Both cation and anion can be replaced or substituted by foreign impurity ions. There are complex selection rules for the dopants based on their size, valency and solid solubility. Higher is the solid solubility larger will be the degeneracy in doping. Since in conventional electronics such as silicon, the term 'doping' refers to the small fraction of impurities, but in case of metal oxide based electroceramics, the term 'doping' has a broad meaning, where the concentration of dopants is high enough to generate charge carriers, when the requirement is to achieve high electrical conductivity. Thus, the literal meaning of 'impurity substitution' in metal oxides resembles the 'degenerate doping' in conventional silicon technology.

The TCOs are largely n-type in nature. The rare TCOs does show p-type behavior, but the maximum reported electrical conductivity of p-type TCOs or holes as prime and majority charge carriers is not more than ~1 Scm^{-1} with the mobility of ~1 $cm^2V^{-1}s^{-1}$ with carrier concentration of less than 10^{18} cm^{-3} (Pasquarelli et al. 2011). The conduction of holes is difficult because of oxygen-2p orbitals, which form the deeper levels below the valance band (Kawazoe et al. 2000). It is not surprising that the p-type TCOs are rare but introduced first in 1997, which was a spinel type TCO called copper aluminate ($CuAlO_2$) (Kawazoe et al. 1997). The spinel stoichiometry AB_2O_4 having A = Ni and Zn, B = Ir, Co have shown p-type conduction, but suffer poor electrical functionalities (Owings et al. 2005; Banerjee and Chattopadhyay 2005; Dekkers et al. 2007; Exarhos and Zhou 2007).

2.6.6 Alternate to ITO

In this section, the range of different TCOs is reported other than conventional ITO. The elegance of ITO is its combination of 'electrical conductivity and optical transparency'. Due to rare earth indium acting as the host of ITO shoots up its cost. Over the years many research groups are keenly concentrated on the replacement of ITO, either partially or fully. The complete replacement of ITO can also be attributed as an indium-free system. For example, aluminum doped zinc oxide (Al:ZnO), fluorine-doped tin oxide (F:SnO$_2$), molybdenum doped tin oxide (Mo:SnO$_2$), niobium doped titanium oxide (Nb:TiO$_2$) etc. Also, the partial replacement in the sense of a reduction in the indium percentage in ITO, which can be fulfilled either by increasing the doping percentage of tin in In$_2$O$_3$ or by co-doping of more than one dopant. From the hexahedron presented in fig. 2.11, the likely choices for the multiple dopants are gallium and zinc in ITO. Since gallium is a carrier suppressor thus the best choice for co-doping is zinc along with tin in In$_2$O$_3$.

The tunable composition of co-doping results in the wide range of composition, also the solid solubility due to co-doping increases compared to their individual solubilities in the same host. As an example, only 2 at. % of tin can replace indium in In$_2$O$_3$ (Gonzalez Aviles 2003) and solid solubility of indium in SnO$_2$ is negligible (Heward and Swenson 2007). However, the co-doping of zinc and tin is possible up to a maximum of 40 at. % in case of zinc and tin together replacing indium in In$_2$O$_3$ (In$_{(2-2x)}$Zn$_x$Sn$_x$O$_{3-\delta}$, $x_{max} = 0.4$) (Palmer et al. 1997a). Thus, co-doping promotes the reduction in indium percentage by 60 % compared to ITO (Hoel et al. 2010). Co-doping has a great potential in developing next-generation indium-based TCOs reduced the percentage of indium. Irrespective of the type of TCO, following are the few selection criteria that the TCO system must obey:

$\Rightarrow$ A minimal or no usage of indium.

$\Rightarrow$ A bandgap more than 3.1 eV, to transmit at least 85 % of visible light.

$\Rightarrow$ An electronic configuration: (n-1) d^{10} ns^0 (n = 4, 5), example: Zn^{2+}, Cd^{2+}, Sn^{4+}.

Among above mentioned three crucial aspects of TCOs, the concept of indium-free TCOs gained an important role; table 2.4 shows a list of indium-free TCOs (Gordon 2000).

Table 2.4 List of TCOs with no or minimum indium and their properties

Properties	TCO
Highest transparency	Cd_2SnO_4, Zn_2SnO_4, F: ZnO
Low plasma frequency	F: SnO_2, F: ZnO
Highest mobility	CdO, Ti: In_2O_3, Mo: In_2O_3
Lowest cost	F: SnO_2

2.6.6.1 Indium Zin Tin Oxide

A complex ternary oxide, composed of indium, zinc and tin cations in 3+, 2+ and 4+ states respectively with host-indium oxide shows an opportunity of being a TCO with a reduced percentage of indium due to extra substitutional impurity zinc (Harvey et al. 2008b). There are two reported compositions of TCOs and a homologous series namely, $In_{(2-2x)}Zn_xSn_xO_{3-\delta}$ where $0 \leq x \leq 0.4$, $Zn_{2-x}Sn_{1-x}In_{2x}O_4$ where $0 \leq x \leq 0.45$, $(ZnO)_k$ In_2O_3 where k = 3, 4, 5, 6, 7, 9, 11 respectively (Harvey et al. 2008b). Fig. 2.12 shows the subsolidus phase diagram first reported in the year 2008. The Gibb's triangle drawn at 1275 °C having end components as In_2O_3, ZnO and SnO_2 shows single, two also three phase regions. Two red lines presented with respective compositions are of single phase, the compositions lying within the compatibility triangles are of three phases. A small deviation from the single-phase renders the composition of interest to fall in the two-phase region. Following are the few salient features of the phase diagram:

$\Rightarrow$ The end-members of Gibb's triangle are unary phases. Namely, In_2O_3 which crystallizes in a cubic bixbyite structure (Marezio 1966) which is a modified anti-fluorite structure falls in the space group *Ia3*. Similarly, ZnO and SnO_2

crystalize in wurtzite (space group: P6₃mc) and tetragonal (space group: P4₂/mnm) structures respectively (Wyckoff 1963; Gonzalez Aviles 2003).

⇒ The vertices of the triangle represent the binary systems. The line connecting In_2O_3 and SnO_2 gives rise to a binary well known TCO called ITO having a general composition $In_{(2-2x)}Sn_{2x}O_3$ depicting a solid solubility of tin in In_2O_3 not more than 2 at. % (Harvey et al. 2008b) but this value substantially increases to 8.6 at. % (Gonzalez Aviles 2003) in the case of thin films and nanopowders of ITO.
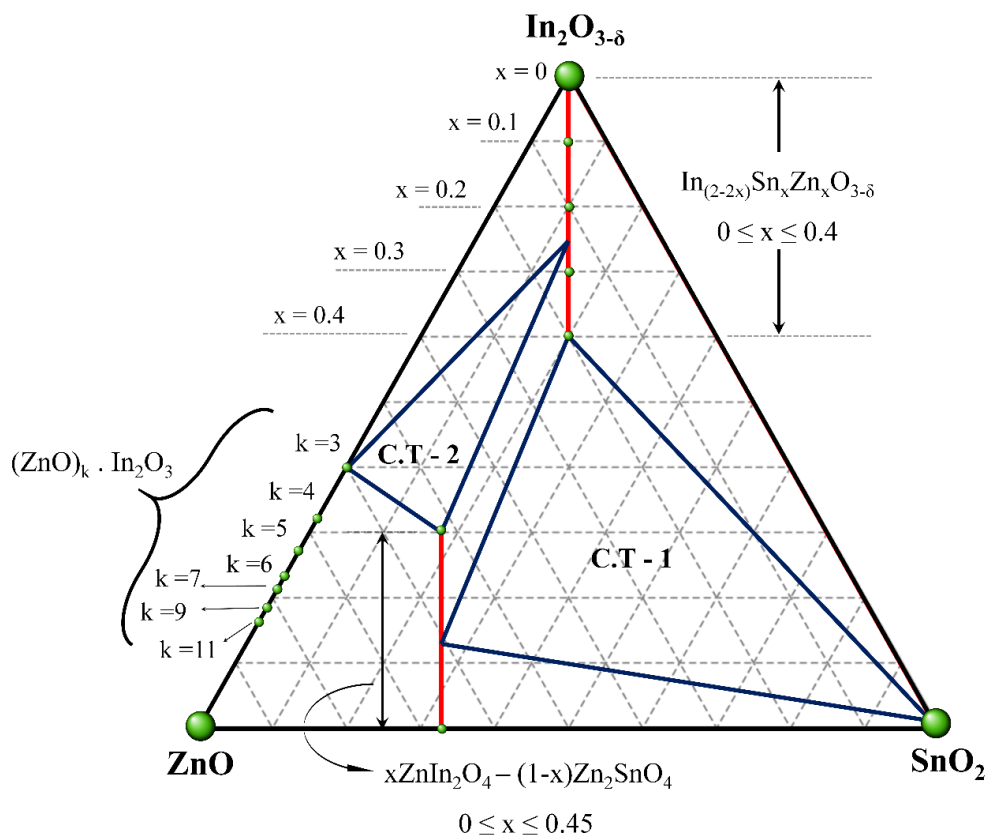
Fig. 2.12 Gibb's triangle (1275 °C) of In_2O_3-ZnO-SnO_2 ternary system (Harvey et al. 2008b) representing two compatibility triangles C.T-1 and C.T-2 and other TCO compositions (Harvey et al. 2008b).

⇒ Also, general secondary phases such as $In_4Sn_3O_{12}$ appears with an increase in the doping percentage of tin beyond its solid solubility. In the case of SnO_2-ZnO system, only one compound namely zinc stannate spinel is observed (Zn_2SnO_4). Further, the binary system consisting of end members In_2O_3-ZnO shows a range

of compounds called homologous series. The general formula for which is $(ZnO)_k.In_2O_3$ with k = 3, 4, 5, 6, 7, 9, 11. These range of compounds are characterized by short 'a-axis' and long 'c-axis' (Harvey et al. 2008b).

⇒ Commenting on the bixbyite ternary solid solution $In_{(2-2x)}Zn_xSn_xO_{3-\delta}$: due to the isovalent nature and similar sizes the maximum solubility of zinc and tin through co-doping increases up to 40 at. % (Harvey et al. 2008b). Although there is a substantial reduction in the indium percentage in the system due to extra zinc cation, the resulting system is an outstanding TCO. As an example, the maximum electrical conductivity of a pulsed laser deposited films of $In_{(2-2x)}Zn_xSn_xO_{3-\delta}$ with $x = 0.3$ was reported to be 4000 S/cm (Harvey et al. 2008a).

⇒ The bixbyite $In_{(2-2x)}Zn_xSn_xO_{3-\delta}$ ($x = 0$ to 0.4) does not work on the intuitive of increase in the conductivity with an increase in the doping concentration. The increment in the electrical conductivity with doping concentration is not significant because the underlying mechanism of 'off-stoichiometry' (Harvey et al. 2008b). There is a slight variation in the stoichiometry of the bixbyite $In_{(2-2x)}Zn_xSn_xO_{3-\delta}$ from its equilibrium concentration of dopants. The off-stoichiometry is towards tin donors than the zinc acceptors, and the difference in these varies as a function of co-doping. Fig. 2.13 shows the off-stoichiometric line in the phase diagram. The value of 'n' in the fig. 2.13 is the degree of off-stoichiometry, which is defined as the difference between the concentration of tin donors and the zinc acceptors and is a quantification of 'n' is difficult (Harvey et al. 2008a).

⇒ The lattice parameter of the system $In_{(2-2x)}Zn_xSn_xO_{3-\delta}$ with $x = 0.4$ is found to be 9.99 Å, which is smaller than the host In_2O_3 (10.12 Å) due to the smaller sizes of the dopants Zn^{2+} and Sn^{4+} compared to In^{3+} (Harvey et al. 2008b).

⇒ Another ternary solid solution is indium doped zinc stannate spinel having a stoichiometry of $Zn_{(2-x)}Sn_{(1-x)}In_{2x}O_4$ with $x = 0$ to 0.45. Before doping with indium, the zinc stannate spinel-host is non-conductive and attains moderate conductivity (~ 3 Scm^{-1}) (Palmer et al. 1997b) with an increase in the doping concentration.
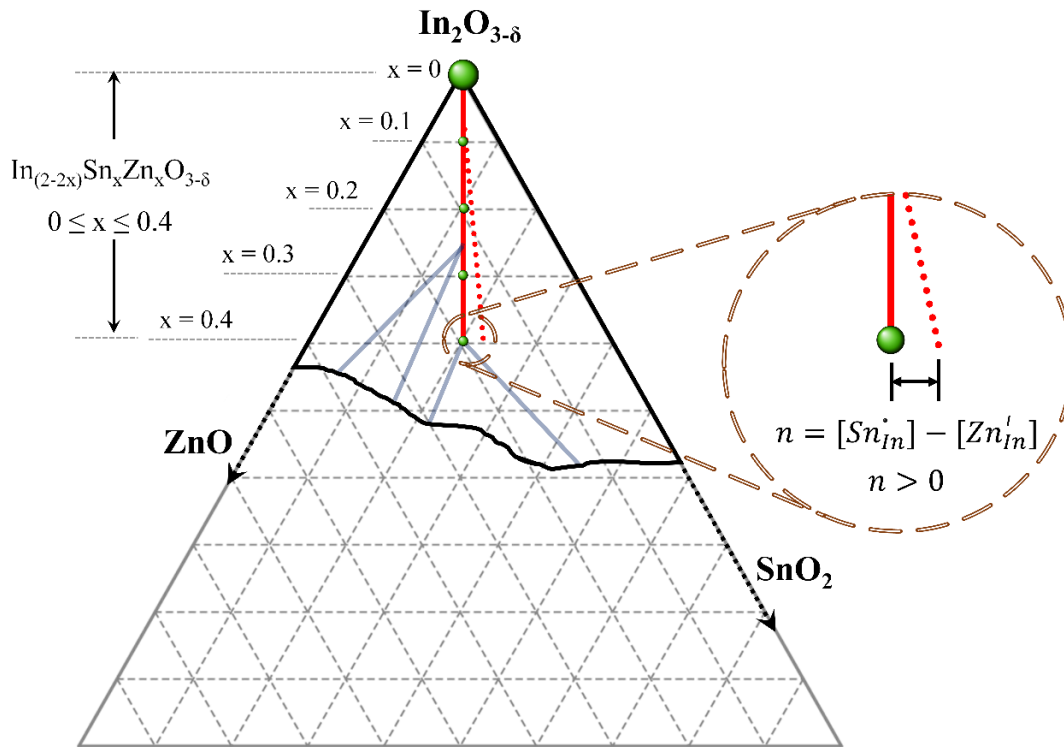
Fig. 2.13 The Gibb's triangle of In_2O_3-ZnO-SnO_2 showing off-stoichiometry in the $In_{(2-2x)}Zn_xSn_xO_{3-\delta}$ composition over the range of co-doping and the zoomed view depicting the degree of off-stoichiometry (n) (Harvey et al. 2008b).

2.7 Importance of dielectrics

In the above sections, the metal oxide semiconductors and the electrodes are elaborated. Another essential component of the TFTs is the dielectric. The conventional silicon dioxide (SiO_2) possess low permittivity and TFTs employing SiO_2 demands high input voltages. To achieve low voltage operation, there is an urgent requirement of dielectrics with high permittivity. Amorphous metal oxides are promising candidates with high permittivity (Liu et al. 2018). Amorphous metal oxides are promising candidates with high permittivity. Another critical parameter considered to be an essential ingredient for the betterment of electrical functionality is the leakage current. The order of leakage current need to be minimized for the successful capacitive action. The atomic scale SiO_2 shows leakage of more than 1 Acm^{-2} at 1 V of applied bias (Wong

2011; Liu et al., (2018). Thus, the dielectrics urge for larger thicknesses. But, in the era of miniaturization, there is a continuous demand or lowering the thickness and enhancing the capacitance to get low voltage operation. From the fundamental relation (equation 2.8), the capacitance inversely depends on the thickness of the dielectric

$$C = \frac{\varepsilon_o k A}{d} \tag{2.8}$$

where C, ε_o, k, A, d is capacitance, permittivity of free space (8.85418782×10^{-12} m^{-3} kg^{-1} s^4 A^2), dielectric constant (also termed as the permittivity of the dielectric material), area of overlap and thickness of the dielectric. In order to maintain the same capacitance with acceptable thickness, the dielectric material should possess high permittivity. Thus, achievement of the similar capacitance as that of thick dielectrics is possible in the case of thinner ones with large dielectric constants. Examples of which are hafnium oxide are considered to be the next best candidate after SiO_2. At this stage, it is worth mentioning about the series of high-k materials are categorized into (a) self-assembled molecular (SAM), (b) inorganic-organic hybrid materials, (c) electrolytes, (d) ferroelectric polymers, and (c) amorphous metal oxides.

SAMs have shown high areal capacitance and low leakage current of the order 10^{-8} Acm^{-2} the first report on SAM was reported using octadytrichlorosilane (Vuillaume et al. 1996). The advantage of SAM is the compatibility with different semiconductors such as organic and inorganic metal oxides (Ortiz et al. 2009). Due to the complex inert processing requirements, SAMs are yet to be commercialized. Further, the composite high-k dielectric having organic-inorganic mixtures are reported. The first report on TiO_2-polystyrene composite has shown promising results (Khastgir et al. 1988). Various groups have proposed different composites using nanoparticles of $BaTiO_3$, ZrO_2 and sodium β-alumina (Kagan et al. 1999; Zhou et al. 2012). Due to poor dispersibility of metal oxide nanoparticles in polymer matrix led undesired agglomeration resulting in severe performance setbacks and over the time the system is getting less visibility in the literature. Other sets of high-k dielectrics, like electrolytes possess exceptional areal capacitances (10 μFcm^{-2}) rendering ultralow operating voltages (Kim et al. 2013a). Due to mechanical instability and the poor adhesion, the electrolytes have not shown reproducible performance.

Another category of high-k dielectrics is the ferroelectric polymers. The fluorinated polymers such as such as poly (vinylidene fluoride co-trifluoroethylene) possess high-k (> 10) (Chen et al. 2017). However, it fails to deliver hysteresis-free performance due to their inherent ferroelectric properties. Thus, employed in memory devices rather than switching devices such as TFTs (Caironi and Noh 2015). It is essential to reduce the hysteresis with maintained high-k, to accomplish the same blending with polymethyl methacrylate was reported (Baeg et al. 2012). It is challenging to have high-k with low hysteresis, to address the same amorphous metal oxide dielectrics have been investigated over the years. Mention a few Al_2O_3, ZrO_2, HfO_2, Ta_2O_5 and so on. High-k, low leakage, and less hysteresis, substantial environmental stability, solution processability are the key advantages of amorphous metal oxide dielectrics (Liu et al. 2018). One such dielectric which is less investigated in the literature is sodium β-alumina. The high-temperature stable β-phase of sodium incorporated alumina has shown a dielectric constant of ~200 (Pal et al. 2009) with a negligible hysteresis. The sodium β-alumina is considered to be an anisotropic ceramic material due to its dual nature of solid electrolyte and the dielectric. The structure of the sodium β-alumina consists of alternate layers of spinel alumina blocks with sodium ions situated between the layers (fig. 2.14). The movement of the sodium ions is blocked by the presence of alumina blocks perpendicular to the plane in which sodium ions are situated. On the other hand, the sodium ions move with great ease in the parallel direction to the alumina spinels. Thus, there exist dual electronic functionality due to the movement of sodium ions (Lu et al. 2010). Though there is an enormous literature on the usage of sodium β-alumina in batteries, the reported literature on its dielectric nature in TFTs and other electronic devices is scares and requires more understanding and careful investigation with different semiconductors. Other than sodium, few investigations on other alkali dopants have been reported such as potassium and lithium (Zhang et al. 2011; Liu et al. 2013).

In the previous sections, complete description of the materials especially functional metal oxides as transparent semiconductors, transparent conductors and dielectrics are presented. Regardless of their electronic properties, the processing of metal oxides plays a crucial and decisive role. The complete fetching of their purpose

will only be fulfilled if they are processed economically with maximum yield. Almost all applications demand 'thin films' of metal oxides. The word 'thin film' is enclosed in quotations because of a film on the substrate regarded as thin, if its thickness is well below a critical value. Higher thickness will lead to the interpretation of 'coating' rather than 'thin films'. There are various methods to fabricate thin films of metal oxides. Forthcoming section is dedicated to the processing of thin films.
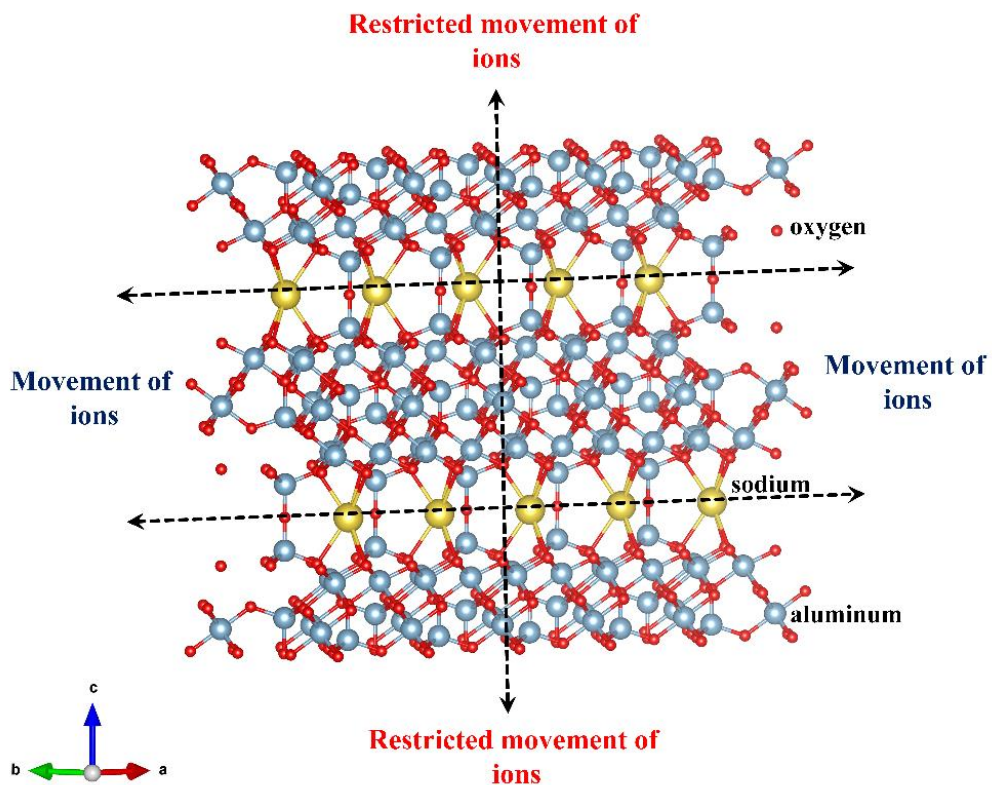
Fig. 2.14 Crystal structure of sodium β-alumina (blue-Al, yellow-Na, red-O).

2.8 Thin film processing

There are fundamentally two techniques of deposition of thin films onto a substrate, (a) evaporative- and (b) solution-based. The primary difference that led to this classification is the nature of the initial precursor. In the case of evaporative techniques, the primary form of the material to be deposited is in the solid state and liquid in the case of solution processing. There are several evaporative techniques, which have been employed by various research groups for the deposition of the thin films, such as thermal evaporation, Pulsed Laser Deposition (PLD), Radio Frequency

(R.F) Magnetron Sputtering, Direct Current (DC) Magnetron sputtering etc. Despite above-mentioned techniques, the initial material in all the cases is in the form of solid, which need to be evaporated under a high vacuum and followed by capturing onto a substrate. The source of heating, which accomplishes the evaporation is different in all the techniques. As an example: for PLD, the laser source is used, for RF magnetron sputtering radio frequency is utilized, for thermal evaporation Joule's heating is used to evaporate the target material. The unique advantage of the evaporative techniques is the 'purity' of the end films, which directly affects the electronic properties of the thin films. Thus, evaporative based techniques have gained tremendous importance in the commercial electronic industries. However, there are challenges associated with evaporative techniques, such as the requirement of high vacuum, limitation of substrate size etc. To address these issues effectively, a parallel low-cost processing technique has made its impression called 'solution processing' (Pasquarelli et al. 2011; Fortunato et al. 2012).

2.9 Solution processing

According to Moore's law, the transistors have doubled in number every 18 months. However, the cost of the microelectronic chip per unit area has remained relatively the same in the past three decades. Thus, it becomes crucial to mitigate the cost to a minimum possible value by adopting inexpensive alternate solution-based techniques. It is fascinating to note that the invention of solution processing was way before the evaporative techniques. L. Gordon and his research colleagues during conduction of the gravimetric analysis through precipitation had observed transparent layers retained on the inner surface of the glass on the beaker (Gordon 1952; Gordon 2000). These transparent layers are the thin films adhered at the bottom of the glass beaker and opened up an area of understanding the nature of these films and their implications (Gordon et al. 1959). This accidental invention led the area of solution processing, but the electronic properties of the solution processed films depend on a range of parameters such as type and composition of precursors, deposition method, the temperature of annealing, time of annealing etc. The general method of solution deposition is basically of two kinds: (a) through colloidal nanoparticle solution and (b) via molecular precursor deposition. In both the cases, the precursor solution is modified

accordingly, but the deposition techniques adopted for these precursors remain unchanged. They are spin coating, spray coating, dip coating, chemical bath deposition, inkjet and screen printing mention a few. Fig. 2.15 shows the schematic of the solution processing which includes, precursor type and the coating methods generally adopted for the solution processed thin films. It is worth mentioning about the sequences of the solution deposition of thin films, they are: (a) precursor designing (b) formulation of coating solution, (c) deposition of thin films, (d) thermal annealing of thin films. Following subsections will be dedicated to these sequences of processing.
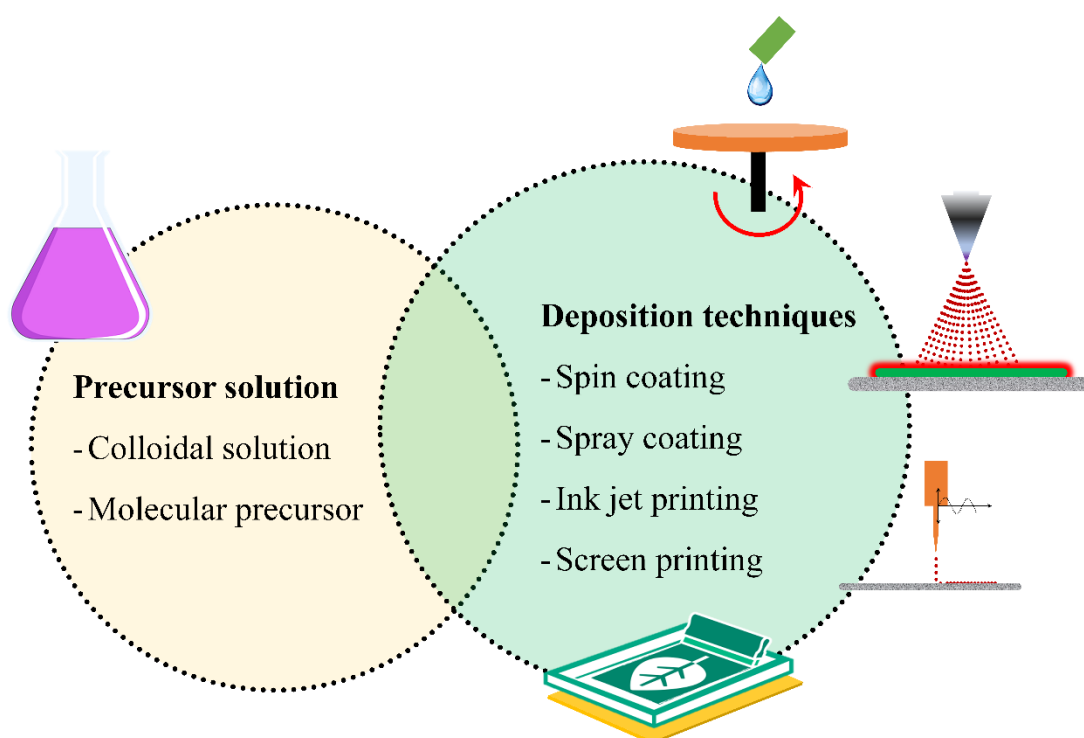
Fig. 2.15 Type of the precursor and the techniques of film fabrication adopted in solution-processed thin films.

2.9.1 Designing the precursor

In the case of colloidal dispersions, nanoparticles are dispersed into a solvent along with the surfactant, and the resulting solution is used for the thin film fabrication processes using different deposition techniques. However, designing the molecular precursors is more complicated and need more understanding of the chemistry. The reagents containing the required cations are made to undergo a chemical reaction in as-

deposited films, which results in the form of dense metal oxide films under suitable thermal processing. The selection of the precursor depends on the type of solvent employed in solution preparation and the processing route. The chemical reagents are the solute and need to dissolve in the solvent to form a clear, stable and homogeneous precursor (Pasquarelli et al. 2011). Many of the cases, where two or more solvents are required to achieve a clear and homogeneous solution. Chemical reagents are mainly metal salts such as chlorides, acetates, nitrates, acetylacetonates and so on. As an example, zinc acetate is more popular compared to nitrate, but when it comes to the other cations such as indium and tin, nitrates and chlorides are preferred over acetates and acetylacetonates because of their ease of dissolution and compatibility with other metal salts and the solution. Chlorides, acetates, and nitrates are readily available in the market and need no purification before the use. Along with commercially available metal salts, laboratory-synthesized complex precursors have also been used in the literature; such as, carboxylates (Dippel et al. 2007), Organometallics (Roth and Williams 1981), homometallic Alkoxides (Okamura and Bowen 1986), oxo-alkoxides (Westin et al. 1998), beta-diketonates (Pasquarelli et al. 2011), ammine hydroxy nitrates (Meyers et al. 2008), heterometallic alkoxides (Pasquarelli et al. 2011).

2.9.2 Formulation of the coating solution

After the selection of the precursor, the next step is to formulate the solution, which needs to be coated. The preparation of solution needs an intelligent selection of the solvent. In the case of the formulation of nanoparticle-dispersed colloidal solution, there is a need for surfactant or capping agent. The surfactant ensures the high degree of dispersion of nanoparticles in the solution. It is essential to have a high mass loading of nanoparticles in the solution to achieve dense films. The advantage of nanoparticle-based formulations is that the thermal energy required for the fabrication of thin films is comparatively lower because the nanoparticles are pre-synthesized (Talapin et al. 2009). Moreover, it is barely not advisable to employ nanoparticle-based colloidal formulations for oxide films because of poor density of coated thin films (Pinna and Niederberger 2008). However, applications demanding porous network of the particles, can be fulfilled by the metal oxide nanoparticle-based colloidal formulations (Pasquarelli et al. 2011). On the other hand, the fundamental advantage of molecular

precursors is that they result in the amorphous metal oxides (Pasquarelli et al. 2011). Thus, gained popularity in depositing metal oxide semiconductors also opened up a new area of research on amorphous TCOs. Initially, a stable suspension is formed after the alkoxides in the precursor undergoes hydrolysis and poly-condensation reactions forming the stable suspension of particles termed as 'the sol'. Further, the sol evolves to a porous polymeric network called 'the gel'. The solutions that undergo such events are classified as 'sol-gel' precursors (Pierre 1998). The process of formation of the polymeric complex is called 'gelation', which is a time-dependent phenomenon and the time-span is called 'aging'. The result of the aging process is the formation of metal-oxygen-metal (M-O-M) and metal-hydroxide-metal (M-OH-M) bridging through the process of condensation via which water and alcohol removal takes place, as shown in the fig. 2.16 (Pasquarelli et al. 2011). It is worth mentioning that the gelation may result in the 3D networks or the stable suspension of colloidal particles depending on whether the reaction is backed by the base or acid catalyst, respectively (Lewis 2000).
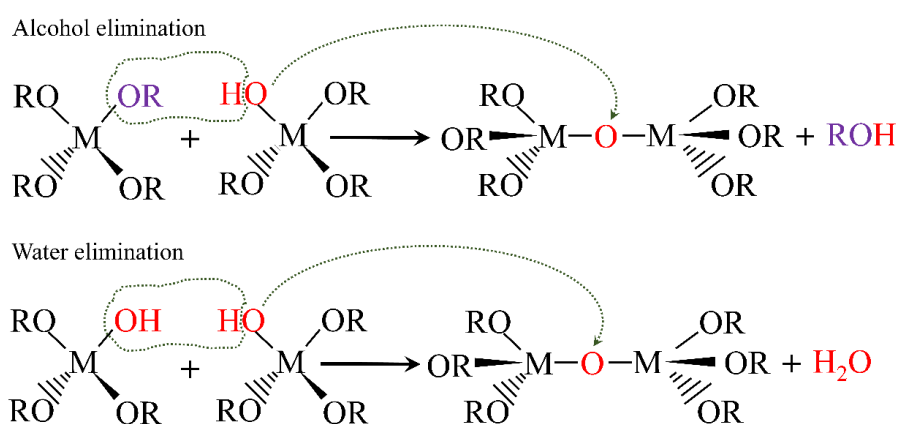
Fig. 2.16 Reactions depicting the elimination of alcohol and water.

Modification in the sol-gel route is the Pechini method (Pechini 1967), first reported in 1967. In this method, inexpensive metal nitrates are used instead of alkoxides along with multi carboxylic acids such as citric acid. The cations from the metal nitrates and carbonates undergo chelation with multi carboxylic acids. Multiple chelation events result in the formation complexes, which constitute the organic matrix with distributed metal cations. Thus, due to high organic loadings, the problem of shrinkage in the mass becomes severe. To reduce undesirable shrinkages, the combined

approach has also been reported, where a combination of nanoparticle-molecular precursor routes also reported with a high percentage loading of nanoparticles, which accounts for the mass loss. The combined approach is well reported for multiple cation-based photo absorbers (Todorov et al. 2010).

2.9.3 Deposition of thin films

The solution processing allows the deposition of thin films at atmospheric pressure, with minimum or no sophistication. A wide range of deposition techniques have emerged, and few of them are commercialized successfully for high throughput and large area deposition. In the present section, few of such deposition techniques are elaborated. The deposition of high-quality thin film needs proper attention to various aspects such as deposition rate, post-processing of as-deposited film, and deposition conditions. The broad classification of the deposition methods is: (a) direct growth of the desired material on the substrate of interest and (b) coating of precursor demanding post-processing to make the as-deposited film, free from organic carriers.

Under the direct growth of the material, the most widely adopted technique is chemical bath deposition, where an immersed substrate in the solution-bath containing the desired composition of the material. The substrate acts as the heteronomous nucleation site for the growth of the material (Hodes 2002). Another category is the solution coating, which is most popular. Due to reproducibility and ease of coating, the second classification is mostly used for a wide range of materials including both unary and doped metal oxides. Spin coating is one among them, where the solution is dispensed on to the substrate held by vacuum chuck of the spin coater. After the spin-off, a thin and uniform film persist onto the substrate and gives rise to the desired product after the post processing (Yang and Jiang 2010). Similar is the case with dip coating, where successful dipping and retrieving the substrate from the precursor makes the solution to adhere. A proper withdrawal rate results in the adhered thin film on the substrate (Brinker and Scherer 2013).

The spray coating is a non-contact, large area deposition technique, where atomized droplets of the precursor sprayed on the substrate. If the temperature of the substrate maintained higher than that of the decomposition temperature of the

precursor, then the atomized droplets touching the substrate undergo decomposition and successful sintering to form a uniform film. The solution is sprayable if the viscosity of the solution is less than 10 cP (Perednis and Gauckler 2005). However, demand in optoelectronics is mainly concentrated on the patterned films rather than the continuous thick films. Screen printing and stamping are two techniques, which allow the direct patterned deposits. However, these require massive forces and viscous solutions. Inkjet printing and direct-wire techniques avoid the patterning requirement and result in the maximum utilization of the precursor without wastage. Also, the inkjet printing allows the stacking of multi-layers of different materials, which helps in the complete device fabrication (Magdassi 2010). The drawback of the inkjet nozzle is its clogging, if the precursor consists of colloidal nanoparticles (Magdassi 2010). All the above-mentioned processing of the films is in the wet state, which requires thermal processing. The thermal-assisted decomposition of the film takes place, which leaves behind the dense film. The coated precursors do resemble the sol-gel on the substrate. Thus, before thermal processing of coated wet films needs to be aged to promote gelation in the film. The aging of the wet films can be accomplished in the proper atmosphere with well-maintained conditions such as moisture (Pasquarelli et al. 2011).

2.9.4 Annealing of coated thin films

The final and essential step in realizing the fabrication of thin film is the thermal processing step. There are mainly three reasons of thermal processing: (a) to decompose the precursor and fetch out organic impurities, (b) to impart crystallization and formation of desired phase, and (c) to control carrier concentration through formation and elimination of defects. For semiconductors, the crystallization is not necessary, and there should be a strict hold over the formation of defects. However, in the case of transparent conductors the formation of defects such as native oxygen vacancies lead to the enhancement in the electrical conductivity (Pasquarelli et al. 2011). The first step is the most essential and decisive, when it comes to purity and the densification of the film. Dense films show improved properties such as dielectric response and low leakage current (Liu et al. 2018). Irrespective of the type of precursors whether nanoparticle-colloidal ones or molecular precursor, the decomposition and impurity removal step need to be successfully fulfilled with higher yield. Spray pyrolysis is being an exception

where, the events such as precursor decomposition, impurity removal, and formation/elimination of defects are not attributed seperately (Schneller et al. 2013). Further, the control over carrier concentration is crucial in the case of metal oxide semiconductors. On the other hand, carrier concentration plays a crucial role in TCOs. Thus, post-processing or secondary annealing becomes essential, where the annealing in reducing atmosphere is preferred. The reducing atmosphere has the mixture of nitrogen and hydrogen ($N_2:H_2$), which results in the generation of carriers.

The thin films fabricated via nanoparticles-based solution required to be made free of organic capping agents and process is termed as 'curing'. The cured film, which is free of organics leads to the physical contact of the particles because of which the particle network shows probable percolation paths. If the dense film is desired, then sintering of the particles become essential. Thus, both curing and sintering are two facets of the thermal processing of films fabricated via nanoparticle-based colloidal solutions. The solution processing is summarized in fig. 2.17, which includes both molecular precursor and the colloidal nanoparticle route. In addition, the morphological development of the deposited film via colloidal nanoparticle route, mainly depends on the movement of particles driven by solvent evaporation. The subsequent section deals with the morphological evolution of films deposited via nanoparticle dispersed colloidal solution.

2.10 The colloidal dispersion of nanoparticles

The nanoparticles with uniform size dispersed in the medium with the help of capping agents lead the formation of a stable colloidal solution. The solvent medium utilized for dispersing the nanoparticles generally has a low boiling point, and the capping agent possesses a heterostructure composed of both hydrophilic and hydrophobic parts. The hydrophobic part attaches to the nanoparticle and forms a micelle with self-assembled monolayer, and the repulsive forces between micelles restrict the agglomeration of nanoparticles and keep them dispersed. The formulated colloidal dispersion is used for the fabrication of thin film. The deposited colloidal solution undergoes solvent evaporation followed by the removal of capping agent under supplied thermal energy. Noble metal nanoparticles such as silver, gold, platinum,

palladium are used often in the formulation of colloidal dispersions (Kamyshny et al. 2014), while other metal nanoparticles such as copper can be stabilized to form colloidal ink.
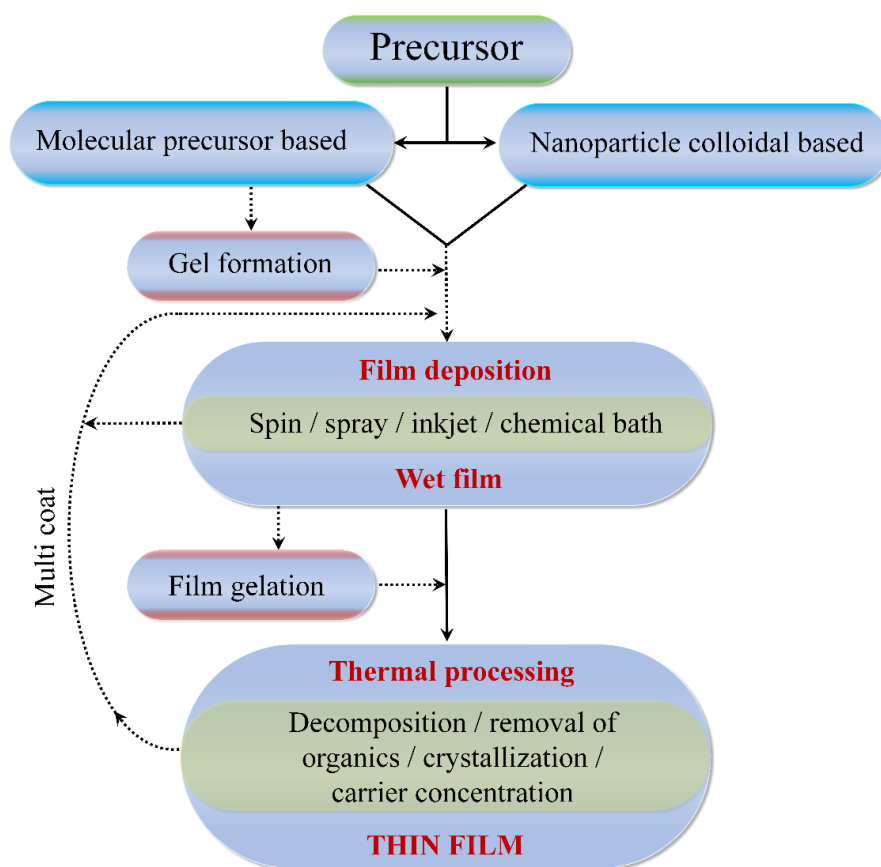
Fig. 2.17 Summary of the solution-processed thin films.

The critical aspect of being noted is that the evaporation caused morphological development of the resulting film is not straightforward. The drop of colloidal solution on a substrate undergoes evaporative mass transfer at the pinned edge promoting replenishment of the solvent from the middle of a drop to the edge to compensate for the mass loss governed by 'law of conservation of mass'. The outward flux of solvent in the radial direction of the drop called capillary flow (Deegan et al. 1997).

2.10.1 Morphological evolution of the deposited films

The type of flow plays a crucial role in deciding the end morphology of the film produced out of colloidal solution. Because, the movement of fluid particles solely

guides the formation of the film through nanoparticle rearrangement. In the case of outward capillary flow, the fluid particles carry the solid, immobile nanoparticles towards the pinned edge of the drop, which is getting evaporated continuously with time. Post evaporation of the solvent, the retained assemblage of nanoparticle, which is physically in contact with each other resembles a coffee stain. Thus, the effect is popularly known as the 'coffee ring effect'. Fig. 2.18 shows the nature of ring deposit of the nanoparticle along with the flow pattern within the drop during the evaporation.
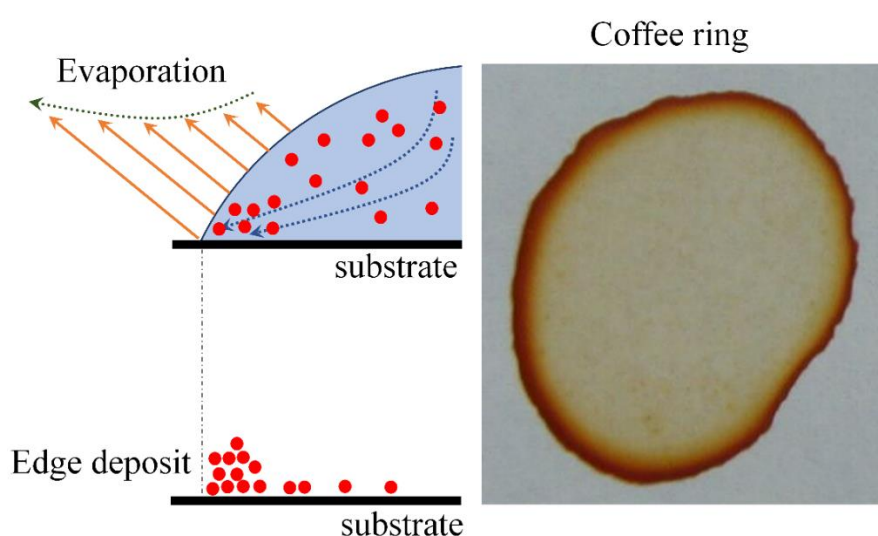
Fig. 2.18 Evaporation of the solvent from the drop, resulting in edge deposit of the nanoparticles, and photograph of the coffee ring.

The capillary flow dominates the criteria for the formation of edge deposit, with a negligible surface flows such as Marangoni. The increased surface flow can reverse the coffee ring effect. Thus, the phenomena came into existence after the discovery of the effect of intense Marangoni flux on the morphology. The resulting pattern is completely reverse, and termed as the 'dot' (Hu and Larson 2006). Both 'coffee ring' and the 'dot formation' are the two extremities of the morphologies obtainable from the evaporation of a drop of colloidal solution. It is essential to overcome these extremities to achieve uniform deposition of the nanoparticles onto the substrates (Soltman and Subramanian 2008). Previously few attempts were made in terms of optimizing the distribution of the size of nanoparticles, the chemistry of the solution, and annealing

temperature to achieve uniform deposition of the nanoparticles (Soltman et al. 2010; Perelaer et al. 2010).

2.11 Low-temperature processing

Further, irrespective of whether the precursor is nanoparticle-based or the molecular precursor, thermal processing is vital in achieving dense and continuous film. as the temperature of annealing is selected based on the decomposition of constituents of the initial precursor (Pasquarelli et al. 2011). In the case of molecular precursor route, metal salts are the sources of metal cations and decomposition of the same lead to the formation of the continuous and periodic framework of the metal-oxygen-metal network. Periodicity in the network is termed as 'crystalline metal oxide'. Several methods have been illustrated to reduce the temperature of processing by adopting modifications in the chemistry of the solution such as 'sol-gel on-chip' (Banger et al. 2011) and combustible precursor (Kim et al. 2011b). As a model example of combustible system is zinc nitrate and urea, as explained by Kim et. al. Besides, the modification in the annealing techniques such as ultraviolet annealing (Kim et al. 2012) rather than conventional thermal annealing has also shown promising performance.

In the case of combustible precursors, the solution comprises a pair of fuel and oxidizer, which undergo exothermic reaction resulting in the evolution of heat. The fuel-oxidizer couple is called redox mixture, which undergoes a chemical reaction at a temperature as low as 200 °C or less (Varma et al. 2016; Patil et al. 2008a). The exothermic reaction between the fuel and the oxidizer brings up the change in the enthalpy, which is attributed to the heat. Thus, the generation of localized heat gives rise to a natural decomposition of the metal nitrates leaving behind the desired metal oxide. Forthcoming sections will explain the thermodynamics involved in the combustion techniques and the importance of balanced combustion reaction, and relative amounts of fuel and oxidizers.

2.11.1 Combustion thermodynamics

The exothermic reaction between the fuel and the oxidizer is generally attributed to the conventional burning. The process of burning of the redox pair results in the

energy-heat outcome. The essentials of the reaction can be presented in the form of a triangle called 'fire triangle' (fig. 2.19). The enthalpy of the reaction ($\Delta H_{reaction}$) can be calculated from the Hess' law and estimated via thermal analysis of the precursors. The area under the DSC thermogram quantifies the enthalpy. For an open system, the first law of thermodynamics can be written as:

$$\delta Q - \delta W = dH_{reaction} \tag{2.9}$$

where, δQ, δW, and dH are heat transfer, work transfer, and change in the enthalpy of the reaction. The combustion reaction is spontaneous and exothermic. The rise in temperature of the products of the combustion in a short period makes the system adiabatic ($\delta Q = 0$). In the case of combustion processing of materials, $\delta W = 0$. Thus, the resulting equation is

$$dH_{reaction} = 0 \tag{2.10}$$

on integrating equation 2.10, within the limits of H_R (enthalpy of reactants) and H_P (enthalpy of products)

$$\Delta H_{reaction} = (H_P - H_R) = 0. \tag{2.11}$$

On plotting the equation 2.10 in the thermodynamic plane of enthalpy vs. temperature (fig. 2.19); after the commencement of the reaction, the products attain higher temperature (T_{ad}). On revisiting the equation 2.9; with proper consideration of sign convention (heat transfer from system to surrounding: negative):

$$-\delta Q = dH_{reaction}$$

$$Q_{R \to P} = \Delta H_{reaction} = (H_P - H_R) < 0. \tag{2.12}$$

For exothermic reactions, 'the enthalpy of the reactants is higher than the enthalpy of the products and difference is the amount of heat transfer from the system to the surrounding at constant pressure.' In order to determine the maximum temperature achieved (adiabatic flame temperature: T_{ad}) by the products of the combustion (Patil et al. 2008a), the change in enthalpy of the reaction can be reconsidered as presented in the equation 2.13.

$$dH_{reaction} = C_P dT \tag{2.13}$$

where C_p = specific heat at constant pressure. Integrating equation 2.13, on both sides

$$\Delta H_{reaction} = \int_{298\ K}^{T_{ad}} \Delta C_{P(Product)}\ dT \qquad (2.14)$$
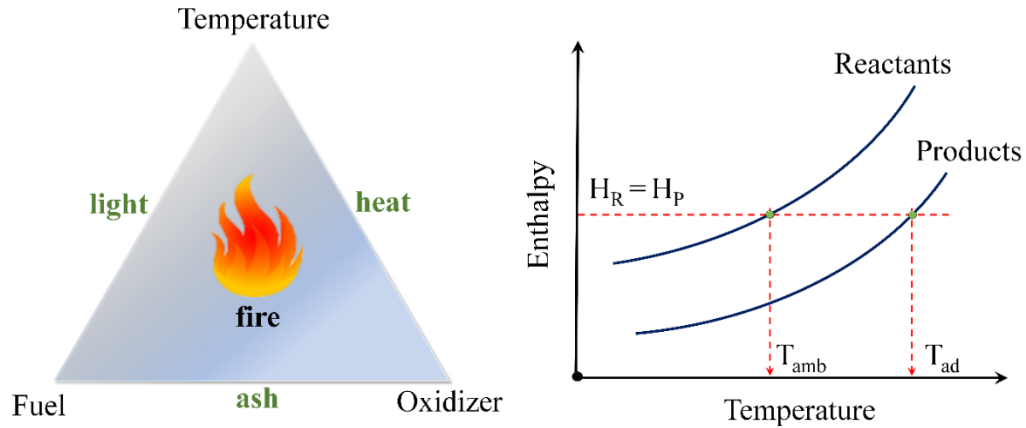
Fig. 2.19 Thermodynamics of combustion reaction: (a) fire triangle and (b) nature of enthalpy vs. temperature plot for a chemical reaction.

The value of T_{ad} is defined as the 'exothermicity' of the combustion reaction. The magnitude of exothermicity is maximum if the reactants of the combustion are mixed in the balanced stoichiometry. The deviation in the stoichiometric amounts of oxidizers and fuel can lead to a reduction in the exothermicity. The stoichiometric quantity of the combustible elements is always specified by the ratio of fuel to oxidizer. If ϕ is the fuel to oxidizer ratio (F:O) then it can be defined from the equation 2.15, the method of determination of ϕ is called Jain's method (Jain et al. 1981)

$$\phi = \left(^{RV}/_{OV}\right) \times n \qquad (2.15)$$

where, RV, OV, and n are reducing valency, oxidizing valency and the number of moles of fuel per mole of an oxidizer respectively. The combustible elements are considered to be stoichiometric when $\phi = 1$, lean-fuel when $\phi < 1$ and excess-fuel when $\phi > 1$. Following example demonstrates the method of determination of 'n' (equation 2.15). The combustion mechanism of zinc nitrate with fuel glycine is presented as:

Zinc nitrate :: $Zn\ (NO_3)_2$ :: OV = $(+2) + (0 \times 2) + (6 \times (-2)) = -10$,

Glycine :: $C_2H_5NO_2$ :: RV = $(2 \times (+4)) + (5 \times (+1)) + (0 \times (+1)) + (2 \times (-2)) = +9$,
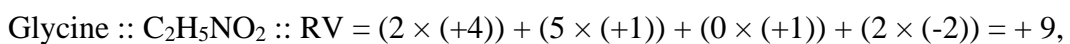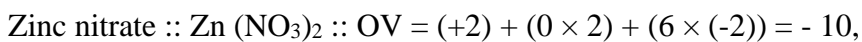
using equation 2.15, the value of 'n' turns out to be 1.11 for the stoichiometric mixture of zinc nitrate and the glycine. Thus, 1.11 moles of glycine is required for one mole of zinc nitrate to yield maximum energy output in the form of heat. The value of 'n' can be further plugged into the chemical reaction (equation 2.16).

$$\textbf{1 } Zn(NO_3)_2 + \textbf{10/9 } C_2H_5NO_2 \xrightarrow{\hspace{1cm}} \textbf{1 } ZnO + \textbf{20/9 } CO_2 + \textbf{14/9 } N_2 + \textbf{25/9 } H_2O \qquad (2.16)$$
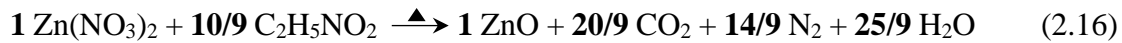
The coefficients of zinc nitrate and glycine are '1' and '10/9' respectively. The equation 2.16 can be extended for any metal nitrate and fuel redox couple. If $M^{+\upsilon}(NO_3)_\upsilon$ is the metal nitrate with cation-M having a valency '+υ,' then the OV can be calculated as follows:

$$OV = (+\upsilon) + (0 \times (+\upsilon)) + ((-2) \times 3 \ (+\upsilon)) = -5\upsilon$$

Moreover, RV of glycine is estimated to be '+9', thus from the Jain's method (equation 2.15) the number of moles of fuel per mole of oxidizer (n) becomes '5υϕ/9'. The redox chemical reaction can be written in the form of two independent reactions namely (a) formation of metal oxide from metal nitrates or the reduction of metal nitrate into metal oxide and (b) oxidation of the fuel into carbon dioxide and the water vapor. Fig. 2.20 shows the complete derivation of the general combustion reaction involving metal nitrate and glycine as the oxidizer and the fuel, respectively. The final equation is the function of F:O ratio. Interestingly, the coefficient of molecular oxygen on the reactant side tends to zero as ϕ tends to unity (fig. 2.20). This implies that during the commencement of the reaction no molecular oxygen from the atmosphere is necessary (Branquinho et al. 2014) and the reaction is sustaining with the oxygen provided by the oxidizer. However, any deviation in the value of ϕ leads to incomplete combustion. The flow chart presenting different values of ϕ and the consequences is shown in fig. 2.21. It is interesting to know that the stoichiometric mixtures of fuel and the oxidizers result in the maximum heat output or the maximum exothermicity because of the absence of unburnt hydrocarbons. Thus, the stochiometric redox mixtures of generally preferred.

2.11.2 Comparison between combustion and sol-gel processing techniques

The formation of metal oxide is also possible under the continuous supply of thermal energy to the metal salts. The value of ϕ ensures the successful conversion of

metal nitrate (or salts in general) into a metal oxide. The decomposition temperature plays a decisive role in the formation of metal oxide, which is reported to be around 400-450 ºC (Kang et al. 2014; Pasquarelli et al. 2011).

Reduction of metal nitrate into metal oxide

$$M^{+\upsilon}(NO_3)_\upsilon \longrightarrow MO_{\upsilon/2} + (\upsilon/2)\, N_2 + (5\upsilon/4)\, O_2$$

Oxidation of fuel

$$n \times [C_2H_5NO_2 + (9/4)\, O_2 \longrightarrow 2\, CO_2 + (1/2)\, N_2 + (5/2)\, H_2O]$$

adding both the equations

$$M^{+\upsilon}(NO_3)_\upsilon + n\, C_2H_5NO_2 + 1/4\, (9n - 5\upsilon)\, O_2 \longrightarrow$$

$$\longrightarrow M^{+\upsilon}O_{\upsilon/2} + 2n\, CO_2 + ((\upsilon+n)/2)\, N_2 + (5n/2)\, H_2O$$

substituting $n = (5\phi\upsilon / 9)$ in the above equation

$$M^{+\upsilon}(NO_3)_\upsilon + (5\phi\upsilon / 9)\, C_2H_5NO_2 + 5\upsilon/4\, (\phi-1)\, O_2 \longrightarrow$$

$$\longrightarrow M^{+\upsilon}O_{\upsilon/2} + (10\phi\upsilon / 9)\, CO_2 + (\upsilon /18)(5\phi+9)\, N_2 + (25\upsilon\phi /18)\, H_2O$$
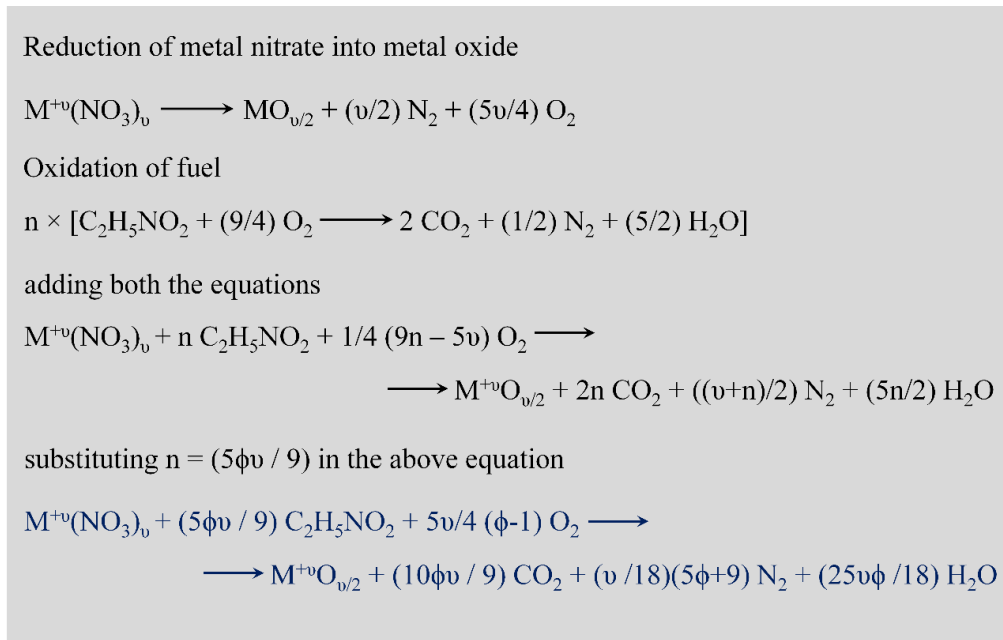
Fig. 2.20 Derivation of general combustion reaction comprising metal nitrates and the fuel-glycine as the function of ϕ.

F:O ratio (ϕ)

$\phi < 1$	$\phi = 1$	$\phi > 1$
o Fuel lean.	o Stoichiometric mixture.	o Fuel rich
o More oxidizer.		o Requires molecular oxygen for the complete burning.
o Formation of molecular oxygen.	o Formation of CO_2, H_2O and N_2.	
o Increased amounts of gaseous products.	o Maximum heat output.	o Low heat output.
o Low heat output.		o Can result in the retainment of unburnt hydrocarbon.

Fig. 2.21 Effect of ϕ on the combustion reaction.

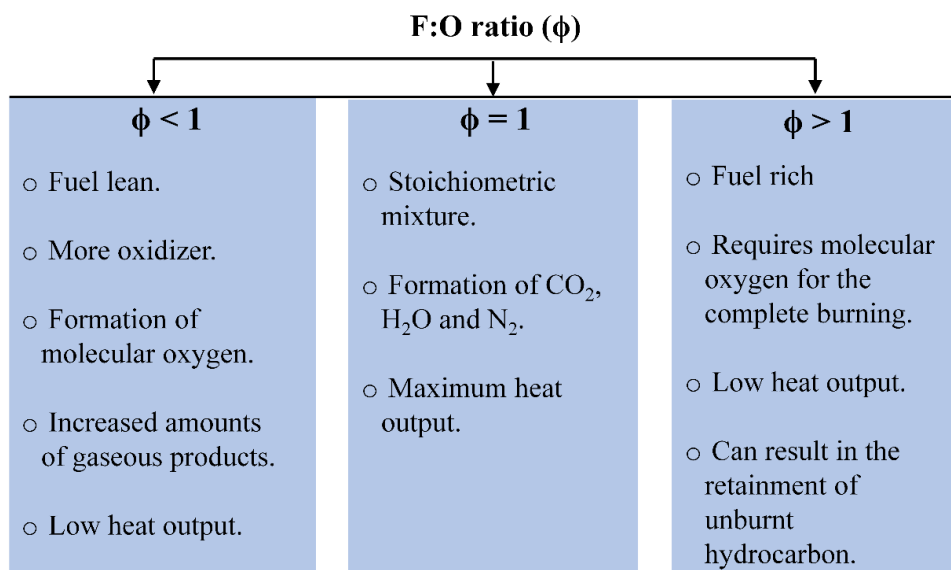The activation barrier for the transformation of metal salts into metal oxides is higher for conventional, such as sol-gel processing compared to combustion. Fig. 2.22 shows the variation of energy to the reaction coordinate for both sol-gel and combustion reactions. The decomposition of sol-gel precursors is an endothermic event, whereas the combustible ones are exothermic. The maximum temperature (T_{ad}) achieved during the combustion reaction is high, as an example: for stoichiometric ($\phi = 1$) nickel nitrate-glycine system it is around 1076 K with a supplied energy having a temperature equivalent to 300 K (Varma et al. 2016). Similarly, for stoichiometric aluminum nitrate-urea $T_{ad} = 1700$ K (Patil et al. 2008a). The T_{ad} exists only for a short period (fig. 2.22).
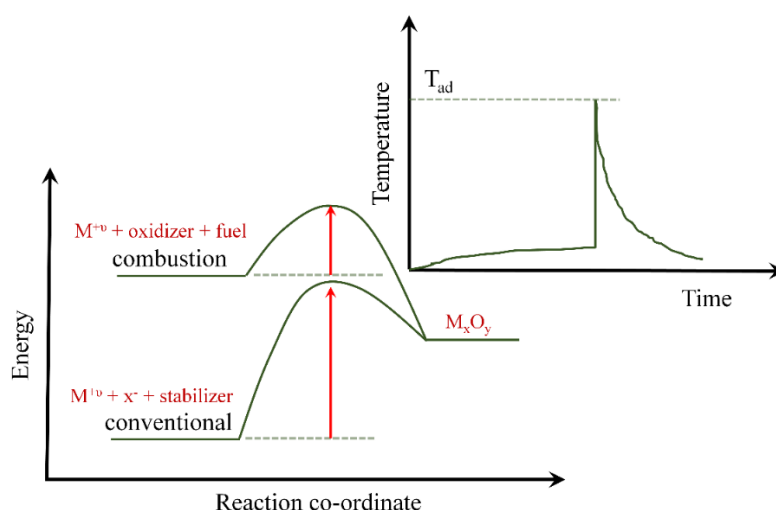

Fig. 2.22 The plot of energy vs. reaction co-ordinate showing the comparison of conventional sol-gel and combustion reactions.

2.11.3 Solution combustion

The combustible elements namely the fuel and the oxidizer (metal nitrates) are to be dissolved in a medium called solvent, which is either aqueous or organic. Series of solvents have been reported such as ethanol, menthol, 2-methoxyethanol, formaldehyde, kerosene, etc. An ideal solvent should dissolve a series of metal nitrates and also should have large range of solubilities. Focusing on another vital ingredient, which is the fuel. There is a broad spectrum of fuels, which are dissolvable in different solvents and shows the compatibility with the metal nitrates. All hydrocarbons are fuels, and also few compounds containing nitrogen can also serve the purpose of being

reducing agents or fuels such as hydrazine (N_2H_4). The reason for the exothermicity of these fuels is due to N-N bonds, which breaks into N_2 ($N \equiv N$) through exothermic decomposition. Fig. 2.23 summarizes the criteria of a chemical compound being fuel along with a few well-known fuels. The solution constituting all combustible elements is called "combustible precursor," which can further be utilized in two distinct ways namely (Cochran et al. 2017) (a) bulk-powder synthesis and (b) thin film fabrication. Bulk-powder synthesis has been extensively addressed by many research groups (Patil et al. 2008a; Varma et al. 2016).
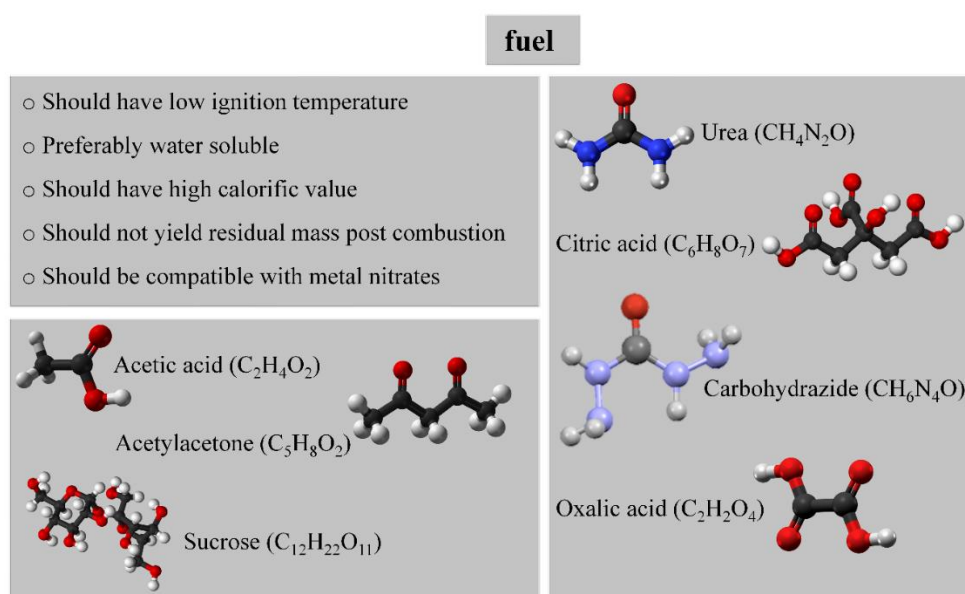

Fig. 2.23 Criteria of an ideal fuel and the list of different fuels.

However, the fabrication of thin films from combustible precursors is relatively new and first reported in the year 2011 (Kim et al. 2011b). Irrespective of the type of the product, the combustion reaction entails clear and homogeneous precursors. The initial solution is utilized for the fabrication of thin films using various deposition techniques such as spin coating, spray coating, dip coating, inkjet printing as mentioned in the previous section. The as-casted films yield metal oxide as product at a low temperature, which promotes the process compatibility with thermal sensitive substrates.

2.11.4 Evidence of combustion

The combustible precursors undergo exothermic reaction at a fixed temperature forming gaseous byproducts. Both thermogravimetric analysis (TGA) and differential scanning calorimetry/differential thermal analysis (DSC/DTA) provide the evidence of combustion reaction. The TG-thermogram shows an intense and sudden mass loss at a fixed temperature. The vertical drop of the curve having maximum slope can be assigned to the evolution of the gaseous impurities and corresponding DSC/DTA curve at same temperature reveals the cause of the mass loss. The typical nature of TGA and DSC/DTA curves is depicted in fig. 2.24. Also, the amount of heat energy interaction can be quantified by integrating the area under the DSC response, which is nothing but the change in enthalpy (ΔH) at constant pressure (Chen et al. 2018a).

$$\Delta H = \int_{T_1}^{T_2} Q(T)dT = \int_{298}^{T_{ad}} \Delta C_{p(product)} dT$$

C.T = Combustion temperature
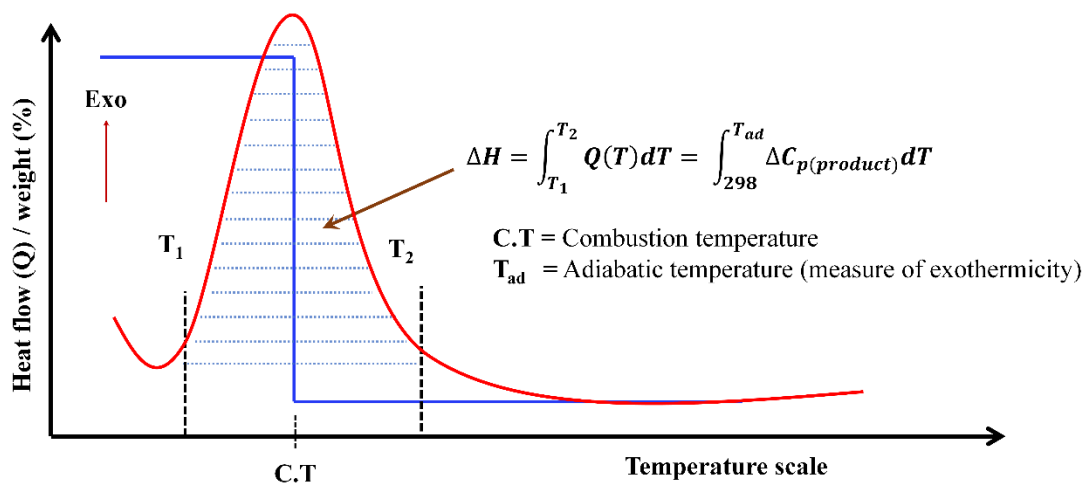T_{ad} = Adiabatic temperature (measure of exothermicity)

Fig. 2.24 Nature of TGA (blue curve) and DSC (red curve) thermograms for a combustion reaction at a fixed temperature (C.T: combustion temperature).

2.11.5 Solution combustion derived thin films

The combustible precursors are used for film fabrication. In literature, spin coating (Hennek et al. 2012; Hennek et al. 2013; Branquinho et al. 2014; Chen et al. 2018b), spray coating and inkjet printing (Kim et al. 2011b; Everaerts et al. 2013) are reported via combustible precursors, among which spray combustion has shown high performance approaching the quality of sputter deposited films (Yu et al. 2015; Wang

et al. 2016a). Owing to the high surface area of the atomized droplets facilitates the formation of metal oxide with great ease. Thus, the resulted film out of spray combustion is purer compared to spin-coated ones. The first report on the feasibility of combustion processing in fabricating thin films is established to deposit In_2O_3 and commercial grade ITO (Kim et al. 2011b). Further, the well-known metal oxide semiconductor IGZO is deposited via spray combustion (Yu et al. 2015). After these inventions, there are numerous articles that have been published in the past eight years in various disciplines of Science and Engineering. Fig. 2.25 provides an idea of number of Scopus-indexed articles published from various parts of the globe. These articles specifically address the solution combustion derived metal oxides for the components of TFTs. Also, fig. I-c (Appendix I) shows the percentage of published articles on solution combustion derived metal oxide thin films by different branches of science.
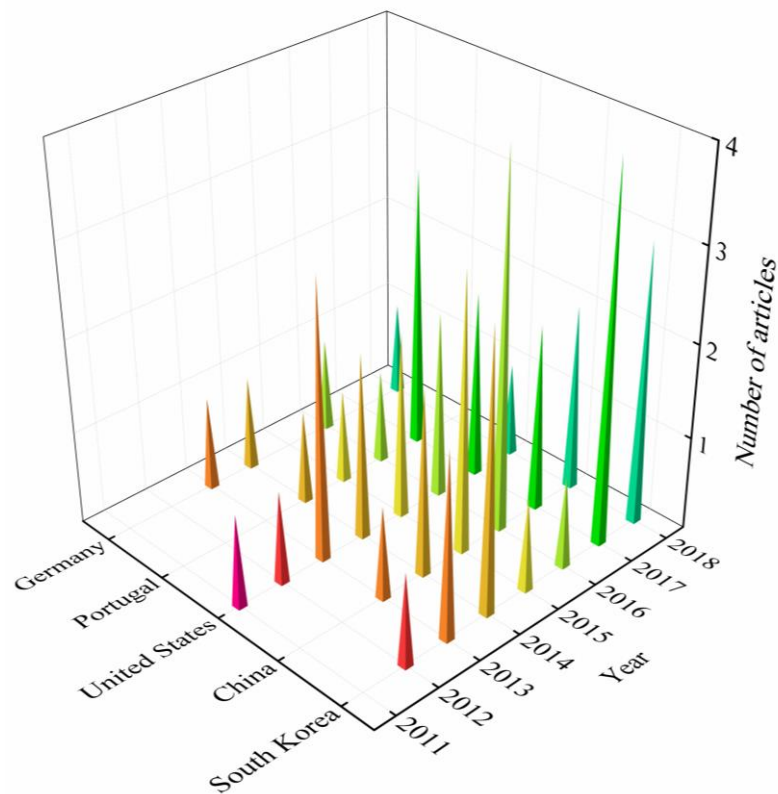

Fig. 2.25 3-Dimensional plot showing the number of Scopus-indexed articles per year from different countries specifically on combustion derived metal oxide thin films in optoelectronic devices, especially TFTs.

Although combustion processed thin films have gained considerable scientific attention, the mechanistic understanding of combustion reaction in thin films is still unclear (Wang et al. 2016a). In this regard, the thermal analysis of the as-spun precursors is carried out and found no evidence of combustion in thin films and it is supported by TGA/DTA. Results revealed that the mass loss as the function of temperature is continuous rather than sudden or drastic as observed in the bulk-powder combustion synthesis (Sanchez-Rodriguez et al. 2013). If the metal nitrate possesses low decomposition temperature then thin films yield metal oxide at low temperatures irrespective of the fuel additive, due to high surface to volume ratio (Cochran et al. 2017).

2.11.6 Device performance: low-temperature combustion processing

Series of TFTs were fabricated using a low-temperature solution combustion. Different materials ranging from unary oxides to ternary oxides have been reported. Table 2.5 depicts the different devices along with their performance parameters. The set of performance parameters presented in table 2.5 are reported at the low processing temperature ($\leq 350\ ^\circ$C). The efficacy of combustion processing is fetched in realizing the metal oxide at low temperatures. The device performance can further be enhanced by high-temperature processing (~450 to 500 $^\circ$C) due to improved densification and modulated defect chemistry of the film (Kim et al. 2011b; Fortunato et al. 2012). The combustion processed metal oxide semiconductors show an acceptable performance compared to high temperature sol-gel processed ones (table 2.6).

Table 2.5 Performance of different TFTs with combustion processed semiconductors.

MOS	Fuel	T_P	Performance parameters of TFTs			Ref.
		(°C)	Mobility $(cm^2V^{-1}s^{-1})$	V_{th} (V)	$I_{on}:I_{off}$	
IGZO	Urea	350	3.1	4.3	$\sim 10^7$	Sanctis et al. 2018
In_2O_3	Ac	200	0.81	2.0	$\sim 10^6$	Kim et al. 2011b
IZO	Ac	225	0.32	10.0	$\sim 10^6$	Kim et al. 2011b
LNO	Ac	150	3.15	5.47	$\sim 10^3$	Yang et al. 2018
In_2O_3	Urea	180	1.26	0.53	$\sim 10^4$	Carlos et al. 2016
IGZO	Sugar	300	3.15	10.3	$\sim 10^7$	Wang et al. 2016b

MOS: Metal oxide semiconductor, Ac: Acetylacetone, T_P: Processing temperature, LNO: lithium doped nickel oxide.

Table 2.6 Performance of different TFTs with sol-gel processed semiconductors.

MOS	T_P	Performance parameters of TFTs			Ref.
	(°C)	Mobility $(cm^2V^{-1}s^{-1})$	V_{th} (V)	$I_{on}:I_{off}$ ratio	
ZTO	500	0.6	1.0	$\sim 10^6$	Park et al. 2009
IZO	450	6.0	-0.3	$\sim 10^9$	Park et al. 2010
IGZO	600	1.3	5.3	$\sim 10^4$	Xiong et al. 2010
IGO	400	0.87	-4.1	$\sim 10^3$	Jeong et al. 2011
ZnO	500	0.1	17.1	$\sim 10^5$	Huang and Hsieh 2010

MOS: Metal oxide semiconductor, T_P: Processing temperature.

2.12 Objectives of the present study

The objective of the present study embodies the fabrication of uniform, smooth and well adhered thin films of metal oxides for the applications such as transparent conducting oxides, transparent semiconducting oxide via low temperature solution

combustion processing technique. In addition, it is extended to the metallic silver. Also, the morphological challenges related to nanoparticle-based inks are addressed.

☞ To fabricate the conducting and transparent ITiO ($In_{14}TiO_{23}$) and IZTO ($In_{1.4}Sn_{0.3}Zn_{0.3}O_3$) thin films via solution combustion technique followed by performing their structural, electrical, compositional characterizations.

☞ To mimic the printing process using metallic ink – Balancing the capillary and Marangoni flows to achieve uniform deposit of silver-nano dispersion through the analysis of dwell-time.

☞ To understand the sintering kinetics of silver film deposited from the colloidal dispersion of the silver.

☞ To fabricate and characterize the film of high dielectric permittivity sodium β-alumina.

☞ To fabricate and characterize the TFTs using semiconducting IZTO ($In_4Sn_4ZnO_{15}$) and (a) conventional SiO_2 and (b) high permittivity sodium β-alumina dielectric.

CHAPTER 3

SOLUTION COMBUSTION PROCESSED TRANSPARENT AND CONDUCTIVE METAL OXIDE THIN FILMS
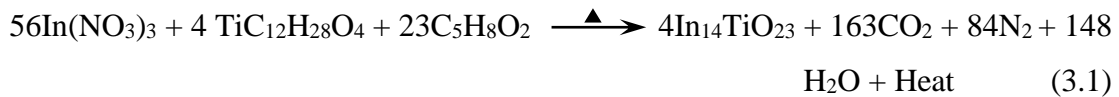
3.1 Introduction

Transparent and conductive metal oxides have proven their applicability in various electronic devices, including thin film transistors and solar cells; where, the unconventional combination of optical transparency and electrical conductivity is expected. The commercially available TCO is 10 wt. % tin doped In_2O_3, abbreviated as ITO. As mentioned in the previous chapter, the rare-earth indium, makes up 90 wt. % in commercial grade ITO contributes to the cost (Pasquarelli et al. 2011). Though the optical transparency and the electrical conductivity are two distinct class of properties, the inverse relation between them through carrier concentration imposes a severe limitation to the properties of TCOs (Calnan and Tiwari 2010). Thus, the realization of ultra-high transparency and the acceptable electrical conductivity needs a revisit to the design concept of TCOs (Facchetti and Marks 2010; Pasquarelli et al. 2011). The electrical conductivity in TCOs is mainly guided by the carrier concentration, due to the ease of formation of anion defects such as oxygen vacancies. Thus, suppressing oxygen vacancies and promoting high mobility of the carriers brings a new perspective to the high transparent TCOs. The TCOs, whose electrical conductivity is majorly driven by the mobility of the charge carriers are called mobility driven TCOs. Titanium-doped In_2O_3 (ITiO: $In_{14}TiO_{23}$) is one such TCO (Van Hest et al. 2005), where the high binding energy of titanium and oxygen suppresses the formation of oxygen vacancies.

In addition, the challenge of reducing rare-earth indium in commercial ITO is realized by adopting a co-doped system comprising of zinc and tin in In_2O_3 with the stoichiometry: $In_{1.4}Zn_{0.3}Sn_{0.3}O_3$-IZTO (Harvey et al. 2008b). The solubility of both zinc and tin in In_2O_3 is well below the limit (fig. 2.12). Apart from the design and selection concept of the TCOs, the deposition of the same becomes crucial in realizing the total cost. The large area deposition of commercial ITO adds-up to the total economic value,

due to the utilization of high-vacuum, capital-intensive deposition techniques (Kim et al. 2011b). The total cost of the TCO can be reduced by adopting solution processing techniques. A series of solution processing techniques have been reported in the literature. As an example: titanium doped In_2O_3 via spray pyrolysis at 400 ℃ has shown a transparency of 83 % and the electrical conductivity of the order $\sim 10^3$ S/cm (Parthiban et al. 2012). The existing literature is limited in the low-temperature solution processed ITiO thin films with transparency more than 90 %, similar to commercial ITO. In this regard, the solution combustion (Patil et al. 2008b), which utilizes redox chemistry of the precursor in realizing low-temperature fabrication can be employed in the fabrication of both ITiO and the IZTO. In this chapter, the low-temperature solution combustion processing of both mobility driven and carrier concentration (N) driven TCOs, namely ITiO ($In_{14}TiO_{23}$) and IZTO ($In_{1.4}Zn_{0.3}Sn_{0.3}O_3$) are addressed.
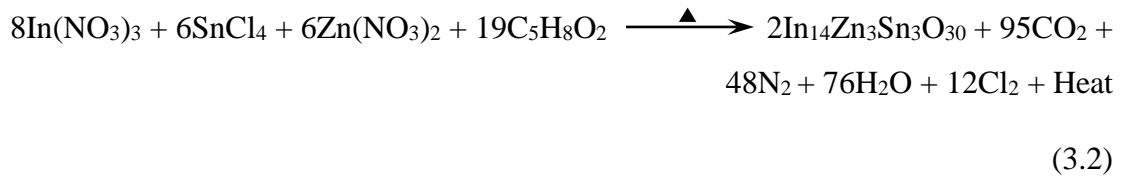
3.2 Experimental methods

To fabricate thin films of ITiO ($In_{14}TiO_{23}$), an initial precursor solution containing 1.5 g of indium nitrate ($In(NO_3)_3$, Sigma), 0.1 ml of titanium (IV) isopropoxide ($TiC_{12}H_{28}O_4$, Sigma) in 21 ml of 2-methoxyethanol (2-ME) was prepared and the amount of fuel – acetylacetone ($C_5H_8O_2$, Tarson Chemicals) was decided based on the balanced redox reaction (equation 3.1). The dried (80 ℃ for 8 h in vacuum oven) aliquots of the precursor solution were subjected to Thermogravimetric Analysis (TGA, PerkinElmer) and Differential Scanning Calorimetry (DSC, NETZSCH 404F1) with the heating rate of 10 ℃/min.

$$56In(NO_3)_3 + 4\ TiC_{12}H_{28}O_4 + 23C_5H_8O_2 \xrightarrow{\Delta} 4In_{14}TiO_{23} + 163CO_2 + 84N_2 + 148$$
$$H_2O + Heat \qquad (3.1)$$

The solution was then utilized for the fabrication of thin film using spin coating (3000 rpm for 30 s). The as-spun films were subjected to thermal annealing at four different temperatures, 300 °C, 350 °C, 400 °C and 450 °C. To understand the structural and compositional nature of the thin films, Grazing Incidence Angle X-ray Diffraction (GIAXRD, RIGAKU-Japan) and X-ray Photoelectron Spectroscopy (XPS, PH15000VersaProbeII) were carried out. The spectra of XPS were calibrated using carbon 1s (C 1s) and for the deconvolution of the spectrum, CASAXPS (version:

2.3.19PR1.0) software package was used. Further, optical, electrical, and topographical nature of the films were analyzed using UV-visible spectroscopy, Hall effect measurement system, and Atomic Force Microscopy (AFM, MMAFMLN-AM-1897) respectively.

Similarly, for IZTO ($In_{1.4}Zn_{0.3}Sn_{0.3}O_3$), a homogeneous and clear precursor solution comprising of 500 mg $In(NO_3)_3$ (Sigma), 92.7 mg of tin chloride ($SnCl_4$, Sigma), 67.4 mg of zinc nitrate ($Zn(NO_3)_2$, Tarson Chemicals) in 2-ME (Tarson Chemicals) was prepared. Addition of the fuel – $C_5H_8O_2$ (Tarson Chemicals) was designed based on fuel:oxidizer ratio (F:O). The optimum F:O of 0.5 was maintained as per the balanced redox stoichiometry (equation 3.2). In addition, two more precursor solutions were prepared with F:O = 5 and 0.05, as fuel rich and fuel lean mixtures, respectively. To understand the thermal behavior of precursor solutions, DSC was performed with the heating rate of 10 °C/min.

$$8In(NO_3)_3 + 6SnCl_4 + 6Zn(NO_3)_2 + 19C_5H_8O_2 \xrightarrow{\Delta} 2In_{14}Zn_3Sn_3O_{30} + 95CO_2 + 48N_2 + 76H_2O + 12Cl_2 + Heat$$

(3.2)

All three solutions were combusted on a hot plate and synthesized powders were subjected to calcination for 2 h at 600 °C. As-synthesized and combusted powders were subjected to x-ray diffraction (XRD, JEOL-JPX 8) using CuK_α radiation (wavelength: 1.5406 Å, scanning rate: 2 °/min, step size: 0.2) and transmission electron microscopic (TEM, accelerating voltage: 200 kV, JEM-2100, JEOL) studies. Further, thin films of IZTO were prepared using spin coating by utilizing the precursor solution with an optimum F:O (= 0.5) ratio. The as-spun films of IZTO were subjected to annealing at three different temperatures namely 200 °C, 300 °C, and 400 °C. To understand the structural nature, the deposited thin films were subjected to GIAXRD. Further, both optical and electrical properties of the thin films were analyzed using UV-visible spectroscopy and Hall effect measurements. In addition, the topographical nature of film was analyzed using AFM. To understand the surface chemical composition of the IZTO films, XPS studies were carried out and the obtained spectra were calibrated using C 1s (position: 284.6 eV). Further, inkjet printing (Micro-Fab Technologies Inc.)

of combustible precursors of IZTO was carried out. The surface profile (Dektak XT) of the printed line feature is recorded.

3.3 Results and Discussion

3.3.1 Solution combustion processed ITiO (In$_{14}$TiO$_{23}$)

It is important to know the temperature at which combustible precursor transforms into desired metal oxide. To accomplish the same, the DSC and TGA of the precursor was carried out. Fig. 3.1(a) shows, the TGA response of the precursor as a function of temperature. Two significant weight losses at 100 and 150 °C corresponds to evaporation of the solvent and the combustion reaction respectively. The evidence of combustion is supported by DSC thermogram, through an exothermic response at 150 °C (figure 3.1(b)). Thus, 150 °C is sufficient to transform the combustible precursor into the product, which is lower than the conventional sol-gel precursor (Kang et al. 2014). The unique advantage of the combustible precursor is that both the removal of gaseous impurities and the generation of heat (enthalpy) takes place at a fixed temperature (T_c, fig. 3.1(a)), which is 150 °C in the present case.
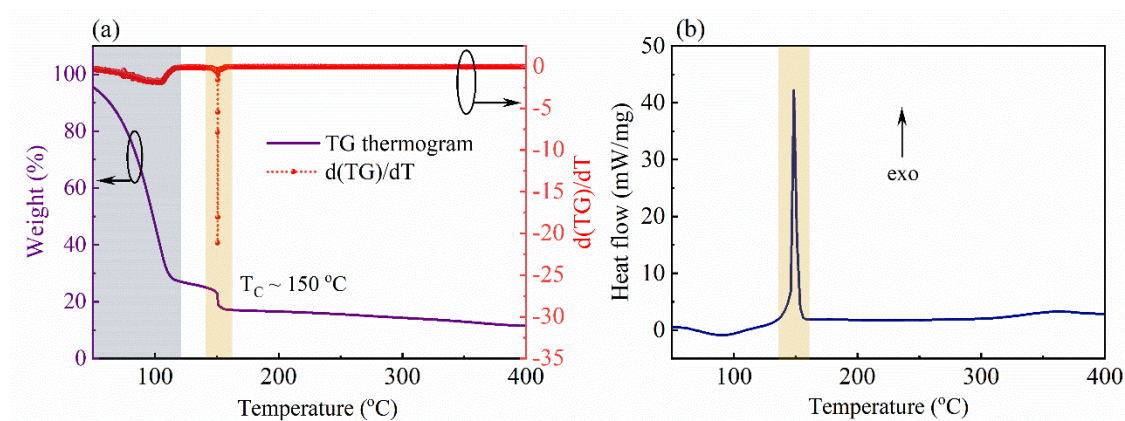

Figure 3.1 (a) TGA and (b) DSC thermograms of combustible precursor of ITiO.

It can be observed that the minimum temperature required for the initiation of the combustion reaction is 150 °C. The combustible precursor further adopted for the fabrication of thin films of ITiO on glass using spin coating. The as-spun films were annealed at four different temperatures namely 300, 350, 400 and 450 °C respectively. The films annealed at 300 °C is found to be amorphous (Gupta et al. 2008), but with

increase in the temperature of annealing the films start showing signs of crystallinity. With temperature, the films depict increased crystallinity without any secondary phases, confirmed by the GIAXRD studies (fig. 3.2(a)). In addition, the thicknesses of the films deposited are found to be decreasing with increasing temperature of annealing (300 °C: 212 ± 6 nm; 350 °C: 166 ± 8 nm; 400 °C: 134 ± 10 nm; 450 °C: 112 ± 6 nm), due to the removal of unburnt products of the combustion reaction. Thus, increasing crystallinity is supported by the purity makes high temperature annealed films to achieve a better optical and electrical properties.
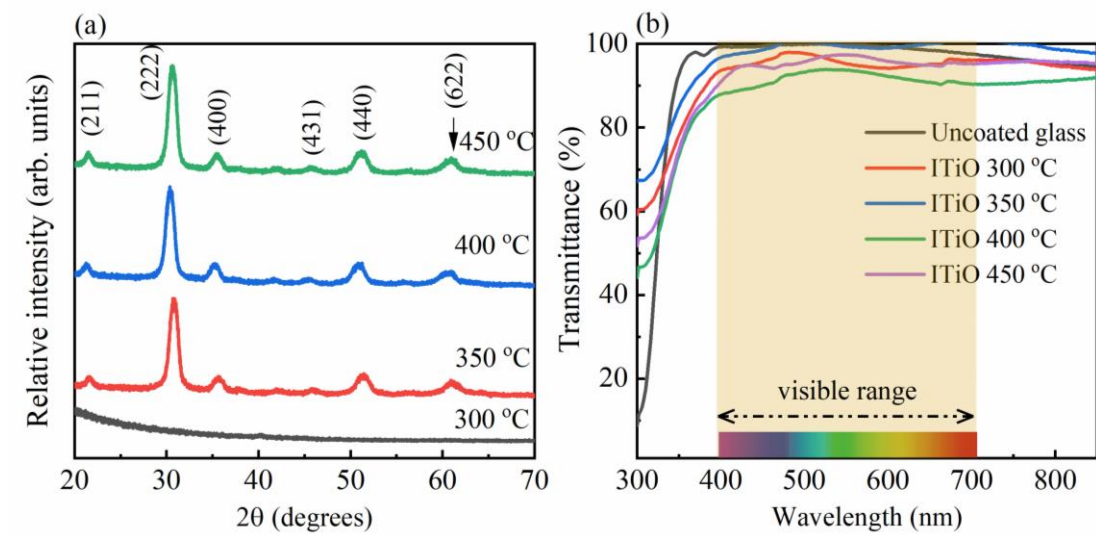

Figure 3.2 (a) GIAXRD and (b) UV-visible spectroscopic results of ITiO thin films.

UV-visible spectroscopic results (fig. 3.2(b)) depicts the optical properties of the films. The normalized transmittance plots (fig. 3.2(b)) revealed the high degree of transparency (> 93 %) in the visible region of the spectra for all films irrespective of temperature of annealing. In addition, the maximum transparency attained is nearly 100 % at 350 °C depicting the complete retainment of the transparency of uncoated glass. Thus, combustion processed films can achieve highest possible optical transparencies matching the bare or uncoated glass. Further, the transparency of the films by solution combustion is highest reported till date compared to the available literature of transparent conductors (fig. 3.3).

In addition, the film with maximum transparency is used for the determination of optical band gap using Tauc's plot and which is equal to 3.4 eV (fig. 3.4(a)). Further,

the fluctuations in the maximum transparency with the annealing temperature is supported by the Hall effect measurements (fig. 3.4(b)). The inverse dependency of electrical conductivity and the plasma wavelength is clearly depicted in the measurement of 'N'. The plots of maximum transparency and the 'N' are mirror images with respect to the XX axis (fig. 3.4(b)).
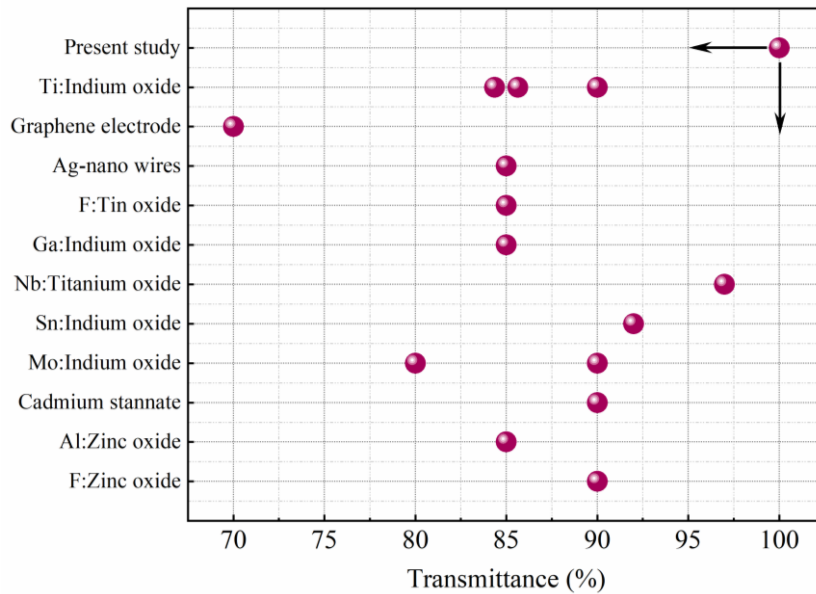

Fig. 3.3 A comparative study of transparencies of various TCOs and TCs.
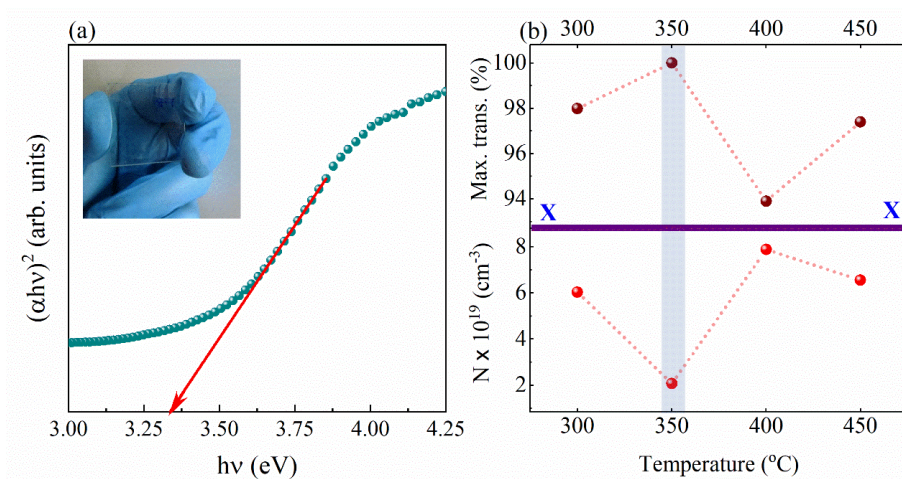

Fig. 3.4 (a) Optical band gap of ITiO (annealed at 350 °C) and (b) comparison between maximum transparency achieved vs carrier concentration (N).

Further, all ITiO films are smooth confirmed through AFM studies, which depicts a roughness ranging from 0.29 to 1.9 nm in all cases (fig. 3.5). The film having annealed

at 300 °C is smoother in nature due to its amorphous nature (fig. 3.2(a)) (Nomura et al. 2004). The increase in the roughness with the temperature of annealing is due to the enhanced crystallinity in the film. In addition, the topography of the film annealed at 450 °C shows a unique topography, the holes on the surface of film might be due to faster escape of gaseous impurities at high temperature (450 °C), contributing to the roughness (Carlos et al. 2016).

(a)
RMS: 0.29 nm
Thickness = 212 ± 6 nm
15.0 nm
0.5 µm
0.0   2.0 µm   0 nm

(b)
RMS: 0.36 nm
Thickness = 166 ± 8 nm
5.0 nm
0.5 µm
0.0   2.0 µm   0 nm

(c)
RMS: 1.2 nm
Thickness = 134 ± 10 nm
20.0 nm
0.5 µm
0.0   2.0 µm   0 nm

(d)
RMS: 1.9 nm
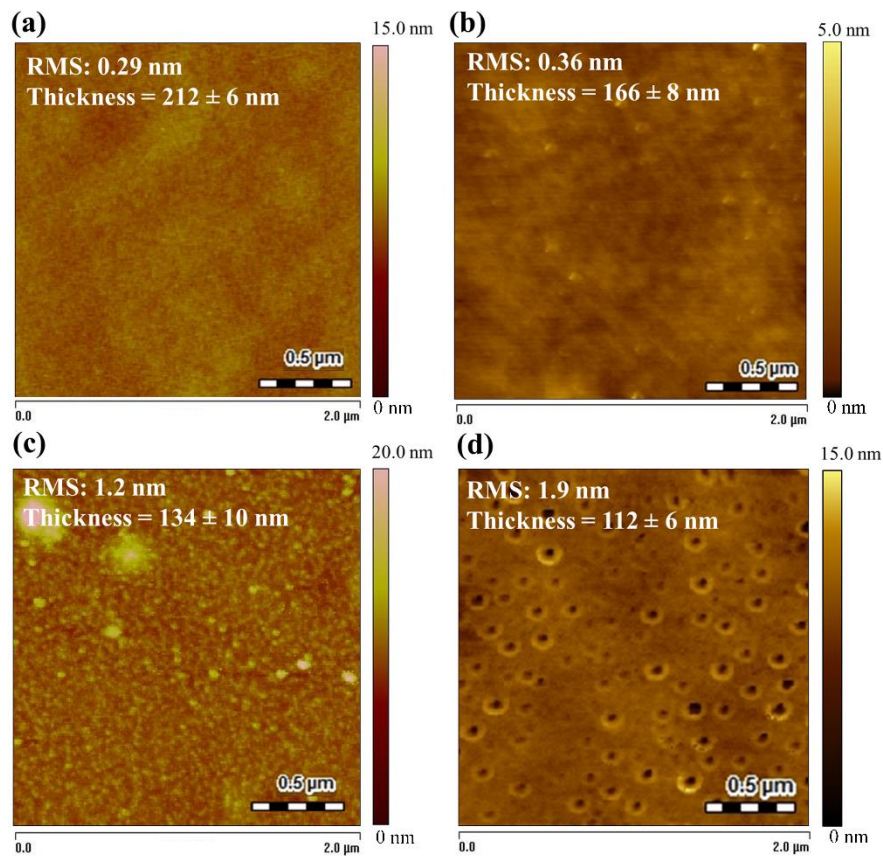Thickness = 112 ± 6 nm
15.0 nm
0.5 µm
0.0   2.0 µm   0 nm

Figure 3.5 Surface topography of ITiO films annealed at (a) 300 °C (b) 350 °C (c) 400 °C and (d) 450 °C. Thickness and roughness were measured using thickness profilometry and AFM respectively.

The electrical properties of the ITiO films annealed at different temperatures are estimated using Hall effect measurements. Both Hall mobility (μ_H) and electrical resistivity (ρ) are plotted against the temperature of annealing. The reduction in the ρ is due to the combined effect of μ_H and N (fig. 3.6).
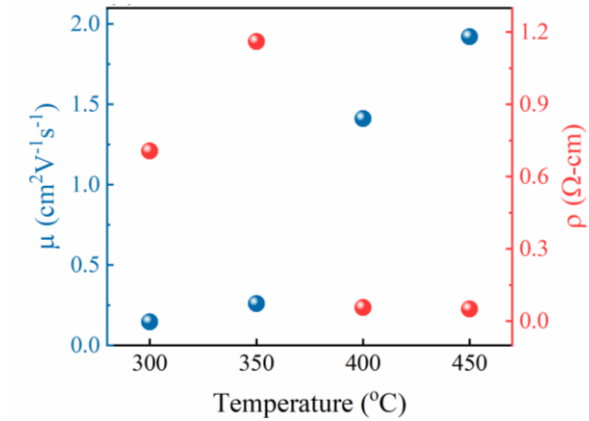
Fig. 3.6 Variation of μ and ρ as the function of annealing temperature.

The product of N, ρ and μ remained unaltered irrespective of annealing temperature ($N \cdot e \cdot \mu_H = e^{-1} = 6.22 \times 10^{18}$ (Coulombs)$^{-1}$) which clearly satisfied the equation 3.3.

$$\sigma = 1/\rho = N \cdot e \cdot \mu_H \tag{3.3}$$

The minimum ρ at 450 °C can be clearly attributed to highest μ_H and the order of the N (= 10^{19} cm^{-3}). The large variation in the μ_H and ρ as a function of annealing temperature can be attributed to chemical composition of ITiO films. XPS studies were carried out to understand the chemical nature of the surface of ITiO films. Fig. 3.7 shows the XPS survey spectrum of ITiO films annealed at different temperatures.
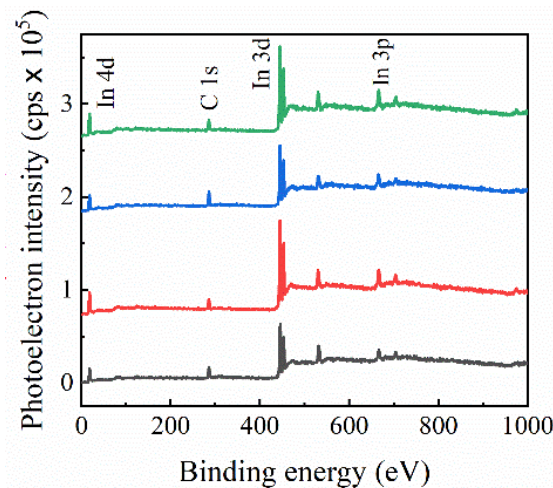

Fig. 3.7 XPS survey spectra of ITiO films annealed at different temperatures.

The presence of constituent elements – indium (In 3d$_{5/2}$ and In 3d$_{3/2}$, in the binding energy range 440 to 455 eV), titanium (Ti 2p in the binding energy range: 455 to 470

64

eV), carbon (C 1s, in the binding energy range: 283 eV to 287 eV) and nitrogen (N 1s, in the binding energy range: 390 to 410 eV) are confirmed through high resolution XPS spectra and presented the same in fig. 3.8(a-c) and fig. 3.9(a).

To get more insight, oxygen 1s (O 1s) responses were further deconvoluted into three distinct principal signatures centered at 529.5 ± 0.5 eV, 531.5 ± 0.5 eV and 530.5 ± 0.5 eV corresponding to lattice oxygen (M-O-M), and surface hydroxide species (M-OH) and O-adsorbates respectively (fig. 3.9(b-e)). The efficiency of the combustion reaction is described by a fraction (η), estimated from the relative areas under the deconvoluted peaks of O 1s spectra. The area fractions described as η^{M-O-M} (area of M-O-M peak / total area), η^{M-OH} (area of M-OH peak / total area) and $\eta^{O-adsorbates}$ (area of O-adsorbates peak / total area) are represented in fig. 3.9(f) as a function of temperature of annealing.
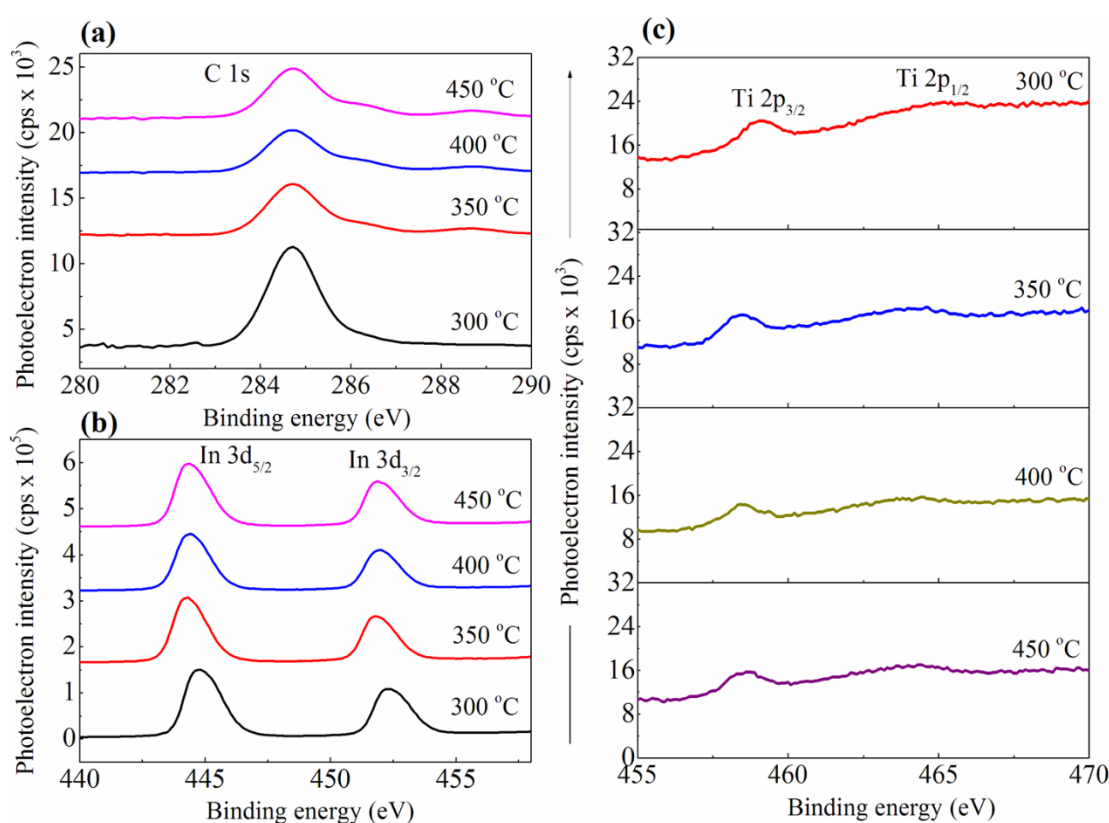

Fig. 3.8 High resolution XPS spectrum of (a) C 1s, (b) In 3d, and (c) Ti 2p of ITiO films annealed at different temperatures.

It can be clearly seen from fig. 3.9(f) that the relative fraction of lattice (η^{M-O-M}) increased from 300 ℃ to 350 ℃ depicting a maximum value of ~67 % added with a hydroxide contribution (η^{M-OH}) of only ~13 %. Hence maximum conversion of the precursor into metal oxide has taken place at 350 ℃. Further increase in temperature of annealing beyond 350 ℃, there is no significant variation in the η^{M-O-M} is observed. But, slight decay in the η^{M-O-M} post 350 ℃ is due to pronounced solvent evaporation at high temperature which hampered the kinetics of the chemical reaction, thereby decreased the precursor conversion efficiency (Branquinho et al. 2014).
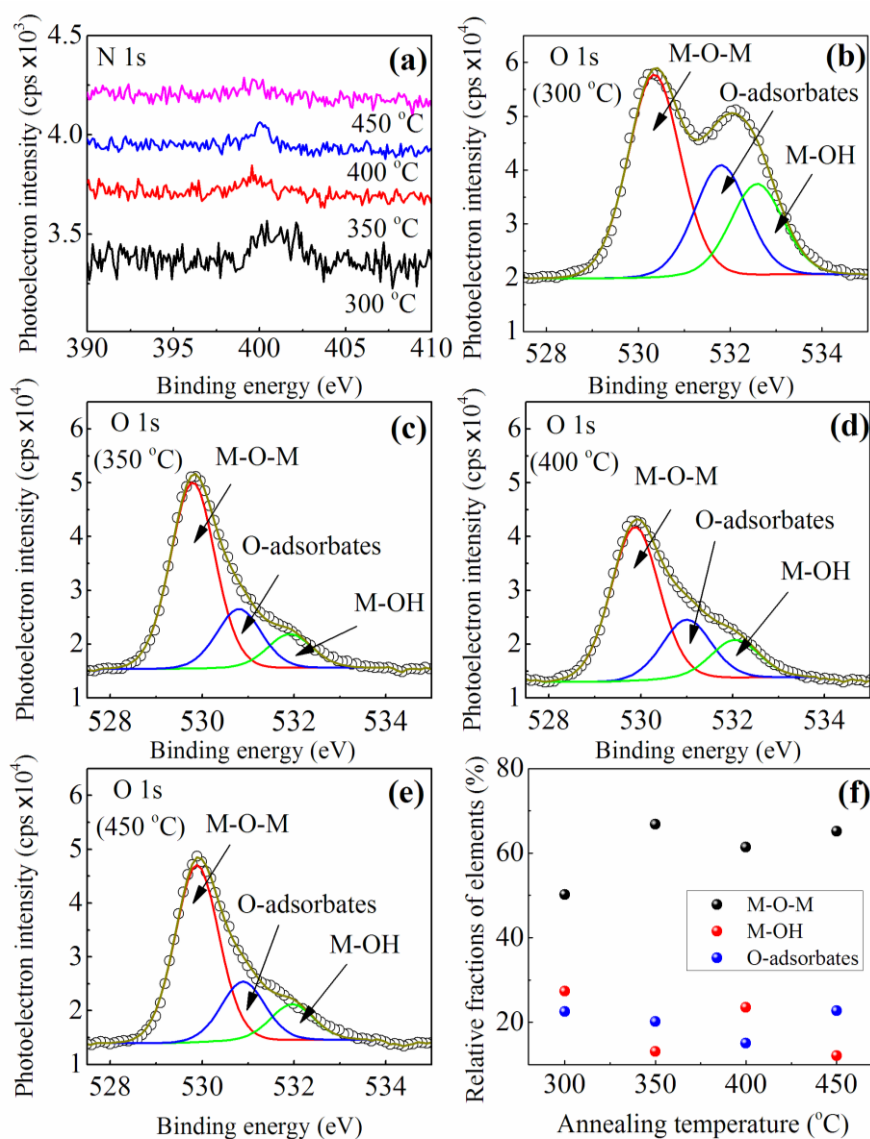

Fig. 3.9 High resolution XPS spectrum of (a) N 1s (b-e) O 1s peaks annealed at different temperatures (f) relative fractions of constituents.

AFM topographical results confirmed have also showed the pronounced evaporation of the solvent. Further commenting on $\eta^{\text{M-OH}}$, which is minimum at 450 °C with ~65 % $\eta^{\text{M-O-M}}$, slightly lower than the magnitude estimated at 350 °C. This is due to large fraction of $\eta^{\text{O-adsorbates}}$ at 450 °C (~23 %) that of 350 °C (~20 %). Due to high concentration of M-O-M the GIAXRD results (fig. 3.2(a)) showed pronounced crystallinity with temperature of annealing. In addition, ITiO being mobility driven TCO (Van Hest et al. 2005), thus with temperature having enhanced M-O-M, the mobility is expected to achieve higher magnitudes (fig. 3.12(a)). The highest $\eta^{\text{M-O-M}}$ (~67 %) at 350 °C depicts high percentage of In-Ti-O over detrimental M-OH and O-adsorbates, consequence of which the transparency of the film is high (nearly equals to uncoated glass). Thus, the combustion derived InTiO films are potential candidates for high transparent electrodes finds applications in various optoelectronic devices especially solar cells and TFTs.

3.3.2 Solution combustion processed IZTO (In$_{1.4}$Zn$_{0.3}$Sn$_{0.3}$O$_3$)

The stoichiometry (In$_{2-2x}$Zn$_x$Sn$_x$O$_3$; $x = 0.3$) adopted in the present study is within the solubility range of co-doping. The DSC thermogram of combustible precursors (fig. 3.10(a)) with different F:O ratios show endothermic responses at around 125 °C depicting the evaporation of the 2-ME.
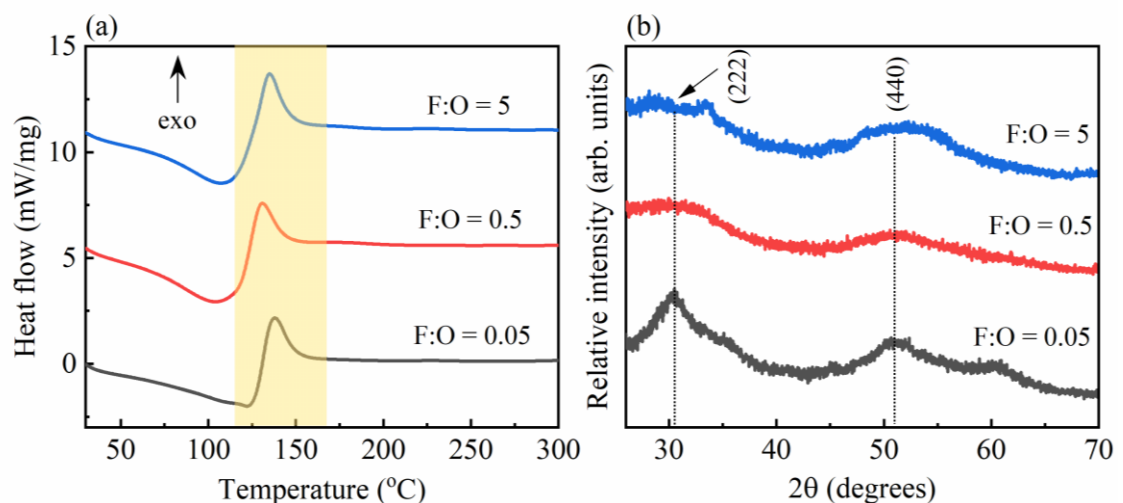

Fig. 3.10 (a) DSC thermogram of combustible precursors and (b) XRD pattern of as-combusted powders of IZTO with varying F:O ratio.

The exothermic peaks of DSC at 136.4 °C, 129.9 °C and 131.9 °C for F:O = 0.05, 0.5 and 5 respectively provides an evidence of combustion reaction. Minimum temperature of 129.9 °C is mandatory to initiate the reaction between the combustible elements with optimum F:O ratio (= 0.5). The solutions with different F:O are subjected to external heating to synthesize powders. Irrespective of F:O ratio all powders were found to be nearly amorphous, but shows the signs of crystallization (fig. 3.10(b)). Further, the nature of combustion found to be clean in the case of optimum F:O (= 0.5), the lean mixture shows sudden flaming and the rich mixture results in the voluminous combustion (fig. 3.11); the variants in the type of combustion depicts the relative amounts of fuel and oxidizers in the precursor.
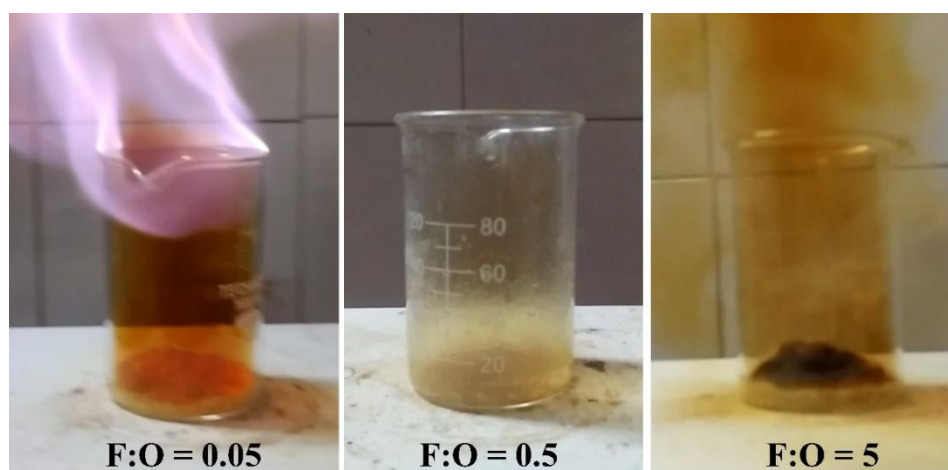

Fig. 3.11 Nature of combustion reaction of precursors having varied F:O ratios.

The colours of the powders synthesized are whitish, yellowish and black in the case of fuel lean, optimum, and rich mixtures respectively. The colour depicts the nature of the product.

To impart crystallinity, calcination of the as-synthesized powders was carried out. Calcined powders show high degree crystallinity confirmed through XRD (fig. 3.12(a)) and the relative positions of the indium, zin, tin, and oxygen are presented in the fig. 3.12(b), which is constructed using first principle density functional theory. The low combustion temperature added with clean burning nature of the precursor having an optimum F:O (= 0.5) adopted for the fabrication of thin films onto a glass substrate. The as-spun films were annealed at three different temperatures namely, 200 ℃, 300

℃ and 400 ℃. The films found to be crystalline even at 200 °C and crystallinity pronounces with temperature of annealing (fig. 3.13(a)).
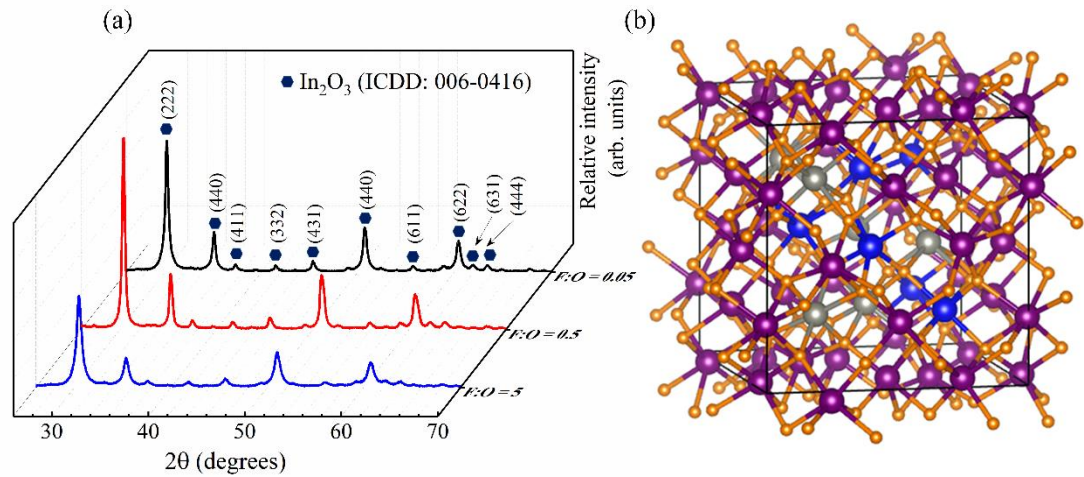

Fig. 3.12 (a) XRD pattern of calcined IZTO powders and (b) unit cell of IZTO constructed using first principles density functional theory.
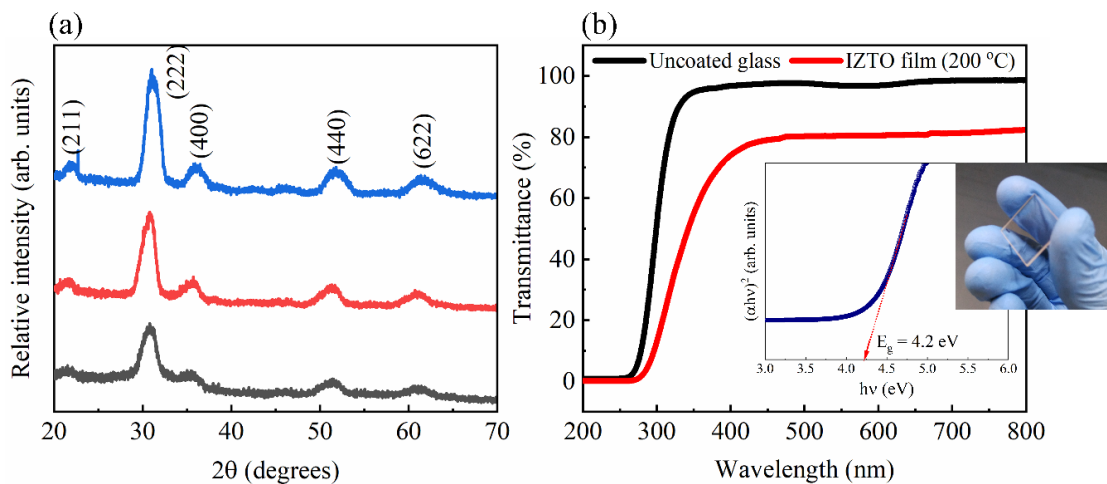
Fig. 3.13 (a) GIAXRD pattern of thin films of IZTO and (b) UV-visible spectroscopic results along with optical band gap of IZTO film annealed at 200 °C.

These results are contradictory to the bulk counterparts of IZTO synthesized at same temperature. The variation in characteristics of IZTO systems is mainly due to the decomposition pathways of combustible precursors (Cochran et al. 2017). Thus, the combustion reaction in a nanometre thick film doesn't resemble the thermal behaviour depicted by DSC study (Sanchez-Rodriguez et al. 2013). Further, the film annealed at

200 ℃ depicts a considerable degree of transparency (~83 %) in the visible spectra (fig. 3.13(b)) with an optical band gap of 4.2 eV (fig. 3.13(b), inset) calculated from Tau's plot (equation 3.4)

$$\alpha h\nu = \alpha_o(h\nu - E_g)^{1/2}, \tag{3.4}$$

where α, E_g, $h\nu$, and α_o are absorption coefficient, band gap, photon energy and a constant respectively. The topographical nature of the IZTO films is presented in figure 3.14. Irrespective of the temperature of annealing, the thin films of IZTO are smooth with smaller RMS roughness magnitudes.
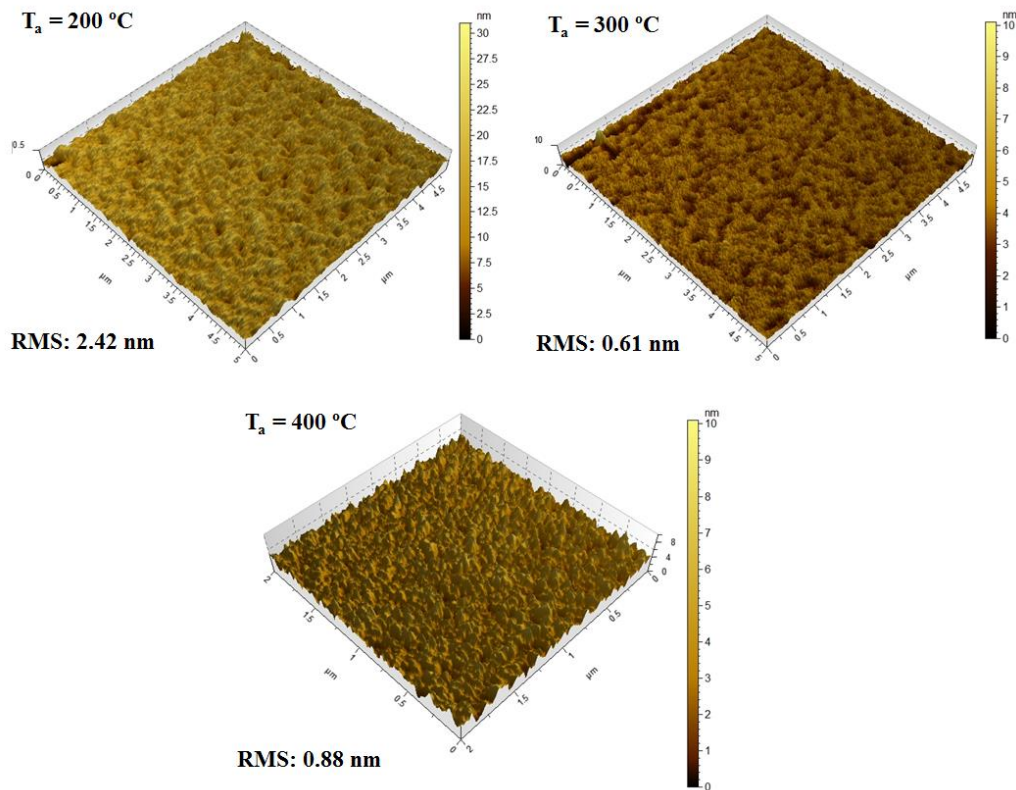
Fig. 3.14 Surface topography of IZTO thin films annealed at different temperatures.

Further, to understand the electronic properties IZTO thin films, Hall effect measurements were carried out and found that type and the order of carrier concentration (N) were n-type and $\sim 10^{19}$ cm^{-3} respectively (fig. 3.15(a)). Due to formation of oxygen vacancies, the magnitude of 'N' shoots up from 3.7 to 6.7 (figure 3.5(a)). In addition, the 'μ_H' shows an increasing trend with the temperature of annealing (fig. 3.15(b)) due to high concentration of carriers and the ease of movement

of charges. The net effect of both 'N' and 'μ_H' resulted in the decrement in the electrical resistivity (ρ) (fig. 3.15(c)). The order of ρ (10^{-2} Ω-cm) at 200 ℃ is lower than solution combustion processed commercial grade ITO thin film. Further, the first principle DFT calculation show minimum effective band gap of 0.9 eV, is responsible for the electrical conductivity (fig. 3.15(d)).
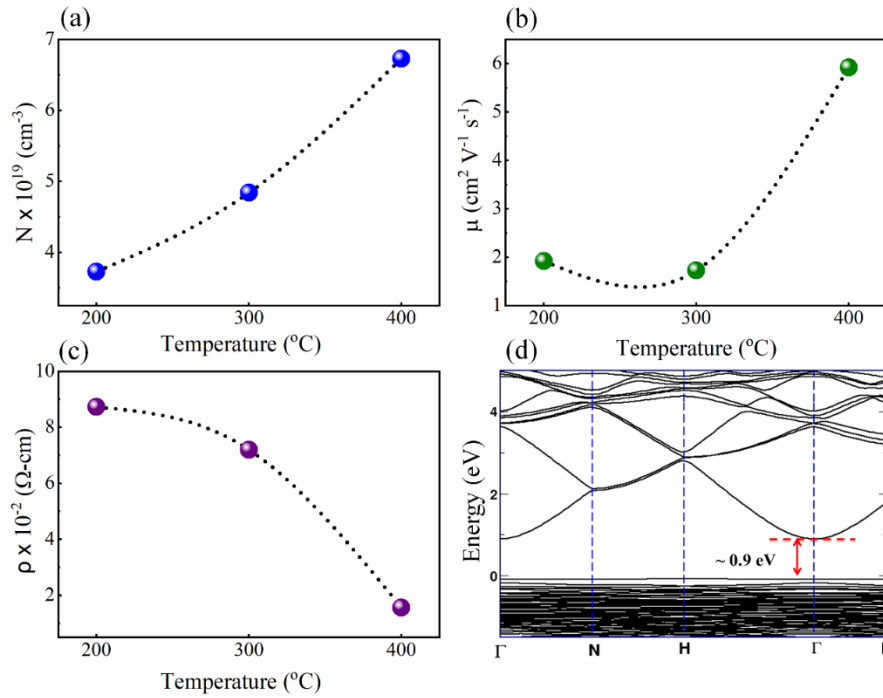

Fig. 3.15 Hall effect measurements of IZTO films: (a) carrier concentration, (b) Hall mobility, (c) electrical resistivity of IZTO films annealed at different temperatures and (d) electronic band structure of IZTO.

To understand the chemical composition of the surface of the IZTO film, XPS studies were carried out. The survey scan confirms the presence of indium, zinc, tin, oxygen and carbon. The constituents were found to be in the ratio In:Zn:Sn::14:3:3 (fig. 3.16(a)). Further, fig. 3.16 (b-d) shows the deconvoluted O 1s peaks of the surface of the IZTO films annealed at 200, 300 and 400 ℃ respectively. The principal signatures peaks at 529 $\pm$ 0.5 eV corresponding to M-O-M lattice (Hennek et al. 2013), 531.5 $\pm$ 0.5 eV accounting surface metal hydroxide species (M-OH) (Hennek et al. 2013), 530 $\pm$ 0.5 eV corresponding to O-adsorbates (Faber et al. 2014) and additional synthetic

peak of nitrate impurities (at 533.7 eV) (Jeong et al. 2011) in the film annealed at 200 ℃ is observed (fig. 3.16(b)).

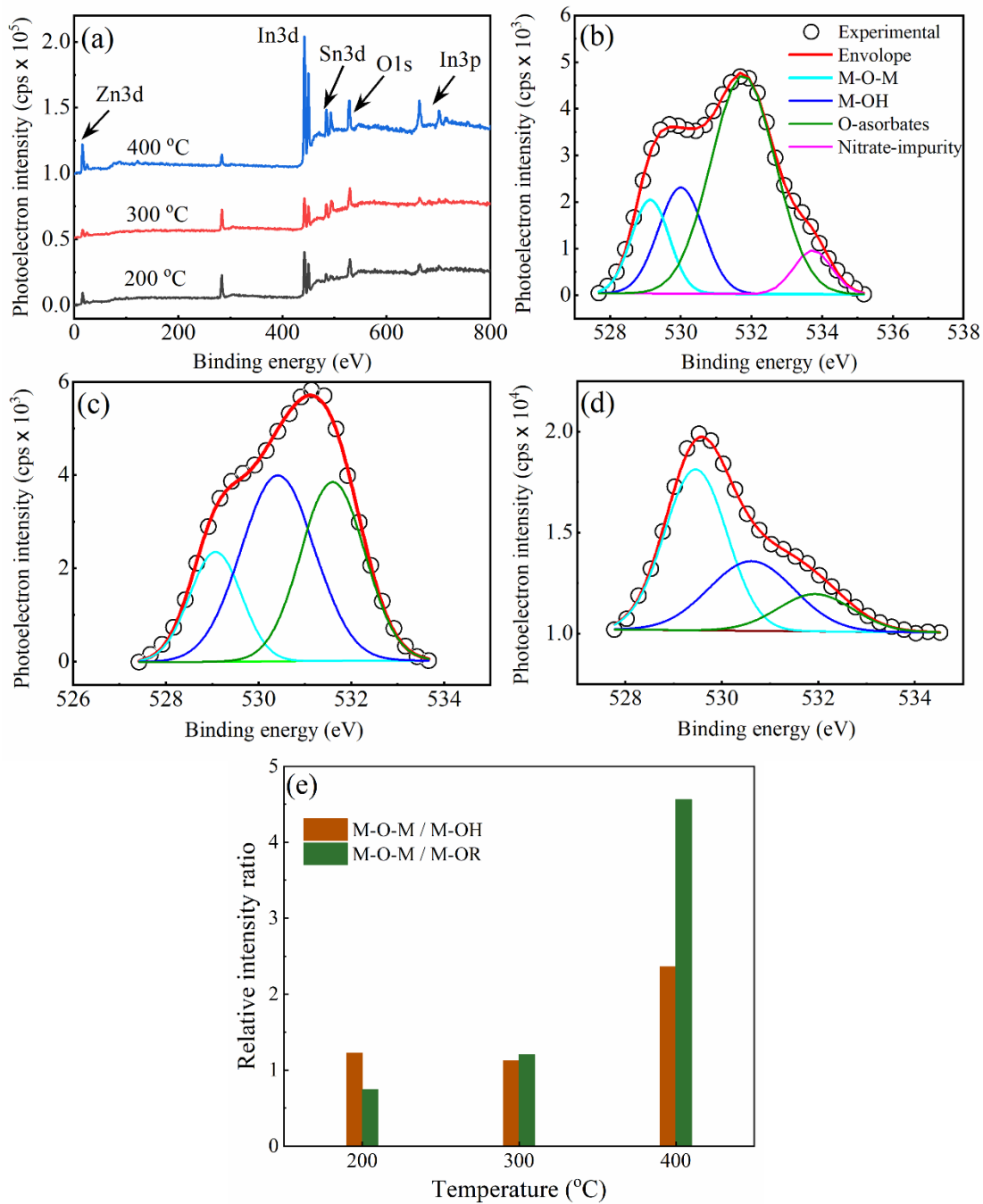Fig. 3.16 (a) XPS survey scans, deconvolution of O 1s peaks of IZTO films annealed at (b) 200 °C (c) 300 °C(d) 400 °C and (e) intensity ratios depicting the formation of M-O-M as a function of temperature of annealing.

The Gaussian synthetic peaks of all signatures of O 1s compared with respect to their photoelectron intensities. The ratio of M-O-M / M-OH and M-O-M / O-adsorbates are plotted (fig. 3.16(e)). It is found that the formation of M-O-M is less pronounced at 200 °C, but increases with increase in the temperature of annealing. These results can be supported by the GIAXRD patterns of IZTO thin films (fig. 3.13(a)). The high temperature pronounced crystallinity in the films is due to increased concentration of lattice oxygen (M-O-M). The results are also reflected in the electrical and optical characteristics. Due to high percentage of M-O-M in films annealed at 400 °C both 'ρ' and 'μ$_H$' turn out to be maximum compared to the films annealed at 200 °C. Further, when it comes to completely transparent optoelectronic devices such as TFTs, till date the most of the research work is concentrated on the usage of metallic electrodes as contacts. Since the metallic patches are opaque in nature restricts the overall transparency of the devices. In recent years, sol-gel derived cadmium oxide along with aluminium doped cadmium oxide are inkjet-printed to show the efficacy of molecular precursors based on 2-ME and water and concluded that at low temperature 2-ME solvent based solutions result in coffee ring deposits (Deegan et al. 1997). Whereas, in this study 2-ME based IZTO combustible precursor presents no such effect (fig. 3.17(a-b)).
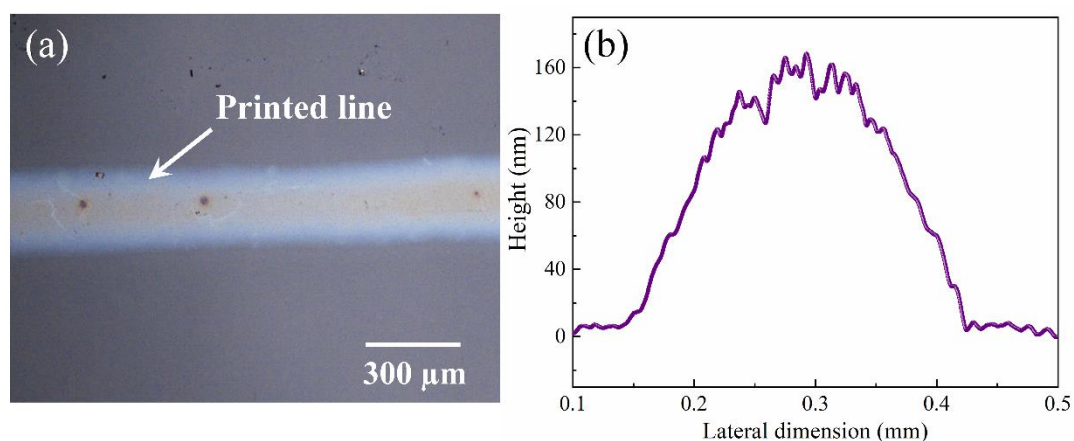

Figure 3.17 (a) optical micrograph and (b) thickness profilometry of printed IZTO line.

It can be attributed to the presence of two distinct organic compounds (2-ME-solvent and acetylacetone-fuel) with different surface tension and with the pre-annealing temperature of 200 ℃, which helps in imparting sufficient gradients of surface tension

resulting in Marangoni flow. Thus, the dome shaped cross section of printed IZTO line is possible to achieve with 2-ME solvent based IZTO precursors.

3.4 Conclusions

From the study, it is clear that the molecular combustible precursor yields continuous, uniform and the high-quality thin films of ITiO and IZTO at low-processing temperatures. The fabricated thin films are conducting and transparent in nature. The ITiO films have shown highest optical transparency (~100 %) ever reported due to high efficiency of the combustion reaction, performed at 350 ℃. The co-doped system of zinc and tin in In_2O_3 have shown acceptable combination of optical transparency (~ 83 %) and the electrical resistivity (10^{-2} Ω-cm) at 200 ℃. In addition, the inkjet printed IZTO line feature has shown a dome shaped profile with nullified morphological irregularities such as coffee ring and center dot.

CHAPTER 4

CHALLENGES OF NANO DISPERSION AND POSSIBLE SOLUTION

4.1 Introduction

In this chapter the morphological challenges in depositing uniform film of silver is addressed by a method called 'dwell-time' modulation. The nano-dispersion of the silver particles is called 'ink', used for the inkjet printing while fabricating the electrodes of various optoelectronic devices. The printable ink constitutes solvent(s) and the surfactant (dispersant/capping agent), which helps in achieving stable colloidal solution. The printable conducting inks are available commercially. Fig. 4.1, is the schematic representation of the constituents of the ink. Post printing of the inks followed by the thermal annealing at a temperature greater than the maximum decomposition temperature of constituents results in the retained stains of silver (Kamyshny et al. 2005). Thus, the selection of constituents of the ink, plays a vital role in deciding the quality of the deposit.

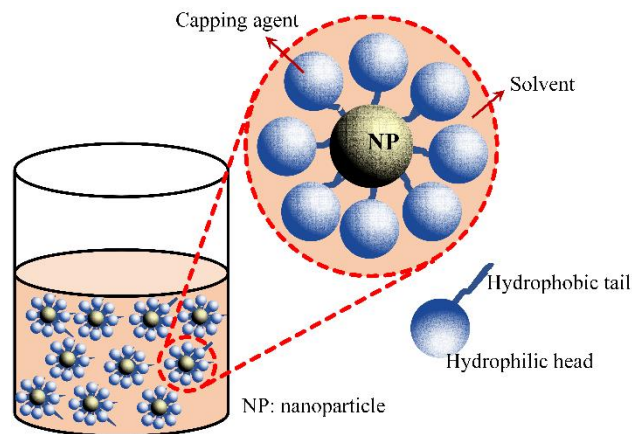Fig. 4.1 Schematic representation of constituents of ink

The morphology of the deposited silver film is guided by the evaporation of the solvent. During the time span of evaporation, the movement of the solvent molecules which carry the silver nanoparticles decides the end morphology. The deposited drop of the ink with non-zero contact angle evaporates at the pinned three-phase contact line and

evaporates faster at the pinned edges compared to center of the drop. The localized evaporative flux results in the larger loss of the solvent at the pinned edges (Deegan et al. 1997). The mass loss is balanced by the replenishment of the solvent from the center of the drop; the fluid from the center to the edge, brings nanoparticles to the edge thereby promoting the peripheral deposition, which results in the ring formation. The ring stains are popularly known as coffee rings (Deegan et al. 1997). Further, if sufficient surface tension gradient is generated then the resulting Marangoni flux reverses the ring formation leading to the center deposit (Hu and Larson 2006). Thus, two distinct flows namely, capillary and Marangoni gives rise to ring and center deposits respectively. Both morphological disorders hamper the flow of charge carriers, thus needs to be prevented for the better performance of the devices. As deposited films are assemblage of nanoparticles, which are physically in contact and needs thermal annealing to make it free from the non-conducting organic constituents such as dispersants. Thus, the as-deposited film of silver needs to be treated thermally. Under the supplied heat energy, the ligands of the surfactants first undergo deboning followed by decomposition. Post debonding, the silver nanoparticles come together and form a continuous path via sintering (Gupta et al. 2012). Thus, sintering of the particles post or during debonding plays a crucial role in establishing the percolation path for the charge carriers.

In the case of nanoparticle dispersions (or the inks), there are series of unavoidable events that need to be fulfilled, such as (a) synthesis of nano particles, (b) selection of solvent and surfactant/dispersant, (c) deposition: overcoming the morphological extremities, (c) elimination of non-conducting constituents, and (d) sintering (Pasquarelli et al. 2011). These steps become irrelevant if the molecular precursors are employed in place of nano-dispersions. In the present chapter, a simplest way called 'modulation of dwell-time' is employed to achieve uniform deposit of silver from nano-dispersion followed by the sintering kinetics. Technically, 'dwell-time' can be defined as the time elapse between the drop casting and the annealing. The modulation of dwell-time will severely affect the evaporative kinetics and alter the morphology. At last, similar deposit of the silver is studied through molecular combustible precursors of silver.

4.2 Experimental methods

4.2.1 Dwell-time modulation and sintering kinetics

Polyol derived silver nano-dispersion (Manjunath et al. 2018) was used to study the effect of modulated dwell-time. For the analysis, drop casting (single drop, volume: ~20 µl) of the silver nano-dispersion was used. Constant drop volume was maintained throughout the study. Range of annealing temperatures (120, 150, 180, 200 and 250 °C) with three different dwell-times (10, 20 and 30 min) were adopted. In order to understand the effects of dwell-time, three different sets of experiments were designed. In the first set, concept of 'infinite dwell-time' was explored. The drop of the silver dispersion on a glass substrate was allowed to evaporate completely under ambient temperature and pressure. Further, the 'zero dwell-time' was analysed by impacting drop of silver nano-dispersion onto a preheated glass substrate maintained at different temperatures. The final analysis was dedicated to the 'variable dwell-time,' where the drop of the silver nano-dispersion onto the substrate is allowed to evaporate naturally for three different time spans (10, 20 and 30 min.) and subsequently the semi-evaporated drop allowed to lose the remaining solvent under the supplied heat. Finally, the solvent free silver stains were annealed for 30 min. to make the samples free from surfactants and to promote sintering. The quality of the sintered silver drop was analysed using profilometry (Dektak XT, Bruker) and optical microscopy (Olympus BX53-F, PerkinElmer). To understand the grain sizes and their distribution, Scanning Electron Microscopy (SEM, model JSM 6380, JEOL) and ImageJ software were used. The obtained average grain sizes were used for the calculation of grain volume and a sintering model comprising of sintering time and temperature was adopted for the calculation of grain growth parameter (K). The predicted mathematical model was validated with experimental grain sizes.

4.2.2 Solution combustion processed films of metallic – silver

2 g of silver nitrate ($AgNO_3$, Sigma) and 0.75 g of citric acid ($C_6H_8O_7$, Tarson Chemicals) were dissolved in 10 ml of water to form a combustible precursor, as per the equation 4.1 (Salian et al. 2019).

$$6AgNO_3 + 2C_6H_8O_7 \xrightarrow{\quad\blacktriangle\quad} 6Ag_{(s)} + 3N_{2(g)} + 8H_2O_{(g)} + 12CO_{2(g)} + Heat$$

(4.1)
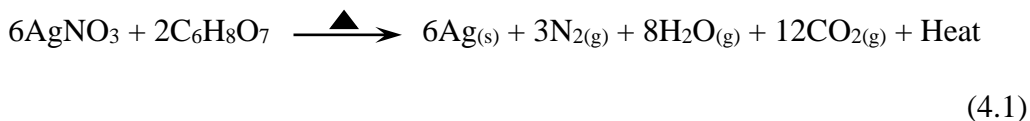
DSC of dried aliquots of the precursor was carried out to understand the thermal behavior. The precursor solution was then spray coated on to the preheated glass substrate. The spray coating parameters are (a) distance between the nozzle and the substrate: 12 to 13 cm, (b) gas used: inert nitrogen, (c) time of spray: 30 s, (d) time for intermediate annealing: 15 min and (e) number of sprays: 10. The resulting film was subjected to GIAXRD and the Transmission Electron Microscopic (TEM, JEOL) analysis to understand the nature of the silver film. Finally, the electrical conductivity measurements were carried out using four probe system.

4.3 Results and Discussion

As defined previously, the 'dwell-time' is the time-elapse between the subsequent events of drop casting and the thermal annealing, which is guided by the evaporation of the solvent. Thus, the dwell-time is highest in the case of natural evaporation of the drop because of elaborated time taken by the solvent at room temperature and pressure. In the case of forced evaporation, the sudden impact of the drop onto the preheated substrate results in the spontaneous elimination of the solvent. Thus, the dwell-time is least or negligible. On the other hand, dwell-time extremities (zero-forced evaporation and infinite-natural evaporation) greatly affects the morphology of the deposit. It is essential to note that the dwell-time is dependent on the type of solvent, ambience of processing, and the temperature of annealing. Thus, it can be attributed as the one of the characteristics of the ink. Thus, the tuning of the dwell-time (10, 20 and 30 min.) directly affects the end morphology of the deposit. In the forthcoming sections the effect of modulated dwell-time is discussed.

4.3.1 Infinite dwell-time

For the broader inclusion of different class of inks with different chemistry, the prefix 'infinite' is used. Natural evaporation took extended time, in the present case the polyol derived silver ink consumed a time of 40 min. Since the drop is allowed to undergo natural evaporation, thus the temperature induced Marangoni flows are

negligible. Fig. 4.2(a) and 4.2(b) shows the results of profilometry along with the optical micrographs of the deposits, at 200 and 250 °C respectively. Due to the existence of extreme capillary outward flows during the evaporation resulted in the pronounced edge deposit. To quantify the percentage of edge deposit, a geometric model comprising of two edge triangles along and rectangle is considered as shown in the fig. 4.3.
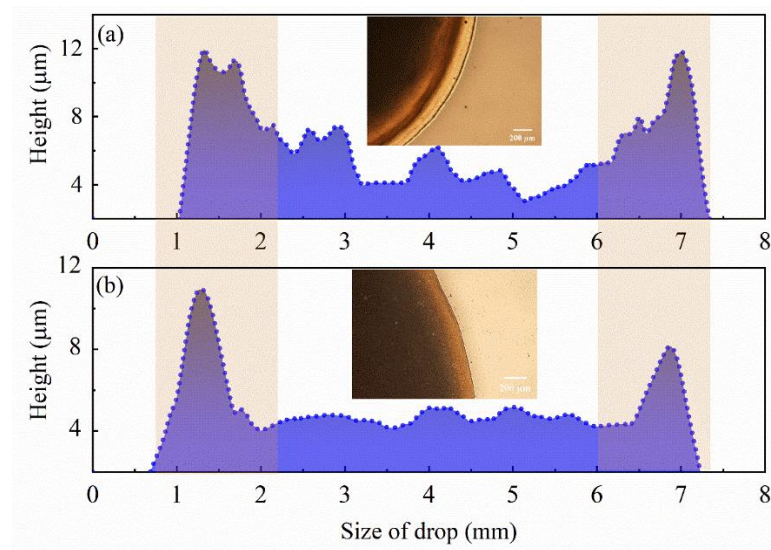

Fig. 4.2 Profile and optical micrograph of the deposited silver with a dwell-time of 40 min with an annealing temperature of (a) 200 and (b) 250 °C.
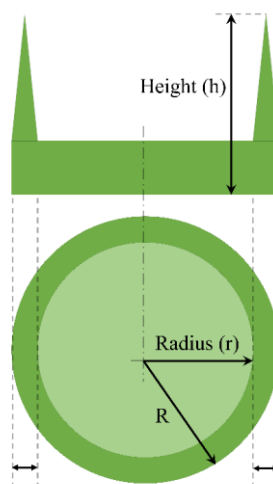

Fig. 4.3 Geometric model of the edge deposit

The total volume of the deposit is equated to the area of the deposit times the height. Further, the total fraction of the edge-deposit is calculated using a simple fraction technique. It is found that 95 % and 98 % of the silver is deposited at the edge of the stain for the temperatures 200 °C and 250 °C, respectively. The high percentage of edge deposit is the resultant of dominating capillary flow over Marangoni flow.

4.3.1.1 Natural evaporation and annealing at 200 ºC

Volume of the deposit = area × average height of the deposit

$$= [(\pi / 4) \times (6.3 \text{ mm})^2] \times 6 \times 10^{-3} \text{ mm}$$

$$= 0.1870 \text{ mm}^3$$

Volume of edge deposit = area of the ring stain × height of the ring stain

$$= [(\pi / 4) \times (1 \text{ mm})^2] \times 12 \times 10^{-3} \text{ mm}$$

$$= 9.4274 \times 10^{-3} \text{ mm}^3$$

Percentage of edge deposit = $[\{(0.1870) - (9.4274 \times 10^{-3})\}/(0.1870)] \times 100$ **~ 95%**

4.3.1.2 Natural evaporation and annealing at 250 ºC

Volume of the deposit = area × average height of the deposit

$$= [(\pi / 4) \times (6.52 \text{ mm})^2] \times 8.007 \times 10^{-3} \text{ mm}$$

$$= 0.2679 \text{ mm}^3$$

Volume of edge deposit = area of the ring stain × height of the ring stain

$$= [(\pi / 4) \times (0.73 \text{ mm})^2] \times 0.4185 \times 10^{-3} \text{ mm}$$

$$= 4.1853 \times 10^{-3} \text{ mm}^3$$

Percentage of edge deposit = $[\{(0.2679)-(4.1853 \times 10^{-3})\}/(0.\ 0.2679)] \times 100$ **~ 98%**

4.3.2 Zero dwell-time

Furthermore, if the drop is impacted onto the preheated glass substrate, then the resulting silver stain shows totally adverse deposit due to non-negligible Marangoni

flows, which carries the silver particles back to the center of the drop from the edges. The temperature gradients on the surface of the drop results in the localized variation of the surface tension of the solvent. The flow backed by the gradient in surface tension is called Marangoni flow. The flow of solvent carries the passive silver nanoparticles from the localized areas of low surface tension to high surface tension. Thus, the extreme Marangoni flow results in the complete adverse effect. Fig. 4.4(a) and 4.4(b) depicts the profilometric results of the deposits resulted from the sudden impacted silver nano dispersion. It is visualized from the plots that the peripheral deposit of the silver is minimum, but the center deposit is maximum irrespective of annealing temperature. The y-axis of the plot depicts the height of the deposit, where the magnitude is with the stain annealed at 250 ℃, this may be due to the increased annealing temperature thereby the improved Marangoni flux.
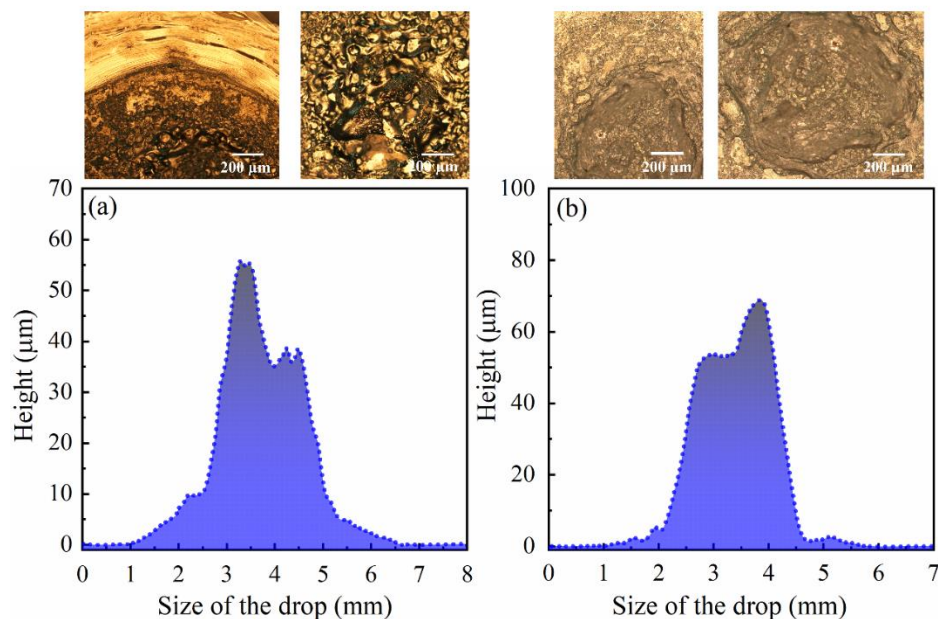
Fig. 4.4 Profile and optical micrograph of the deposited silver with a negligible dwell-time at an annealing temperature of (a) 200 and (b) 250 °C.

4.3.3 Modulated dwell-time

Further, in the case of the combined natural and force evaporation, interestingly the morphology of the silver deposit tends towards uniform distribution. In other words, outcome of systemic amalgamation of the results presented in fig. 4.2 and 4.4 gives rise

to the elimination of the both the extremities. The silver particles act as flow tracers carried by fluid particles gets frozen, when the fluid leaves the system (the drop of nano-dispersion of silver). when the fluid escapes from the drop, the particles of silver begin to sinter with neighbouring silver nanoparticles due to supplied thermal energy, to reduce the overall surface energy. If the drop is allowed to undergo natural evaporation for a particular span of time, then the silver nanoparticles start depositing at the periphery, once the drop is transformed to a hot plate maintained at prescribed temperature of 200 or 250 ℃, the remaining fluid starts evaporating under the supplied thermal energy. By the action of this, the silver nanoparticles start depositing at the center. Thus, the proper tuning of dwell-time between natural and forced evaporations, a uniform deposit of the silver throughout the radius of the stain can be achieved in the drop cast. In the present study, the profilometer results along with the optical micrographs have been presented in fig. 4.5 (a-f) and 4.6 (a-f) for the temperatures 200 and 250 ℃, respectively. The dome shaped features depict the uniform distribution of silver over the radius of the drop after the evaporation of the solvent (fig. 4.5(a-c) and 4.6 (a-c)) and the top view of the silver deposits, shown in the optical micrograph conveys the surface uniformity of the deposits (fig. 4.5(d-f) and 4.6 (d-f)).
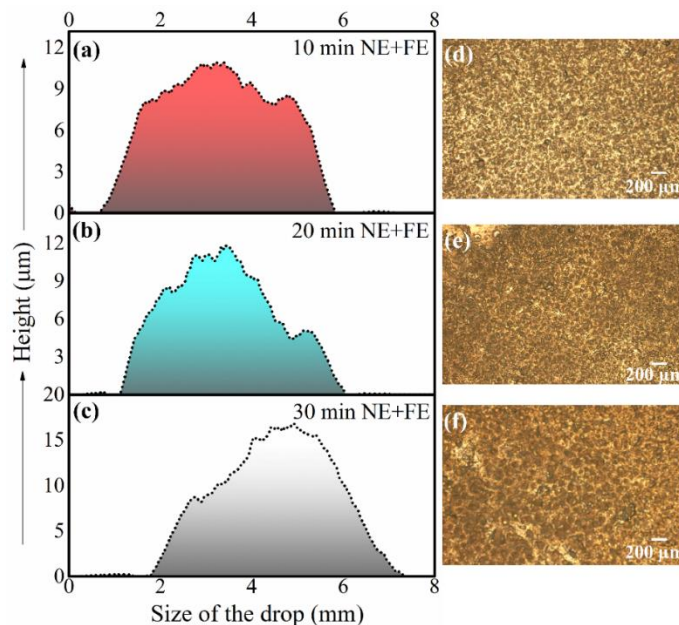

Fig. 4.5 Profilometer and optical micrographs of combined effect of natural and forced evaporations at 200 ℃ with modulated dwell-times.

The nature of deposits of silver with combined natural-forced evaporation at 200 ℃ (fig. 4.5) and 250 ℃ (fig. 4.6), shows nearly uniform deposits at different dwell-times, but at higher annealing temperature the deposit is slightly dominated with the center deposit. The reason may be due to pronounced Marangoni flux backed by the higher annealing temperature. The deposit at 200 ℃ with 10 min dwell-time is perfectly dome shaped profile signifying a uniform distribution of the mass of the silver over the entire radius of the stain. The uniform deposit is due to combined effect of both natural and forced evaporations with a dwell-time of 10 min. The dwell-time may vary with the chemistry of the nano-dispersion and the annealing temperature. Thus, it is important to include dwell-time as a new property of the nano dispersion. Manufacturers generally include properties such as viscosity, surface tension, electrical conductivity, and the annealing temperature; this study proposes a new property called dwell-time which is mandatory in achieving a uniform deposit.
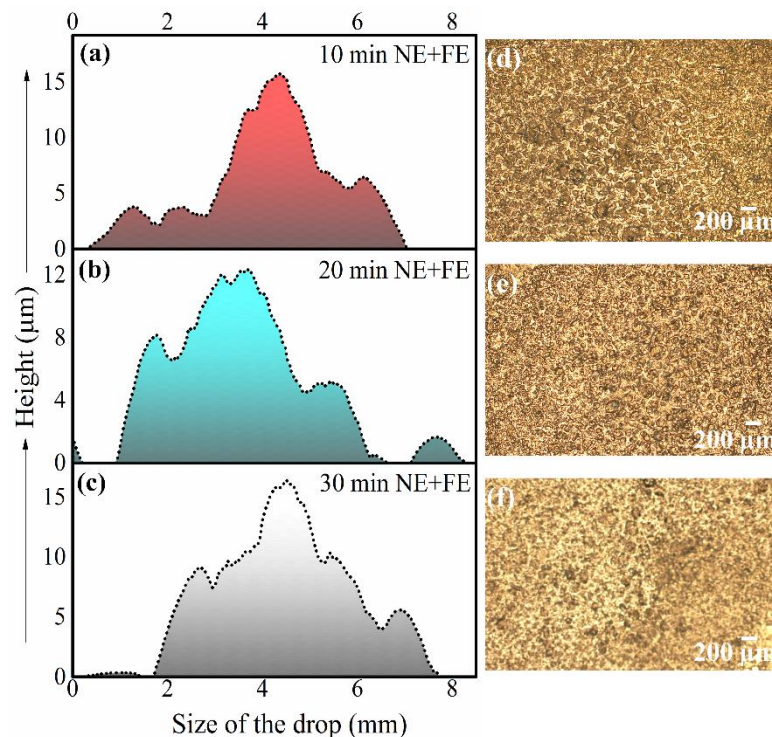

Fig. 4.6 Profilometer and optical micrographs of combined effect of natural and forced evaporations at 250 ℃ with modulated dwell-times.

4.3.4 Mechanism

Overcoming two morphological extremities result in the uniform deposit. Fig. 4.7(a) ad 4.7(b) shows the schematic of three kinds of morphologies. The underlying mechanism is the "distribution of mass." The total mass of silver nanoparticles is constant per drop of the nano-dispersion, but the distribution of which is guided by the evaporation of the solvent. In the case of pure natural evaporation, the maximum mass of the deposits at the periphery. Similarly, in the case of forced evaporation, the maximum mass of silver accumulates at the center of the deposit. With modulated dwell-time, the results clearly state the uniform deposition of the silver. The above study is applicable to 200 and 250 °C and extended to a range of annealing temperatures.
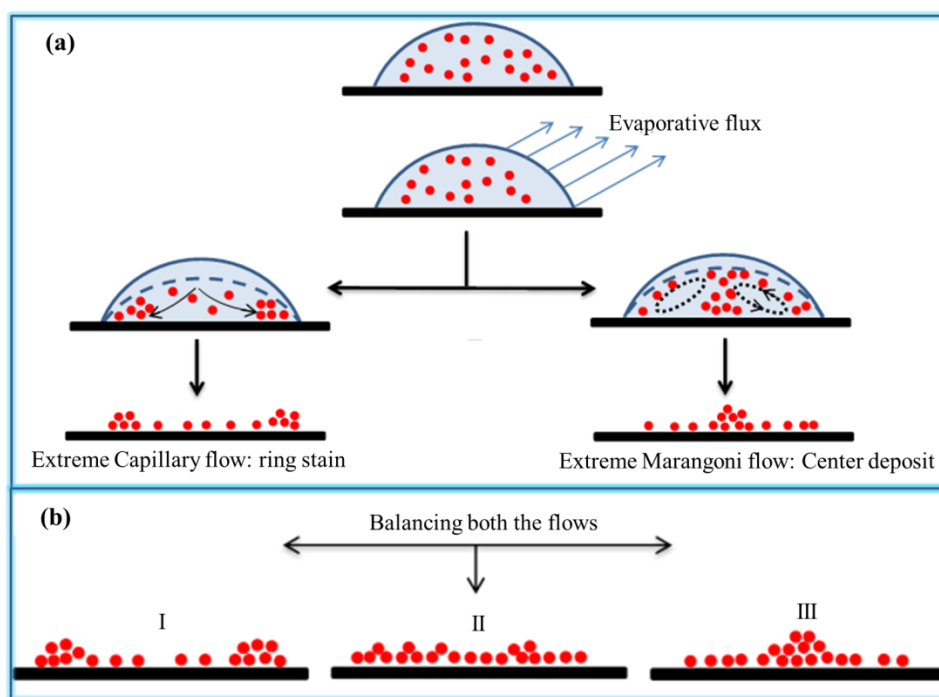
Fig. 4.7 Schematic depicting three distinct morphologies

Thus, similar investigations are performed for various temperatures of annealing and the zone of uniform deposit, edge and center deposits are plotted on a temperature vs. dwell-time plot as presented in the fig. 4.8. The left vertical axis is termed as the 'dot dominance line' depicting 'zero dwell-time' and the right vertical ordinate shows 'ring dominance line' showing 'infinite dwell-time' (40 min for the present polyol derived

silver nano dispersion). Also, the transition zone represents the transition between two morphologies, whereas the zone of uniform deposit appears with a combination of temperature and dwell-times for which the present polyol derived silver nano-dispersion results in the uniform film.

4.3.5 Sintering kinetics

After the complete evaporation of the solvent a micrometre thick silver deposit undergoes subsequent step of (i) debonding of the capping agent/surfactant and (ii) the sintering. The sintering is affected by mobility of the grain boundary, which is influenced by segregation of the impurities such as capping agents.
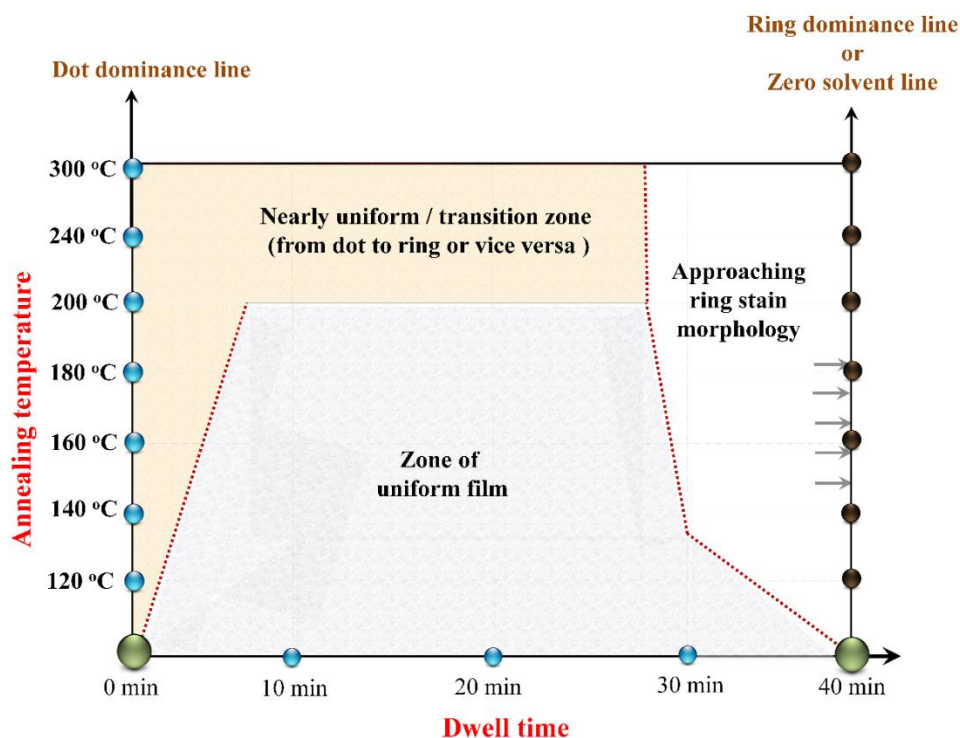
Fig. 4.8 Zone map showing the formation of ring stain, center and uniform deposits from silver nano dispersion.

Thus, the sintering initiates soon after the process of debonding of the capping agents or simultaneously. A schematic presented in the fig. 4.9 covey the stages of removal of segregated impurities and facilitating the exchange of atoms between the particles through diffusion resulting in sintered product. Initially debonding of

surfactants relieve them from the surface of silver nanoparticles and allows the nanoparticles to come closer by increasing the physical contact (fig. 4.9). But, retainment of surfactant does exist over a range of temperature hindering the growth of grains by the movement of atoms across the boundaries (fig. 4.9). In the schematic, the red line between two silver nanoparticles shows the hindrance to the process of sintering followed by the process of grain growth. Continuing, the linear law governing the increment of the volume of the grain at a temperature for a range of annealing times is presented in the equation 4.2. The parameters involved are, grain size after the annealing (G), annealing time (t), and initial grain size (G_o).
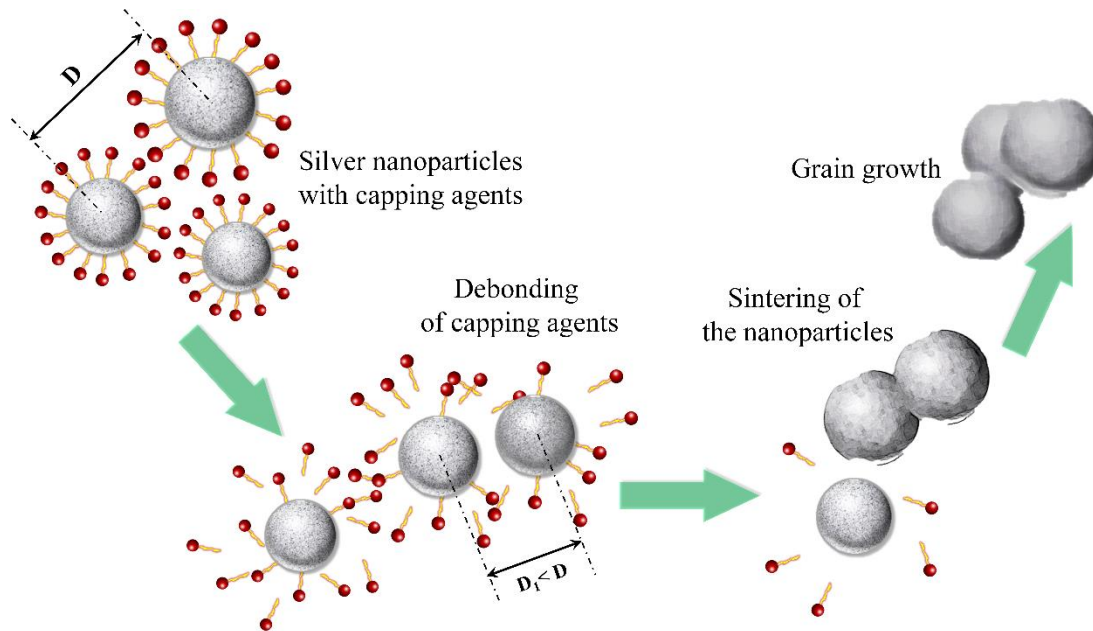
Fig. 4.9 Stages of removal of impurities from the surface of the nanoparticles facilitating the process of sintering

Importantly, K which is the rate constant (also termed as the grain growth parameter), is a complex function of activation energy, diffusion rates, fractional porosity, etc.

$$G^3 = G_o^3 + Kt \qquad (4.2)$$

the deciding factors of the grain size are concise in the grain growth parameter. The, K is the sum of two product functions (equation 4.3)

$$K = K_{SS}C_{SS} + K_{SV}(1 - C_{SS}) \qquad (4.3)$$

where, K_{SS} is the grain growth parameter accounts to the solid-solid interface (grain-grain interface), C_{SS} is the fraction of the solid-solid interface. Similarly, the term K_{SV} accounts for the growth of solid-vapor interface (grain communicating with the pore) and the term C_{SV} depicts the fraction of solid-vapor interface. Practically, the magnitude of K_{SV} is equated to zero, due to the lack of solid solubility in vapor. Thus, K is dependent to both K_{SS} and C_{SS} only (equation 4.4).

$$K = K_{SS}C_{SS} \tag{4.4}$$

Further, the magnitude of C_{SS} depends on the fractional porosity. Since C_{SS} is defined as the fraction of solid-solid interface; the remaining fraction is porous structure, as depicted in the equation 4.5.

$$C_{SS} = 1 - q\sqrt{\varepsilon} \tag{4.5}$$

where, q is a constant and from the equations 4.4 and 4.5;

$$K = K_{SS}(1 - q\sqrt{\varepsilon}). \tag{4.6}$$

The rate of increase of grain size can be calculated by differentiating the equation 4.2. Thus, the differential form of the equation 4.2 along with the equation 4.6, the rate of change of grain size is presented as:

$$\frac{dG}{dt} = \frac{K_{SS}(1 - q\sqrt{\varepsilon})}{3G^2}. \tag{4.7}$$

Further, to determine the arithmetic change in the grain size (from G_1 to G_2) as a function of annealing time (t = t_1 to t_2), the equation 4.7 can be integrated within the limits (equation 4.8)

$$\int_{G_1}^{G_2} 3G^2 dG = \int_{t_1}^{t_2}\{K_{SS}(1 - q\sqrt{\varepsilon})\}dt \tag{4.8}$$

the final form is written as:

$$G_2 = \sqrt[3]{G_1^3 + \{K_{SS}(1 - q\sqrt{\varepsilon})\}\Delta t_{1-2}} \tag{4.9}$$

for initial grain size of G_o at t = 0, the equation 4.9 can be rewritten as:

$$G = \sqrt[3]{G_0^3 + \{K_{SS}(1 - q\sqrt{\varepsilon})\}t} \,. \tag{4.10}$$

An estimation of grain size is performed using above equations. The predicted grain sizes then compared with the experimental results. Fig. 4.10 and 4.11, shows experimental values of grain sizes at different annealing times and temperatures; with increase in annealing temperature and time, the grain sizes increase. Also, due to an abnormal grain growth, a wide distribution of grain sizes is observed at high temperature of 250 °C and an annealing time of 20 and 25 min.
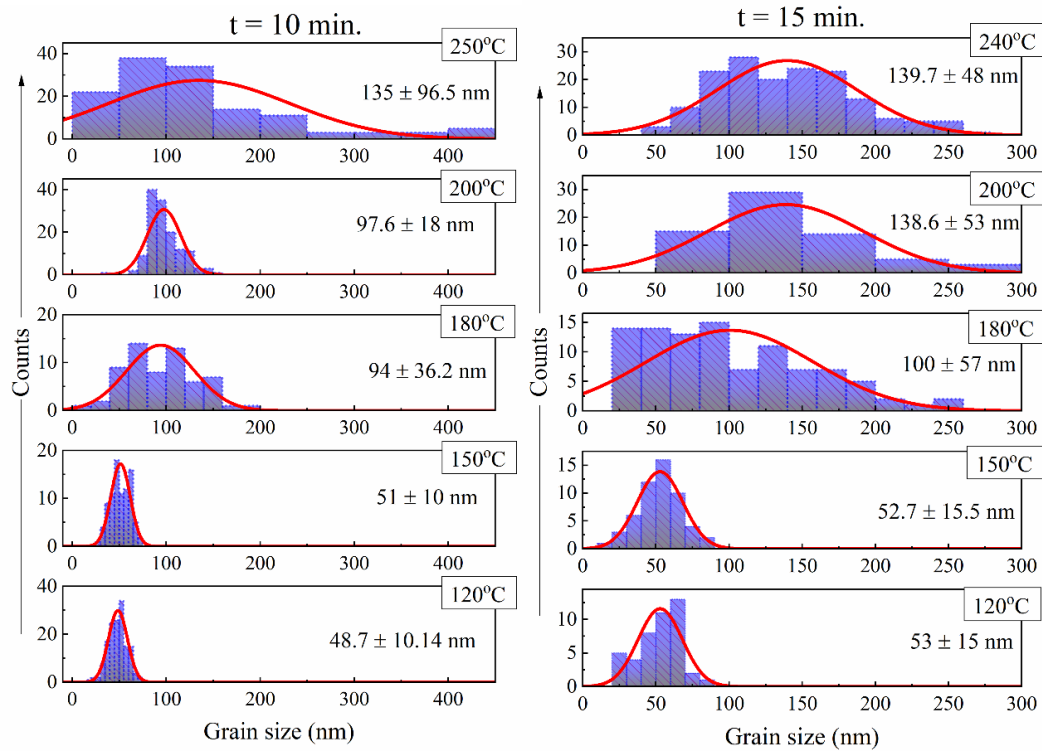
Fig. 4.10 Grain size distributions at different temperatures at 10 and 15 min.

Further, the rate determining parameter in the equation of grain growth is 'K', which is a composite function involving many aspects of growth kinetics. The determination of K plays a vital role in the prediction of the final grain size. By mathematical fitting of the isothermal sintering model at various annealing temperatures, the magnitude of K is estimated. The linear law involving grain volumes (equation 4.2) is then rewritten as a function of annealing temperatures. Fig. 4.12 shows the comparison of the mathematically estimated grain sizes with the experimental outcomes. In powder

metallurgy, an initial green compact is sintered to densify. But, in the present case, the initial system comprising self-aligned nanoparticles, which are brought together by the evaporation of the solvent.
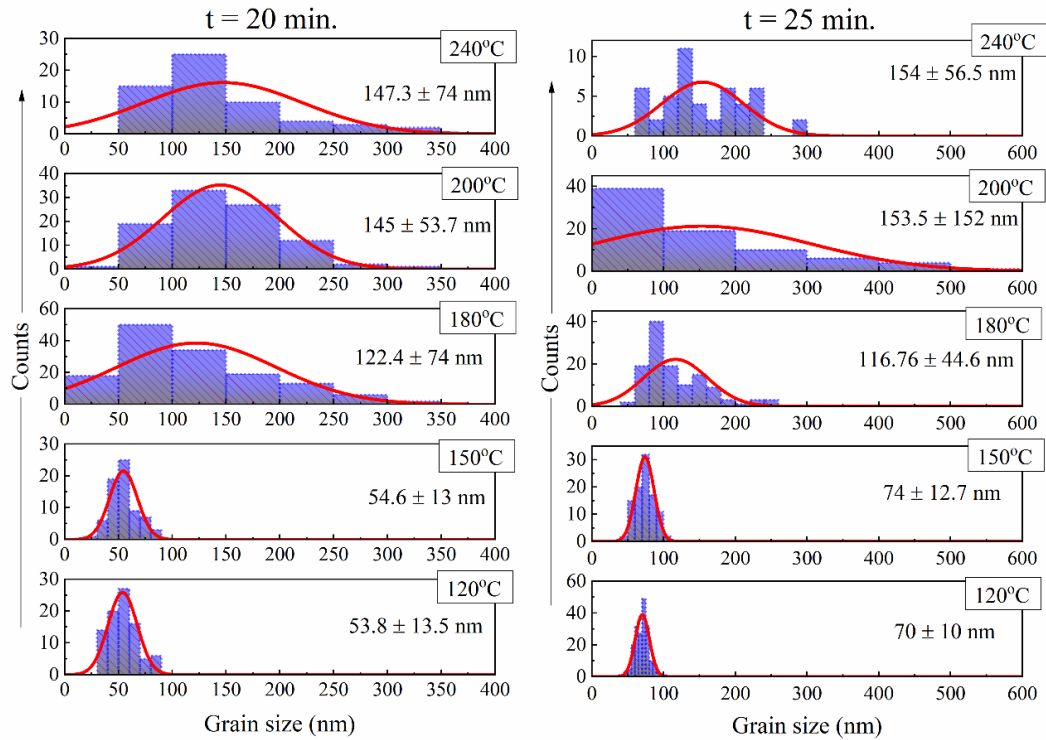
Fig. 4.11 Grain size distributions at different temperatures at 20 and 25 min.

In all the cases irrespective of temperature of annealing, experimentally estimated grain sizes obey the theoretically predicted ones with minute deviations. Especially, the data presented for annealing time of 25 min., deviated substantially from the theoretically predicted grain sizes (fig. 4.12(a) and 4.12(b)) due to abnormal grain growth. The predicted grain sizes nearly match the experimented ones at temperatures 180 and 200 ℃ (fig. 4.12(c-d)). Further, annealing at 250 ℃ also promotes the abnormal growth independent of annealing time (fig. 4.12(e)). In addition, a considerable deviation at low temperature of annealing could be due to the presence of surfactants, which does affect the rate grain growth.

Further K, which is the composite function of diffusion rates, activation energy, fractional porosity etc., is determined for all temperatures and presented as a function of temperature of annealing (fig. 4.12(f)); the magnitude of K increases with

temperature of annealing. The variation of K is due to the increase in the value of C_{SS} with the temperature of annealing. Due to increase in the temperature the fractional porosity decreases due to growth of solid-solid interface (grain boundary). Since, diffusion is a thermally activated phenomena, which promotes the growth of solid-solid interface at the cost of solid-vapor interface, as a result the K is accounted solely to increase in K_{SS}. Thus, the increase in both K_{SS} and C_{SS} results in the increase of K. Further, the value of K can be attributed to the percolation path of the deposited film.
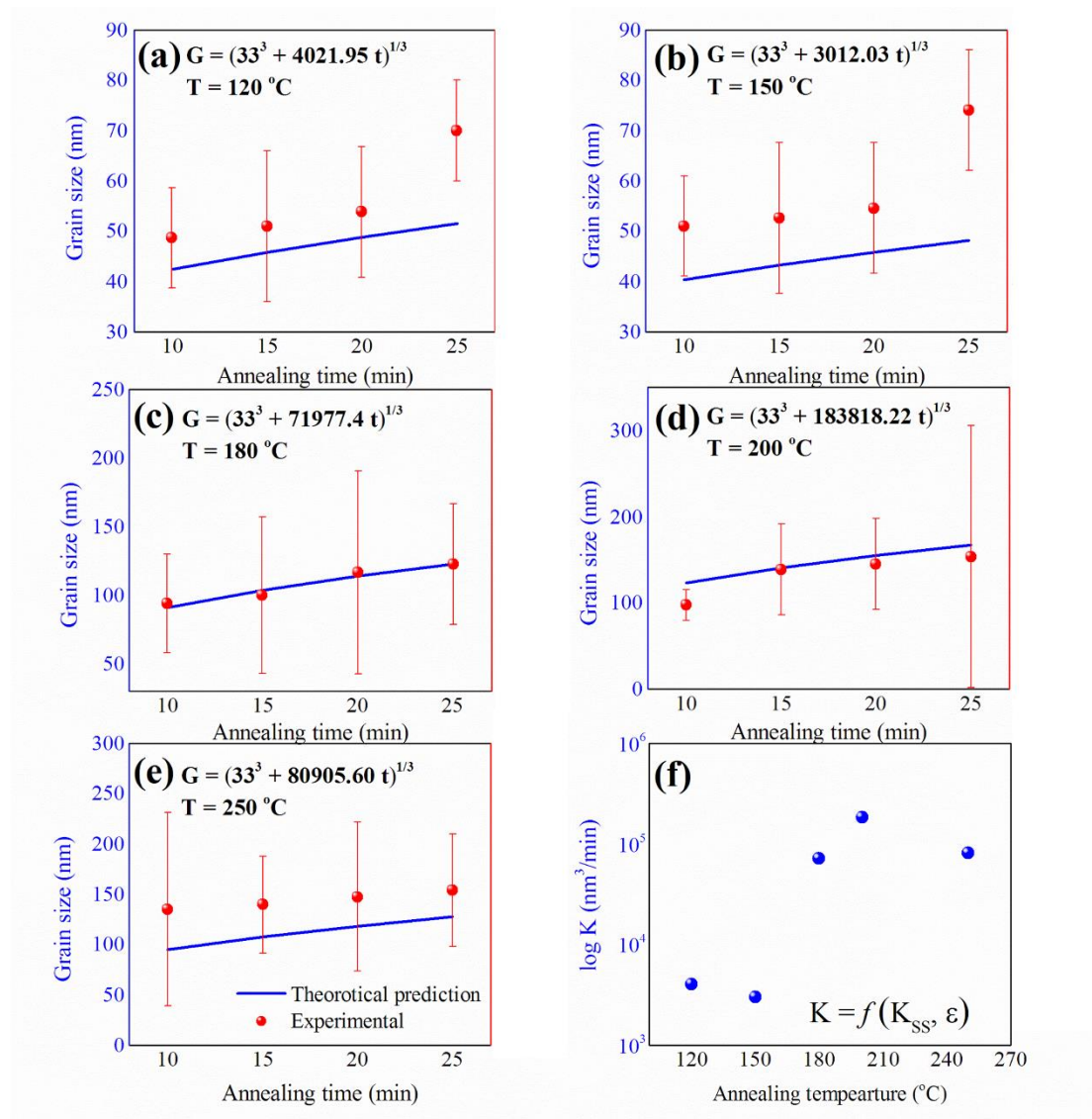

Fig. 4.12 A comparison of both experimentally estimated and the theoretically predicted grain sizes at (a) 120 °C (b) 150 °C (c) 180 °C (d) 200 °C (e) 250 °C and (f) the dependency of K (log scale) on annealing temperature.

Smaller fraction of porosity can lead to the larger solid-solid interface, thereby higher percolation paths for the charge carriers. The application of silver films as electrodes does require enhanced percolation paths facilitating the easier flow of charge carriers.

Thus, in the previous sections it is described that the process of fabrication of films of silver via nano-dispersion route involves series of steps. The importance of each step is enormous and unavoidable. As mentioned in the introduction section of the present chapter, a combustible precursor route can be established for the fabrication of the films of silver.

4.3.6 Solution combustion derived silver film

Solution combustion is focused on the balanced redox reaction, where the stoichiometric proportion of the fuel and the oxidizer yields maximum heat output (or the enthalpy). In the literature, researchers have developed a series of metal oxides via combustion reaction. Here, the process is extended to the fabrication of pure-metallic films. Silver being high electrically conductive; thus, it is preferred in the present study. The balanced redox reaction (equation 4.1) comprising silver nitrate ($AgNO_3$) and citric acid ($C_6H_8O_7$) in the aqueous medium is employed. The dried aliquots of the combustible precursor are analysed through DSC and manifested in the fig. 4.13(a).
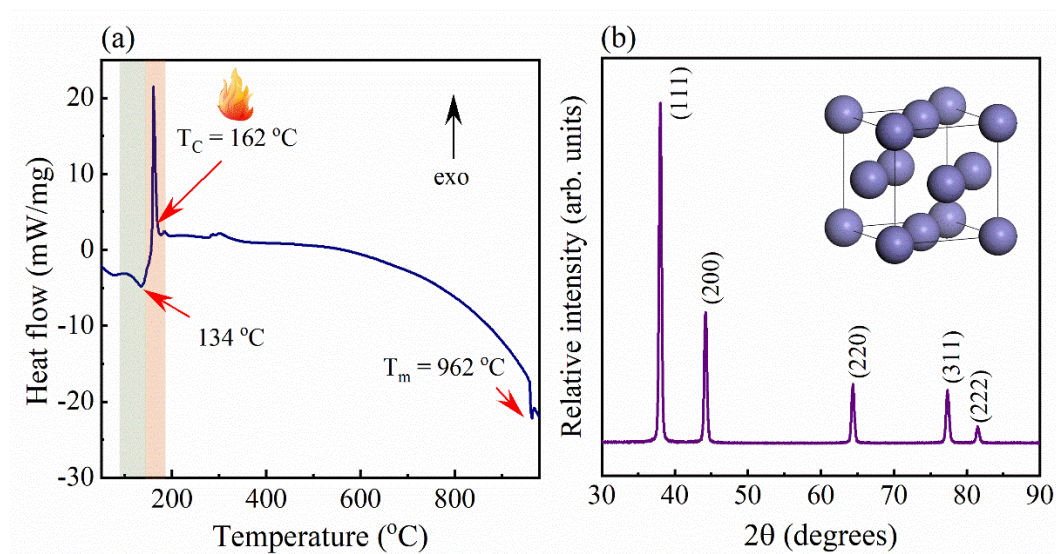

Fig. 4.13 (a) DSC thermogram of combustible precursors of silver (b) GIAXRD of spray deposited silver film and the inset: FCC structure.

91

The endothermic response of the DSC at 134 °C is due to the elimination of the bound water. Further, a sharp exotherm at 162 °C corresponds to the redox reaction yielding pure metallic silver. The formed silver undergoes melting at 962 °C, which is visualized in the DSC as an endothermic response. Thus, minimum temperature of formation of silver from the present combustible precursors is 162 ℃. To fabricate the film of silver, the combustible precursor is loaded into a household sprayer and the atomized drops of combustible precursor is made to touch the hot glass substrate, which is maintained at 162 ℃. The GIAXRD of the resulting film shows the face centered cubic (FCC) structure, confirming the presence of pure silver (fig. 4.13(b)). The exothermic reaction between the silver nitrate and the citric acid yield the pure silver. On the other hand, the product-silver particles undergo sintering to form a continuous film. The network formed by interconnected silver particles results in the percolation path for the flow of charge carriers. The energy required to the sintering process is provided by the exothermic combustion reaction, for which the enthalpy of the reaction is negative. To support the above statements, an innovative approach is adopted. Where, the combustible precursors of silver are sprayed onto the uncoated copper grid at 160 ℃ (fig. 4.14).
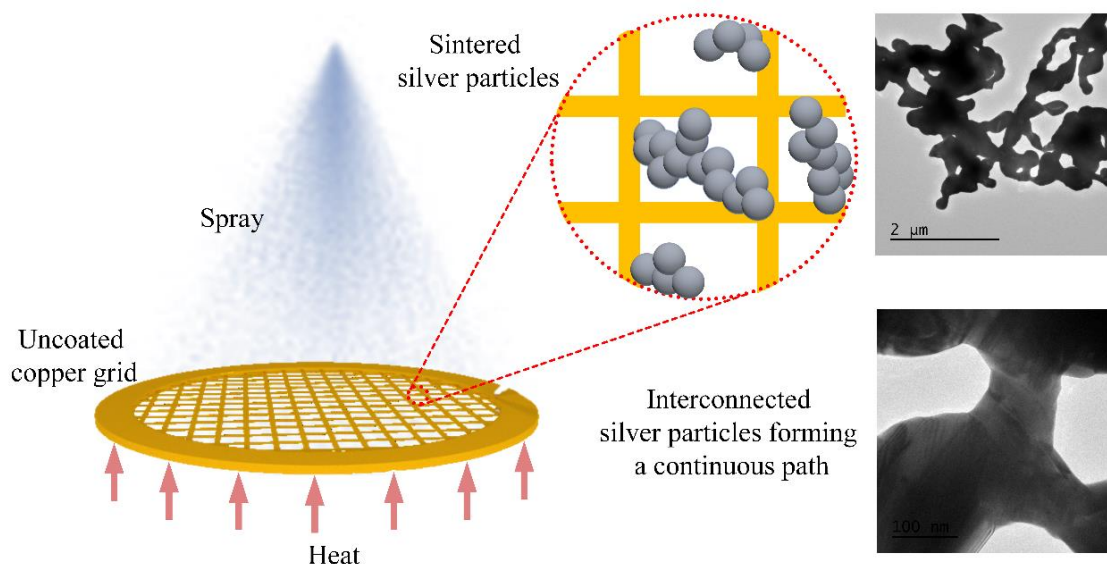

Fig. 4.14 Deposition and sintering of silver nanoparticles on an uncoated copper grid along with TEM micrographs.

The TEM micrographs of the same depicts the sintering and the formation of continuous path of silver particles. The advantage of which is fetched and utilized in the formation of silver film. Thus, the hot substrate maintained at a temperature minimum of 160 ℃ is utilized for the fabrication of the film of silver. The film deposited (~1 µm, thick) via sprayed combustible precursors on a glass substrate showed an electrical conductivity of the order ~10^7 Sm^{-1}, suffice the requirement of being an electrode for optoelectronic devices. The process of fabrication of silver film from the combustible precursors is simple, fast and cost effective than the nano-dispersion route. The spraying of combustible precursor is viable to from a continuous film of metallic-silver.

4.4 Conclusions

A systematic study of method of elimination of morphological irregularities of nano-dispersions is carried out using dwell-time and thermal annealing approach. The time elapse between the drop casting of a single drop and the thermal annealing is defined as the dwell-time. The tuned dwell-time of 10 min at 200 ℃ resulted in the uniform deposition of polyol derived silver is demonstrated. The sintering kinetics of the deposited silver particles have revealed that the parameter K, which depicts the grain growth depends on the annealing temperature. The increment in the magnitude of K with annealing temperature results in the creation of percolation paths for the charge carriers. Further, the sprayed combustible precursor of silver resulted in the continuous, and electrically conducting (~10^7 Sm^{-1}) film.

Page left intentionally blank

CHAPTER 5

APPLICATION OF SOLUTION COMBUSTION PROCESSED IZTO IN THIN FILM TRANSISTORS
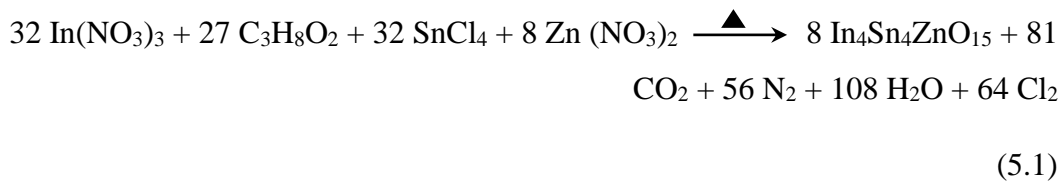
5.1 Introduction

IZTO is a co-doped system with tunable properties. The versatility in the properties is the resultant of co-doping of zinc and tin in indium oxide. As a result of co-doping, IZTO with stoichiometry - In:Zn:Sn::1.4:0.3:0.3 is electrically conductive, which is nearly equals to commercial grade ITO (Hoel et al. 2010). Further, the semiconducting IZTO with the stoichiometry - In:Zn:Sn::4:1:4 shows a field effect mobility of two order, higher than a-Si:H (Kim et al. 2010). The fabrication and characterization of conducting IZTO is detailed in the chapter 3. In the present chapter, fabrication of semiconducting IZTO along with application of both conducting and semiconducting IZTO in the TFTs is described. The performance of the TFTs not only depend on the quality of the semiconductor, also the permittivity of the dielectric employed. Initially, the performance of the semiconducting IZTO with conventional thermally grown SiO_2 is analysed. Further to realize low voltage operation of the TFTs, the conventional SiO_2 is replaced by high permittivity sodium β-alumina.

5.2 Experimental methods

To reveal the efficacy of the conducting IZTO film, series of TFTs with a bottom gate top contact (BGTC) [glass / IZTO / PMMA / Pentacene / gold] architecture was fabricated on to a glass substrate with spin-coated (1000 rpm, 30 s with annealing at 90 ℃ for 30 min.) commercial poly(methyl methacrylate) – PMMA (Microchem XR1541) as the dielectric layer followed by thermally evaporated 50 nm thick pentacene as the channel layer. Finally, the gold contacts (30 nm) were evaporated thermally with a channel dimension of W:L::1000:100. The fabricated devices were characterized in the ambient atmosphere in the dark using a semiconductor characterization system with the KEITHLEY-4200 source meter. The performance

parameters such as μ_{sat}, $I_{on}:I_{off}$, and V_{th} were estimated from the output and transfer characteristics.

The combustible precursor of semiconducting IZTO was prepared with 2-ME as both fuel and the oxidizer. The precursor was ensured to be free of external fuel. The relative amounts of combustible precursors were selected based on the stoichiometric combustion reaction (equation 5.1). 0.1 M precursor comprising 300 mg indium nitrate $(In(NO_3)_3$, Alfa Ascer), 259.8 mg tin(IV) chloride $(SnCl_4$, Sigma) and 47.2 mg zinc nitrate $(Zn(NO_3)_2$, Sigma) was dissolved in 22 ml of 2-ME.

$$32\ In(NO_3)_3 + 27\ C_3H_8O_2 + 32\ SnCl_4 + 8\ Zn\ (NO_3)_2 \xrightarrow{\ \blacktriangle\ } 8\ In_4Sn_4ZnO_{15} + 81$$
$$CO_2 + 56\ N_2 + 108\ H_2O + 64\ Cl_2$$

(5.1)

To understand the thermal behaviour of IZTO precursor, aliquots of dried precursor (8 h in a vacuum oven at 50 °C) weighing 18 mg was utilized for the thermal analysis using DSC, with a heating rate of 10 °Cmin^{-1}. To deposit the semiconducting IZTO film, the surface of the substrate was subjected to oxygen plasma treatment for 30 s. The IZTO precursor was spin coated by two-stage spinning method (1st stage: 500 rpm for 5 s; 2nd stage: 2000 rpm for 30 s). The as-spun film was soft baked at 120 °C for 10 min followed by an annealing at 200 °C for 1 h. To understand the structural nature of the IZTO thin film GIAXRD with an angle of incidence of 0.5° was performed. The morphology and elemental distribution on the surface of IZTO film were analysed using Scanning Electron Microscopy (SEM, Hitachi S3400N) and Energy Dispersive Spectroscopic (EDS, Thermo Noran NSS200) mapping. EDS mapping was carried out with the frame time of 20 s. XPS spectra (AXIS Supra; Kratos Analytical, UK) were recorded to understand the surface chemical composition and the oxidation states cations of IZTO. For XPS, a chamber pressure of 2×10^{-7} Pa, and a monochromatic Al Kα x-ray source were used. The XPS spectra were calibrated using C 1s centered at 284.7 eV, and the state of oxygen was analysed by deconvoluting high-resolution O 1s spectra. For the peak fitting, a product of Gaussian and Lorentzian functions (GL) was used in a software package-CASAXPS Version 2.3.19PR1.0. Also, the topographical nature of IZTO films was analysed by a non-contact mode AFM.

To fabricate BGTC [Si(p++) (resistivity < 0.005 Ω-cm) / SiO$_2$ / IZTO / Al] TFTs, the SiO$_2$ substrate is initially solvent cleaned and dried under nitrogen gas. Hydrophilicity is imparted by UV ozone treatment. The cleaned surface of SiO$_2$ is used for the deposition of semiconducting IZTO, the process of deposition and annealing is detailed in the previous paragraphs. Finally, top aluminium contacts were deposited by maintaining the W:L ratio of 10 (W = 1000 μm and L = 100 μm). The cross-sectional micrograph of the TFT was recorded using Field Emission Gun-Scanning Electron Microscopy (FEG-SEM, JSM-7600F). The fabricated devices were characterized in the ambient atmosphere in the dark using a semiconductor characterization system with the KEITHLEY-4200 source meter. The performance parameters such as μ_{sat}, I_{on}:I_{off}, and V_{th} were estimated from the output and transfer characteristics.

In order to realize low voltage operation of the TFTs, the conventional SiO$_2$ is replaced by sodium β-alumina. The β-phase of sodium incorporated alumina (Na:Al::1:11) is prepared using sol-gel technique. Initially, sodium nitrate (NaNO$_3$; Nice chemicals, India) and aluminium nitrate (Al(NO$_3$)$_3$, Alfa Aesar) were dissolved in a mixture of two solvents acetonitrile (AN,C$_2$H$_3$N, Sigma) and ethylene glycol (EG, C$_2$H$_6$O$_2$, Sigma) (AN: EG :: 1: 9 (v/v)). The resulting homogeneous solutions were mixed by maintaining a metal ion ratio of Na:Al::1:11. Both the precursors were stirred for 8 h and filtered through 0.45 μm PTFE filters before the usage.

To fabricate BGTC [Si(p++) (resistivity < 0.005 Ω-cm) / sodium β-alumina / IZTO / Al] TFTs, the Si(p++) substrate was initially solvent cleaned and dried under nitrogen gas. Hydrophilicity is imparted by UV ozone treatment. The cleaned surface of Si(p++) was used for the deposition of sodium β-alumina using spin coating followed by thermal annealing at 350 ºC for 1 h. Further, the Si(p++) / sodium β-alumina, was utilized for the deposition of semiconducting IZTO. Finally, top aluminium contacts were deposited by maintaining the W:L ratio of 10 (W = 800 μm and L = 150 μm). The fabricated devices were characterized in the ambient atmosphere in the dark using a semiconductor characterization system with the KEITHLEY-4200 source meter. The performance parameters such as μ_{sat}, I_{on}:I_{off}, and V_{th} were estimated from the output and transfer characteristics.

5.3 Results and discussion

5.3.1 TFTs with IZTO (In$_{1.4}$Zn$_{0.3}$Sn$_{0.3}$O$_3$) as the gate electrode

To reveal the efficacy of the transparent, conducting IZTO, TFTs with an architecture Glass / IZTO / PMMA / Pentacene / Au are fabricated (fig. 5.1(a)). The capacitive response of PMMA as a function of the frequency is illustrated in fig. 5.1(b). The output and transfer characteristics of TFT are as presented in fig. 5.1(c) and fig. 5.1(d). The performance parameters such as μ_{sat}, I_{on}:I_{off}, and V_{th} were estimated to be 0.44 cm^{2}V^{-1}s^{-1}, 10^3 and -12.5 V respectively. Also, the hysteresis observed in both output and transfer characteristics is minimum. It shows the capability of solution combustion derived IZTO as a conducting film in TFTs.
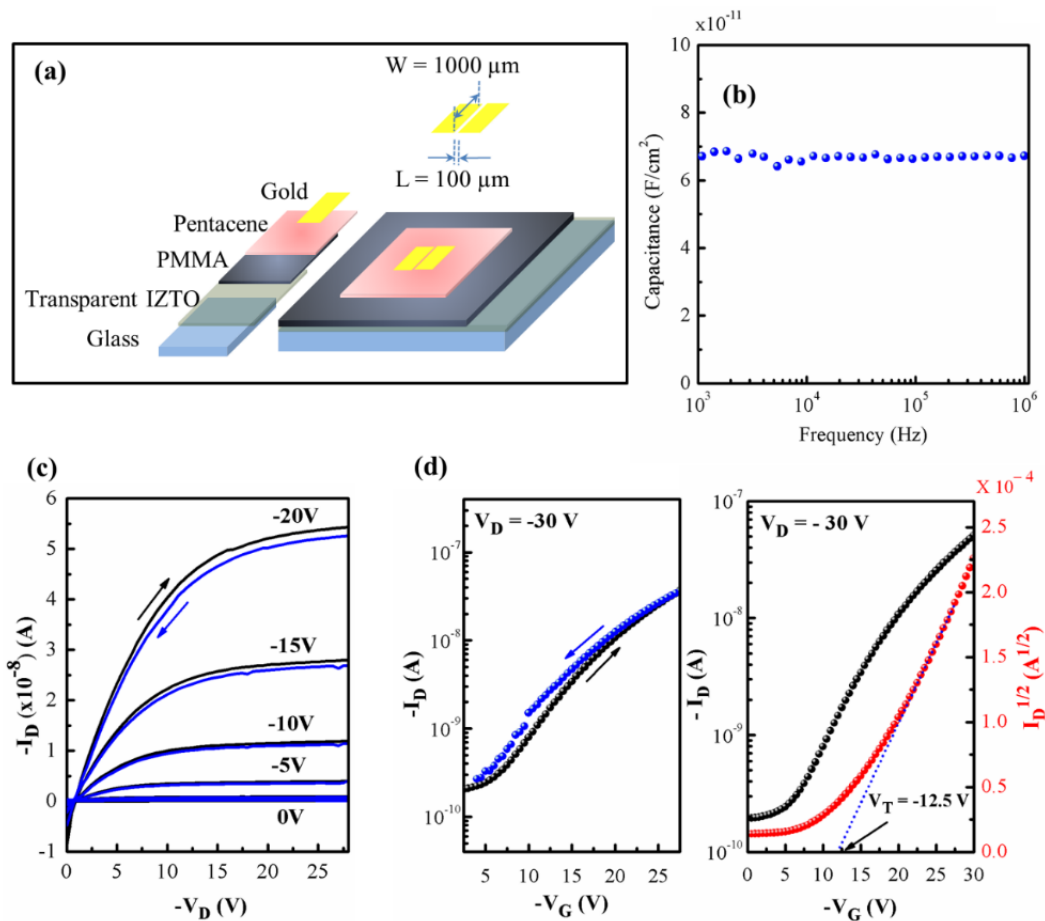

Fig. 5.1 (a) BGTC architecture, (b) capacitance vs. frequency of the capacitor, (c and d) output and transfer (hysteresis) characteristics of TFT.

5.3.2 TFTs with IZTO (In$_4$ZnSn$_4$O$_{15}$) as the semiconducting layer

5.3.2.1 Fuel free solution combustion of semiconducting IZTO

The precursor (0.1M) has an excess amount of organic solvent 2-ME. The quantification of the excess amount can be calculated based on the balanced chemical reaction (equation 5.1); the corresponding number of moles of reactants participated in the reaction are given in table 5.1. The total amount of solution involved in the reaction is calculated from the desired molarity (equation 5.2). Thus, the volume of the solution obtained from equation 5.2, is 23.27 ml. The total solution also involves the quantity of fuel. The amount of 2-ME required for the complete combustion is 66 µl (mass of 2-ME / density of 2-ME). Thus, 0.3 % of the 2-ME is acting as the fuel, and the rest is the medium for the dissolution. Further, experimental evidence for the relative fractions of fuel and the solvent is understood by the thermal analysis. The DSC thermogram renders strong evidence for the above statements. The large area endotherm at 125 °C (boiling point of 2-ME) shows the removal of excess 2-ME and the evaporation of which initiates at 115 °C (onset temperature, fig. 5.2). The complete removal of 2-ME was not accomplished, which is evident from the adjacent sharp exothermic response at 142 °C. The amount of 2-ME, which was in complexation with the nitrate dragged the decomposition temperature to a higher value of 142 ºC.

Table 5.1 The number of moles of reactants involved in the reaction

Reactants	Coefficients	Moles	Mass (g)
In(NO$_3$)$_3$	32	0.000997232	0.3
C$_3$H$_8$O$_2$	27	0.000084141	0.064026
Zn(NO$_3$)$_2$	8	0.00024930	0.047216
SnCl$_4$	32	0.000997232	0.259800

$$0.1 = \frac{0.000997232 + 0.000084141 + 0.000997232 + 0.00024930}{\text{Volume of the solution in litres}}$$

(5.2)

The combustion of the nitrate-fuel complex had begun at a temperature near to the temperature of decomposition of solvent (125 ℃) confirming the dual nature of the 2-ME. Due to a large fraction of the 2-ME acting as the solvent, the area under the endothermic peak is considerably higher than the exothermic counterpart. The existence of endo- and exotherms were previously reported (Kim et al. 2011a) (Salgueiro et al. 2017) but, the in the present study it is supported with a quantification.
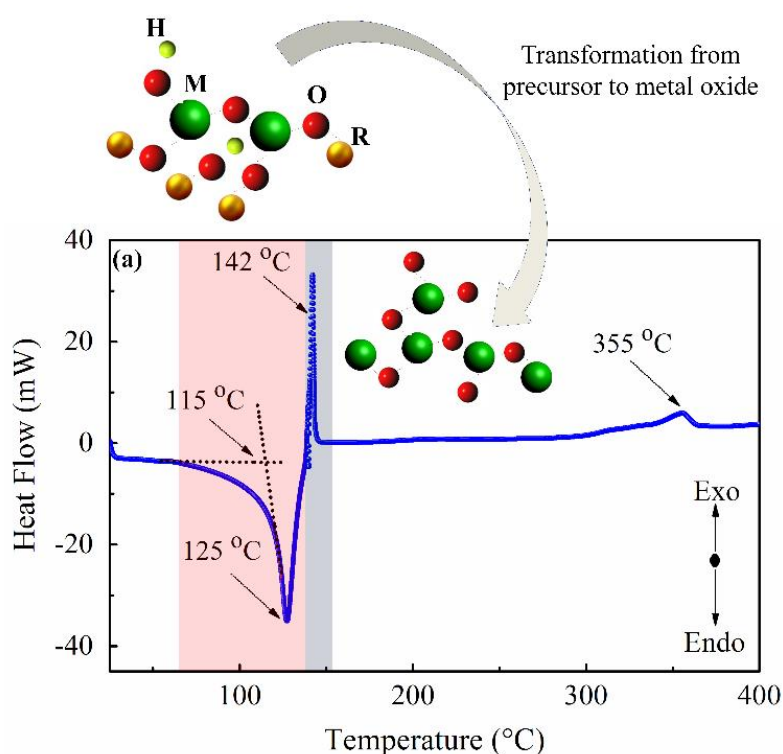
Fig. 5.2 (a) DSC thermogram of the combustible precursor (M-metal, H-hydrogen, O-oxygen, R-methoxy group).

Further, the absence of diffraction peaks in the GIAXRD pattern of the IZTO film depicts that the film is amorphous (fig 5.3(a))), with a surface roughness of 3.2 nm, which is estimated from AFM (fig. 5.3(b)). The reason for the amorphous phase of the film is due to the high surface to volume ratio of the film, which facilitates transfer of heat resulting in enhancement of crystallization temperature (Sanchez-Rodriguez et al. 2013). The IZTO film shows featureless morphology with a uniform distribution of indium, zinc, tin, and oxygen confirmed through EDS-mapping of the surface of the film (fig. 5.4). The fraction of indium and tin on the surface is higher than the zinc, due to the stoichiometry employed for the present study (In:Zn:Sn::4:1:4).

Fig. 5.3 (a) GIAXRD and (b) AFM surface topography of IZTO thin film

Fig. 5.4 EDS mapping of the surface of IZTO depicting the distribution of elements.

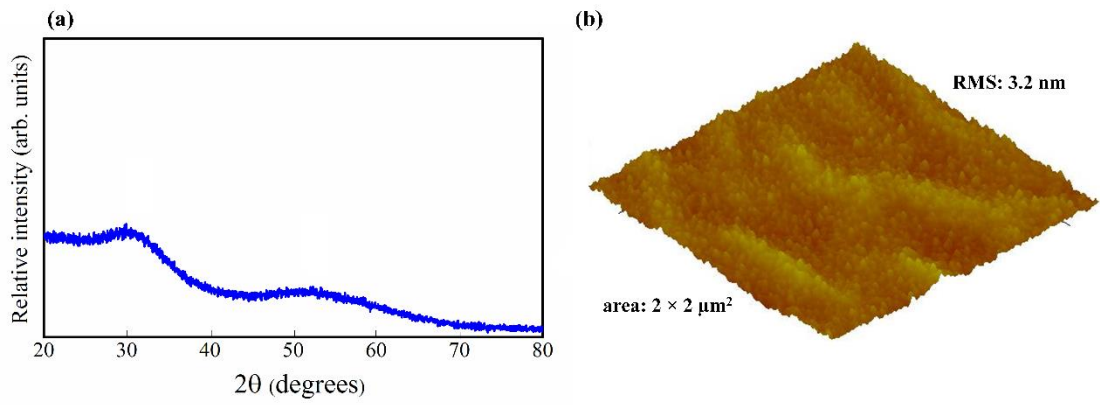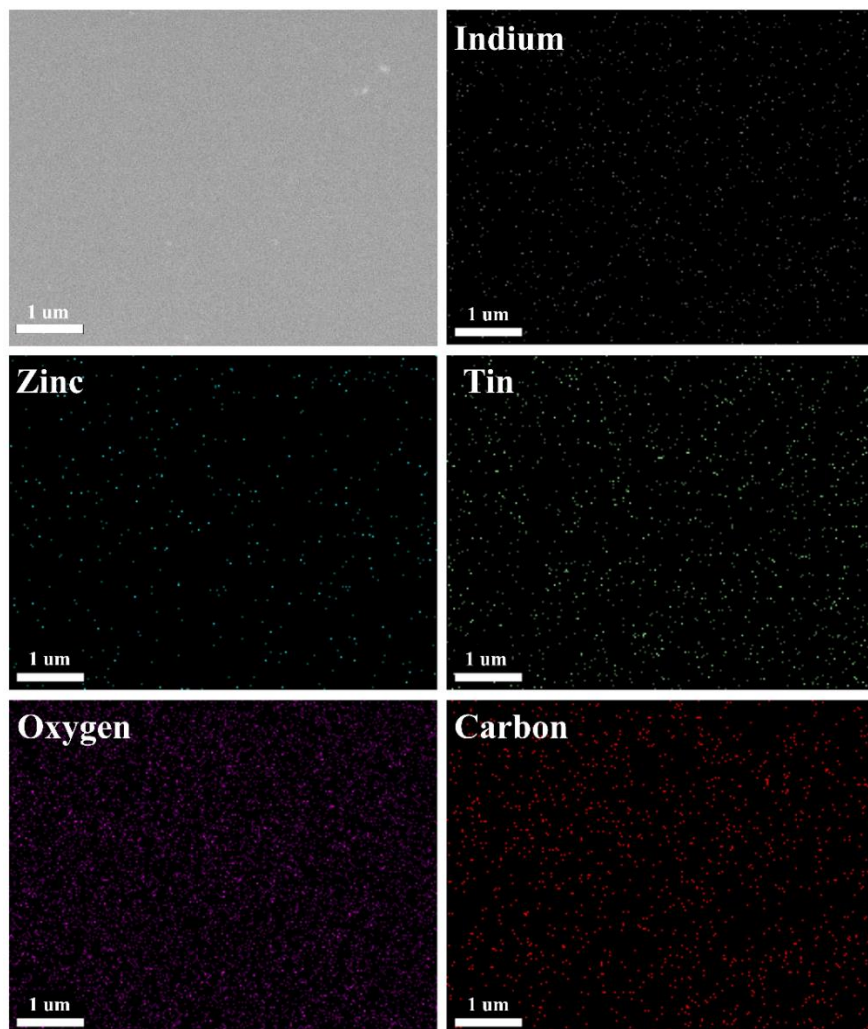To understand the chemical states of elements on the surface of the IZTO thin film, XPS analysis is performed. Fig. 5.5 shows the XPS survey scan of IZTO thin film, depicting the presence of indium, zinc, tin, oxygen and adventitious carbon.
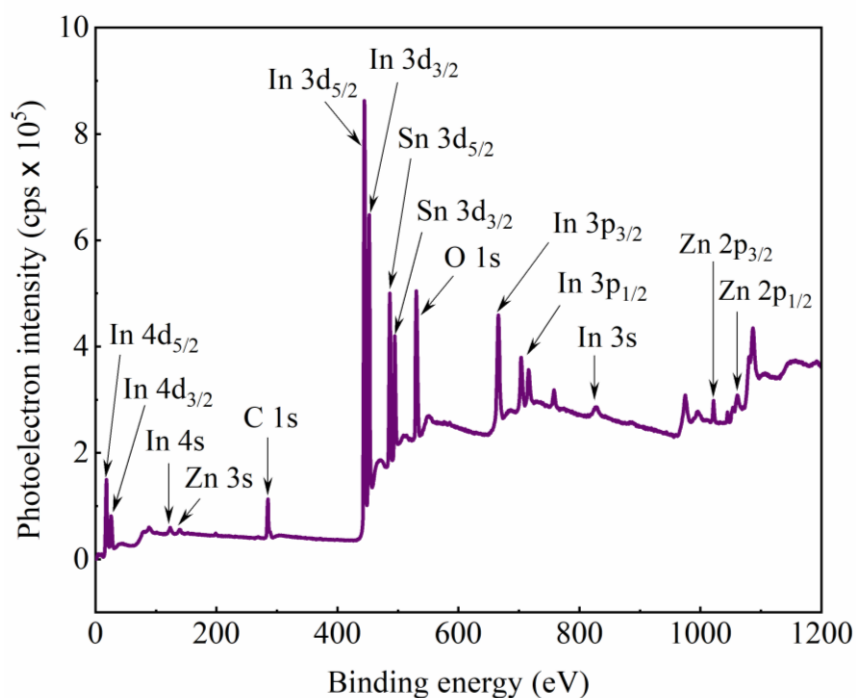
Fig. 5.5 XPS survey spectrum of thin film of IZTO

Peak fit analysis of XPS high-resolution spectra were carried out after calibrating with C 1s spectrum. Figure 5.6(a) shows the deconvoluted C 1s peak, four distinct synthetic features positioned at 284.7 eV, 287.7 eV, 286.2 eV, and 288.7 eV attributed to C-H/C-C, C=O, C-O, and O=C-O respectively. The C-H/C-C peak considered to be highly intense and the position of which is used for the calibration (peak fit parameters and the procedure can be found in Appendix II). In continuation, the oxidation states of indium, zinc, and tin were estimated based on the deconvoluted features of respective high-resolution spectra. Peaks centered at 444.6 eV (Clark et al. 1980), 1021.8 eV (Battistoni et al. 1981) and 486.4 eV (Baronetti et al. 1986) corresponds to In^{3+}, Zn^{2+}, and Sn^{4+}, respectively (fig. 5.6 (b-d)). Further, the efficiency of the combustion reaction in forming the metal oxide was assessed through deconvolution of O 1s XPS response (Fig. 5.6(e)); three principal signatures at 529.9 eV, 531.2 eV and 532.2 eV corresponds to metal oxide, metal hydroxide, and surface adsorbed oxygen (Kim et al. 2010). The

fraction of metal oxide from the precursor found to be ~56.5 %; the formation of a high fraction of metal oxide at 200 ℃ plays a crucial role in deciding electronic properties of the film.

Fig. 5.6 XPS spectra of (a) C 1s (b) In $3d_{5/2}$ (c) Zn $2p_{3/2}$ (d) Sn $3d_{5/2}$ and (e) O 1s of IZTO film annealed at 200 ℃. In all the cases, the open ci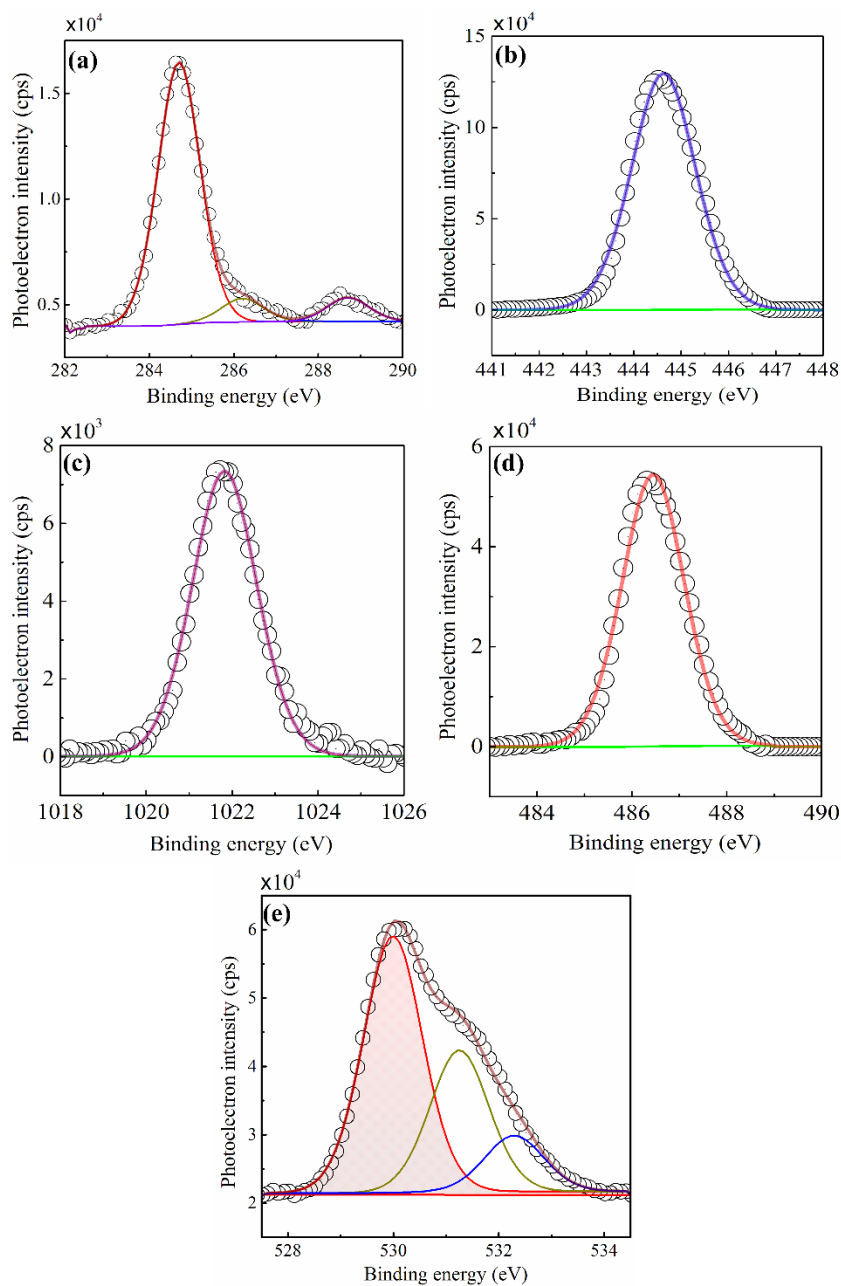rcles represent the experimental data, and both deconvoluted peaks and the peak envelope are represented with continuous lines.

The lower intensity of Zn^{2+} (fig. 5.6(c)) peak compared to In^{3+} and Sn^{4+} (fig. 5.6(b) and 5.6(d)) is attributed to the composition of IZTO (In:Zn:Sn::4:1:4), which matches with the EDS results (fig. 5.4).

5.3.2.2 Performance of TFTs based on semiconducting IZTO and SiO$_2$

To elucidate the performance of the combustion-derived semiconducting IZTO thin film as an active material, a BGTC TFT (fig. 5.7(a)) with 300 nm SiO$_2$ as the gate dielectric is fabricated. Fig. 5.7(b) shows the cross-sectional FEG-SEM micrograph of the TFT; the thickness of IZTO film was found to be ~45 nm. The top aluminium electrodes were thermally evaporated by maintaining W:L = 10. The TFT characterizations such as output (I_D vs. V_D) and transfer (I_D vs. V_G) was performed in the ambient atmosphere. A minimum of five devices were measured to estimate the performance parameters such as average μ_{sat}, I_{on}:I_{off}, and the V_{th}. Fig. 5.7(c) and (d) shows the output and transfer characteristics of the Si/SiO$_2$/IZTO/Al TFT respectively.
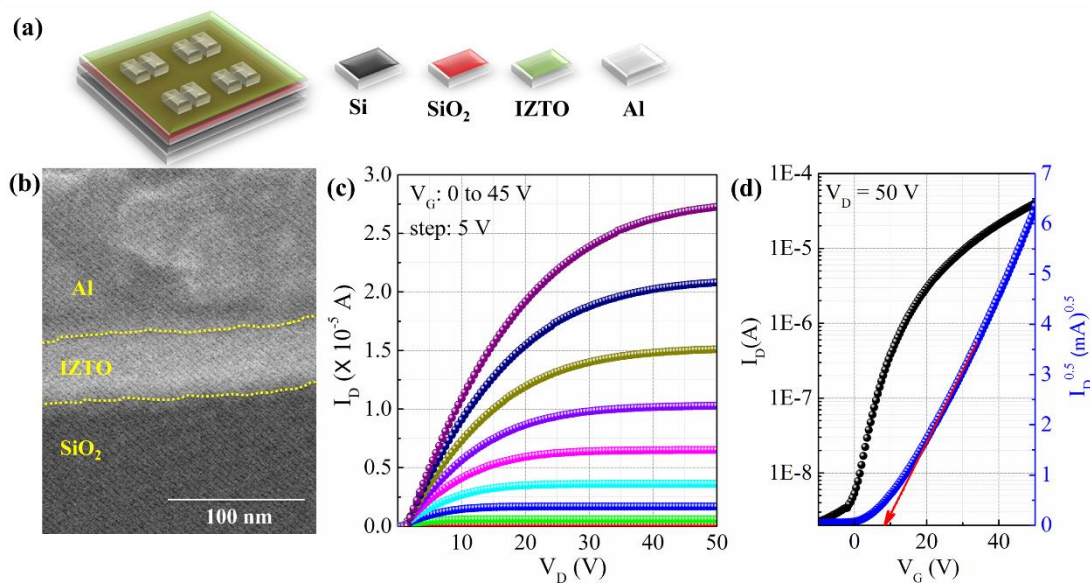
Fig. 5.7 (a) Schematic of the TFT (b) cross-sectional FEG-SEM micrograph of the TFT (c) output (d) transfer characteristics of Si / SiO$_2$ / IZTO / Al devices.

The μ_{sat} estimated to be 0.50 ± 0.02 cm^2 V^{-1} s^{-1} with I_{on}:I_{off} of 1.25×10^4 and V_{th} of 6.6 ± 0.79 V. The present study conveys that the existence of combustion chemistry along with the low decomposition temperature of indium nitrate makes the system to undergo

easy transformation into metal oxide. The performance parameters of the device is tabulated in the table 5.2.

Table 5.2 Performance parameters of the Si / SiO₂ / IZTO / Al, TFTs

Dielectric	Thickness (nm)	Dielectric constant	μ_{sat} $(cm^2V^{-1}s^{-1})$	V_{th} (V)	$I_{on}:I_{off}$
SiO₂	300	3.9	0.50 ± 0.02	6.6 ± 0.79	1.25×10^4

An additional advantage of the present system is its minimum carbon content (fuel free); the presence of reducing agents such as acetylacetone, nitroacetylacetone, urea, and glycine etc., is not mandatory. To further enhance the performance with low voltage operation of the TFTs, a high permittivity sodium β-alumina is incorporated into the system instead of conventional SiO₂.

5.3.2.3 Sol-gel processed thin films of sodium β-alumina

The spin-coated film of sodium β-alumina is analysed for the structural, compositional and topographical behaviour. The GIAXRD pattern shows the crystalline film (fig. 5.8(a)), and the topography of the film shows the RMS roughness of 0.64 nm (fig. 5.8(b)).
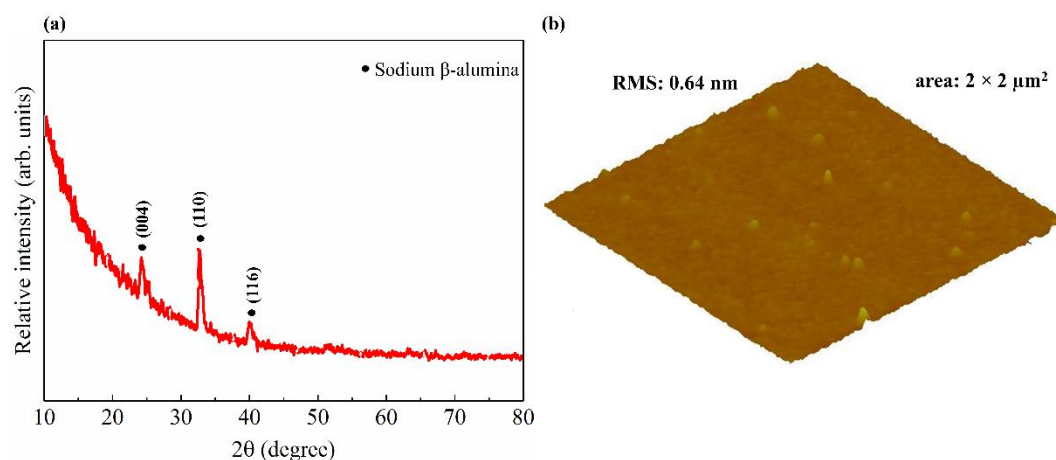
Fig. 5.8 (a) GIAXRD and (b) AFM topography of spin-coated sodium β-alumina.

105

The low roughness plays a significant role in determining the quality of the semiconductor-dielectric interface. Further, the surface chemical composition of the surface of the sodium β-alumina was analysed using XPS. The survey spectrum (fig. 5.9) of XPS shows the presence of constituent elements.
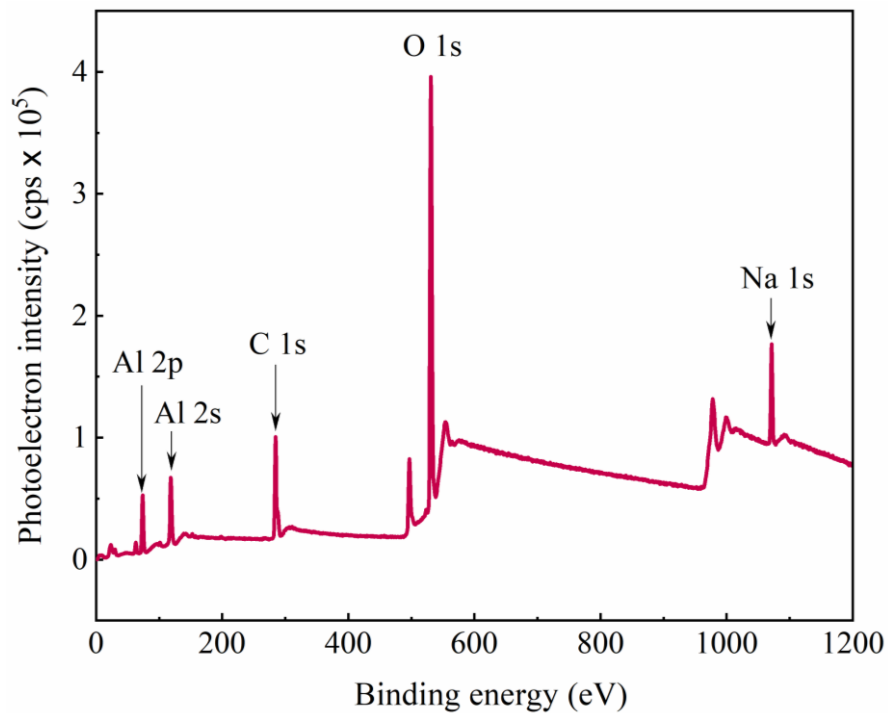
Fig. 5.9 XPS survey spectrum of thin film of sodium β-alumina.

Fig. 5.10 shows peak fit analysis of C 1s with features: C-C/C-H at 284.7 eV, C-O at 286.2 eV, C=O at 287.7 eV, and O=C-O at 288.8 eV, CO_3^{2-} at 289.2 eV. The peak centered at 284.7 eV is used for the calibration (all peak positions and fitting parameters is in Appendix III). The responses at 74.08 eV and 1061.6 eV corresponds to Al 2p and Na 1s, respectively. Also, the O 1s spectra are deconvoluted into three principal features at 530.8 eV, 531.8 eV, and 532.8 eV corresponds to lattice oxygen, oxygen in metal hydroxide and the surface adsorbed species such as H_2O, and CO_2, respectively. The lattice oxygen is found to be ~53 % calculated from the relative area fractions. The high percentage of metal oxide on the surface of the film along with low roughness contributes greatly to the performance of the TFTs. To estimate the capacitance of the ~106 nm thick sodium β-alumina, a capacitor with the MIM architecture is fabricated

(fig. 5.11(a)) and the capacitance vs. voltage is plotted (fig. 5.11(b)), the capacitance of the device is found to be 17.5 nFcm^{-2} at 100 kHz.
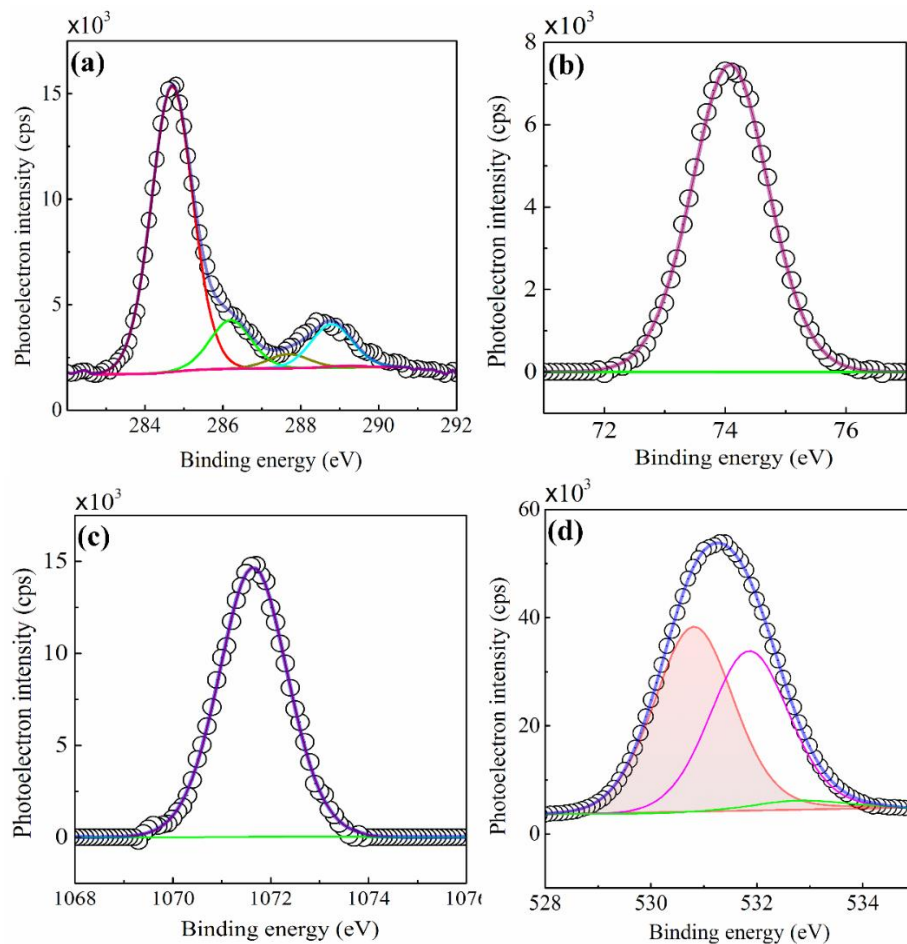
Fig. 5.10 (a) XPS spectrum of (a) C 1s (b) Al 2p (c) Na 1s and (d) O 1s of the sodium β-alumina. In all the cases, the open circles represent the experimental data, and both deconvoluted peaks and the peak sum are represented with continuous lines.

5.3.2.4 Low voltage operation of IZTO TFTs

Achieving low voltage operation of the IZTO based TFTs is realized by replacing conventional SiO$_2$ by sodium β-alumina. The architecture of the TFTs incorporated with sodium β-alumina is presented in the fig. 5.12(a).
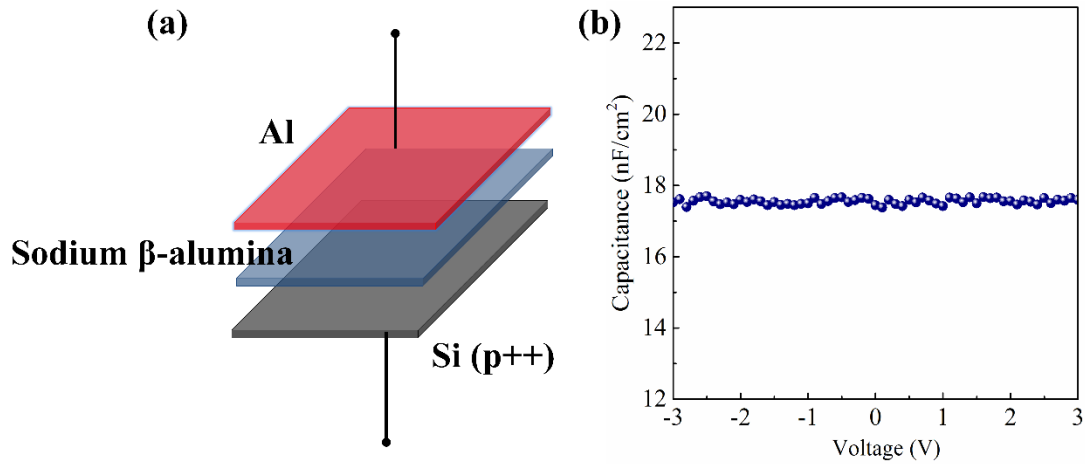
Fig. 5.11 (a) Schematic of the capacitor (b) capacitance vs. voltage plot at 100 kHz.

Table 5.2 Performance parameters of Si / sodium β-alumina / IZTO / Al, TFTs

Dielectric	Thickness (nm)	Dielectric constant	μ_{sat} $(cm^2V^{-1}s^{-1})$	V_{th} (V)	$I_{on}{:}I_{off}$
Sodium β-alumina	106	21	4.21 ± 0.18	0.47 ± 0.08	1.4×10^2

The output and transfer characteristics of the TFTs is shown in the figure 5.12(b) and (c). The TFTs are found to operate at low voltage (< 3 V) and exhibited μ_{sat}, $I_{on}{:}I_{off}$, and V_{th} of 4.21 ± 0.18 cm^2 V^{-1} s^{-1}, 1.4×10^2 and 0.47 ± 0.08 V, respectively. Series of devices were fabricated and characterized to reveal to reproducibility of the performance (output and transfer characteristics of the similar TFTs are shown in Appendix IV). The performance parameters of TFTs with two different dielectrics are presented in table 5.2. The improved performance of the TFTs based on IZTO and sodium β-alumina is due to high dielectric constant of sodium β-alumina and the large spatial distribution of s-orbitals of IZTO (fig. 2.4) which allowed the smooth transport of charge carriers thereby increasing the saturation mobility of the TFTs. Further, the performance of the devices is compared with the literature and a table (table 5.3) showing comparison of the performance parameters is presented.

Table 5.2 Performance parameters of various IZTO based TFTs

Dielectric	T_P (°C)	μ_{sat} (cm^{2}V^{-1}s^{-1})	V_O (V)	V_{th} (V)	Ref.
Self-assembled nanodielectric	400	100 ± 13	≤ 3	1.0	Kim et al. 2010
Zirconia	300	2.65 ± 0.43	≤ 3	0.44	Bukke et al. 2018
Zirconia	300	15.42 ± 4.01	≤ 3	0.5	Bukke et al. 2018
Silicon nitride	600	4.36	≤ 40	2.1	Bong et al. 2011
Sodium β-alumina	200	4.21 ± 0.18	≤ 3	0.47	Present study
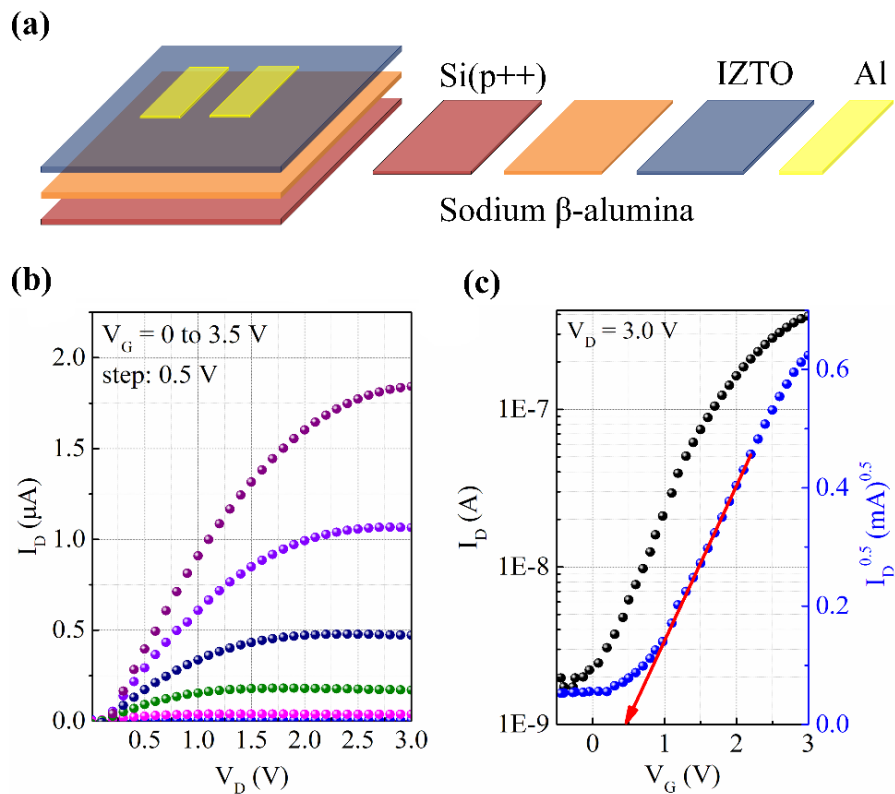
Fig. 5.12 (a) Schematic, (c) output, and (d) transfer characteristics of the TFT.

5.4 Conclusions

Low-temperature solution combustion processed amorphous IZTO semiconductor is fabricated in this study. The fuel-free approach resulted in the

amorphous phase of IZTO with uniformly distributed indium, zinc, tin and oxygen on the surface of the spin coated ~45 nm thick film. The performance of the TFTs with conducting IZTO as gate electrode, pentacene and PMMA as semiconductor and the gate dielectric respectively, have revealed acceptable performance. In addition, the TFTs based on the IZTO semiconductor and the SiO_2 dielectric have shown a μ_{sat} of 0.50 ± 0.02 cm^2 V^{-1} s^{-1} with I_{on}:I_{off} of 1.25×10^4 and V_{th} of 6.6 ± 0.79 V. Low voltage (< 3 V) operation of the TFTs is successfully achieved by replacing SiO_2 by a high permittivity (~21 at 100 kHz) sodium β-alumina. The TFTs based on IZTO semiconductor and the sodium β-alumina have shown μ_{sat}, I_{on}:I_{off}, and V_{th} of 4.21 ± 0.18 cm^2 V^{-1} s^{-1}, 1.4×10^2 and 0.47 ± 0.08 V respectively.

CHAPTER 6

CONCLUSIONS

In the present work, low-temperature fabrication of functional conducting and semiconducting metal oxides such as ITiO and IZTO are addressed via the solution combustion technique. Also, the challenges associated with the nano-dispersion based deposition in terms of morphology and the sintering is studied, followed by easy deposition of combustible precursors of silver using simple spray method, is addressed. Finally, the application of both conducting and semiconducting IZTO are employed as components of TFTs. Based on experimental findings and analysis, the following conclusions are drawn:

→ The combustible precursors of ITiO ($In_{14}TiO_{23}$) have resulted in the formation of metal oxide at a temperature of 150 ºC. The films of ITiO are optically transparent and electrically conductive. The highest optical transparency is found to be ~100 % with 51.3 % of lattice oxygen at an annealing temperature of 350 ºC. Hall effect measurements have revealed a maximum conductivity of 20 Scm^{-1} with a carrier concentration of 10^{19} cm^{-3} and Hall mobility of ~2 cm^{2}V^{-1}s^{-1} at 450 ºC.

→ Low-temperature solution combustion of transparent and conducting crystalline IZTO ($In_{1.4}Sn_{0.3}Zn_{0.3}O_3$) is established at 200 ºC. The IZTO thin film annealed at 200 ºC are electrically conductive (100 Scm^{-1}) and optically transparent (~83 %). The Hall effects measurements of IZTO thin films have revealed a carrier concentration of 10^{19} cm^{-3} and the maximum Hall mobility of 5.92 cm^{2}V^{-1}s^{-1} at 400 ºC.

→ A comprehensive study on the morphological irregularities of self-aligned micrometer thick silver films from nano-dispersion is controlled by tuned dwell-time. The coffee ring formation, center deposit are the outcomes of infinite and zero dwell-times, respectively. The modulated dwell-time of 10 min at 200 °C resulted in the uniform deposit. The sintering kinetics involving estimation of grain growth parameter K, which increases with the annealing temperature

depicting decreased fractional porosity. The decrement in the porosity is directly related to the high probability of percolation paths for the movement of charge carriers

→ The solution combustion derived silver films at 160 ºC are electrically conductive (10^7 Sm^{-1}).

→ The TFTs comprising conducting IZTO (In$_{1.4}$Sn$_{0.3}$Zn$_{0.3}$O$_3$), PMMA, and pentacene as gate electrode, dielectric, and the semiconductor have revealed μ_{sat}, I$_{on}$:I$_{off,}$ and V$_{th}$ of 0.44 cm^{2}V^{-1}s^{-1}, 10^3 and -12.5 V respectively. Fuel free solution combustion of semiconducting amorphous IZTO (In$_4$Sn$_4$ZnO$_{15}$) is fabricated at 200 °C with RMS roughness of 3.9 nm consisting of a maximum lattice oxygen of ~56.5 %. The 2-ME employed as the solvent and the fuel and 0.3 % of which served the purpose of fuel.

→ The conventional SiO$_2$ based BGTC TFTs with solution-processed semiconducting IZTO fabricated at 200 °C has exhibited a μ_{sat} of 0.50 ± 0.02 cm^2 V^{-1} s^{-1} with I$_{on}$:I$_{off}$ of 1.25 × 10^4 and V$_{th}$ of 6.6 ± 0.79 V. Low voltage operation (< 3 V) of TFTs is achieved by replacing conventional SiO$_2$ by high permittivity (~21 at 100 kHz) sol-gel processed sodium β-alumina at 350 °C. The film of sodium β-alumina is smooth with the RMS roughness of 0.64 nm and the lattice oxygen of nearly ~53 %. The static performance parameters IZTO (In$_4$ZnSn$_4$O$_{15}$) TFTs with the architecture Si(p++) / sodium β-alumina / IZTO / Al are estimated to be μ_{sat}, I$_{on}$:I$_{off,}$ and V$_{th}$ of 4.21 ± 0.18 cm^2 V^{-1} s^{-1}, 1.4 × 10^2 and 0.47 ± 0.08 V respectively.

6.1 Scope for the future work

The results and analysis of the current study are aimed at the low temperature solution combustion of functional oxides with a fixed composition. The effect of doping percentage on the structural, compositional, and electrical characteristics has the scope for the future study. Also, the mechanistic approach towards the fabrication of combustion-derived thin films needs more understanding. Solution combustion can be explored to develop various functional metal oxides, like aluminium doped zinc oxide, fluorine doped zinc oxide or perovskites. Further, combustible precursor of metals can be extended to the development of composite films, metal alloys. Solution combustion

of bulk metal oxides powders is established over the years, but its mechanism in the fabrication of nanometre thick films is presently unclear. Understanding the same will guide the researchers to fetch more insight. Alternative doped metal oxides with low cost earth abundant systems such as zinc oxide, aluminium doped zinc oxides can have better opportunities in realizing ultra-low-cost transparent electronics.

APPENDIX I

Original designs of MESFET and MISFET
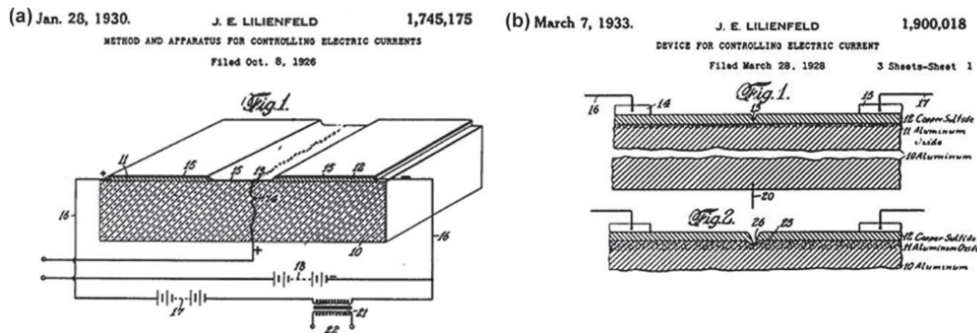
Figure I-a. Original designs of (a) MESFET (b) MISFET (Fortunato et al. 2012).

Device architecture and output characteristics reported by Weimer
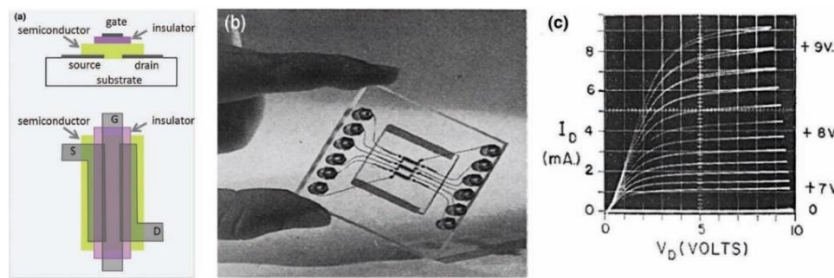
Figure I-b. (a) Device architecture, (b) actual device, and (c) output characteristics of the device first reported by Weimer (Fortunato et al. 2012).

Percentages of Scopus indexed articles
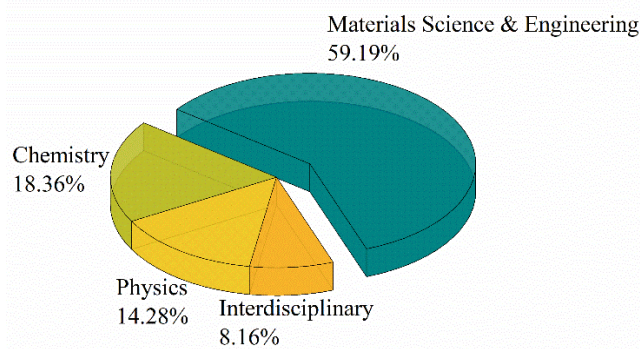
Figure I-c. Articles addressing combustion in thin films of nanometre thick by different branches of physical sciences.

APPENDIX II

XPS peak fitting: IZTO film surface

The XPS spectra was calibrated by carbon 1s (C 1s) peak centered at 284.7 eV. The C 1s peak fitting analysis is performed in order to determine the position of C-H/C-C peak so as to account for charge correction. Four synthetic peaks namely C-H/C-C (peak I), C-O (peak II), C=O (peak III), O-C=O (peak IV) were fit into the experimental data of C 1s by fixing Full Width Half Maximum (FWHM = 1.17), Gaussian-Lorentzian (GL) product peak positions relative to the main C-H/C-C peak. Table A-II provides the peak position constraints and parameters of deconvoluted peaks.

Table A-II: Peak fitting parameters of C 1s

Signatures of synthetic peaks	Position constraints	GL ratio	Positions (eV)	Area	% Area
C-H/C-C (peak I)	--				
		30	284.7	15758.91	84.44
C-O (peak II)	Peak I + 1.5 eV	30	286.2	1415.83	7.59
C=O (peak III)	Peak I + 3.0 eV	30	287.7	48.56	0.26
O=C-O (peak IV)	Peak I + 4.0 eV	30	288.7	1438.82	7.71

APPENDIX III

XPS peak fitting: sodium β-alumina film surface

The peak fitting procedure is same as that of AII. Table AIII gives the peak fitting parameters of C 1s.

Table A-III: Peak fitting parameters of C 1s (FWHM = 1.24)

Signatures of synthetic peaks	Position constraints	GL ratio	Positions (eV)	Area	% Area
C-H/C-C (peak I)	--	30	284.7	18318.06	72.53
C-O (peak II)	Peak I + 1.5 eV	30	286.2	3120.21	12.35
C=O (peak III)	Peak I + 3.0 eV	30	287.7	908.68	3.60
O=C-O (peak IV)	Peak I + 4.0 eV	30	288.8	2803.62	11.10
CO_3^{2-} (peak V)	Peak I + 4.5 eV	30	289.2	106.82	0.42
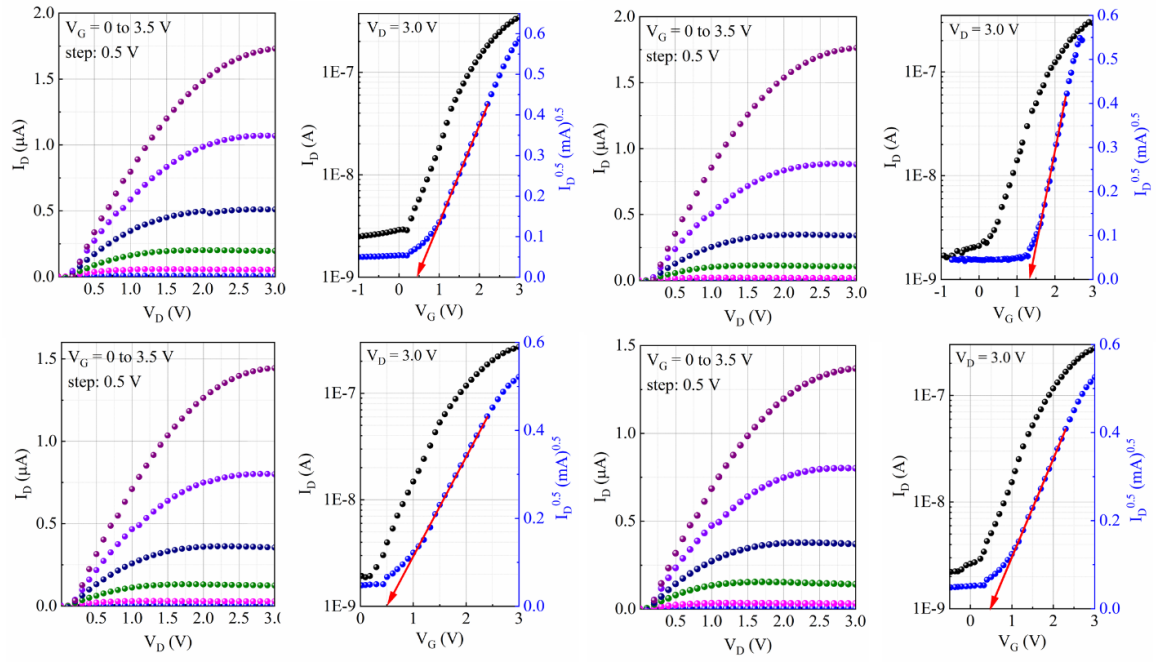
Fig. A-IV Output and transfer characteristics of the TFTs having sodium β-alumina dielectric with IZTO semiconductor

Page left intentionally blank

REFERENCES

Austin, I. and Mott, N. F. (1969). "Polarons in crystalline and non-crystalline materials." *Adv Phys.,* 18, 41-102.

Baeg, K. J., Khim, D., Kim, J., Han, H., Jung, S. W., Kim, T. W., Kang, M., Facchetti, A., Hong, S. K. and Kim, D. Y. (2012). "Controlled charge transport by polymer blend dielectrics in top-gate organic field-effect transistors for low-voltage-operating complementary circuits." *ACS Appl. Mater. Interfaces.,* 4, 6176-6184.

Banerjee, A. and Chattopadhyay, K. (2005). "Recent developments in the emerging field of crystalline p-type transparent conducting oxide thin films." *Prog. Cryst. Growth Charact. Mater.,* 50, 52-105.

Banger, K., Yamashita, Y., Mori, K., Peterson, R., Leedham, T., Rickard, J. and Sirringhaus, H. (2011). "Low-temperature, high-performance solution-processed metal oxide thin-film transistors formed by a 'sol–gel on chip' process." *Nat. Mater.,* 10, 45-50.

Baronetti, G. T., De miguel, S. R., Scelza, O. A. and Castro, A. A. (1986). "State of metallic phase in $PtSn/Al_2O_3$ catalysts prepared by different deposition techniques." *Appl. Catal., A.,* 24, 109-116.

Battistoni, C., Dormann, J., Fiorani, D., Paparazzo, E. and Viticoli, S. (1981). "An XPS and Mössbauer study of the electronic properties of $ZnCr_xGa_{2-x}O_4$ spinel solid solutions." *Solid State Commun.,* 39, 581-585.

Boesen, G. and Jacobs, J. E. (1968). "ZnO field-effect transistor." *Proceedings of the IEEE.,* 56, 2094-2095.

Branquinho, R., Salgueiro, D., Santos, L., Barquinha, P., Pereira, L., Martins, R. and Fortunato, E. (2014). "Aqueous combustion synthesis of aluminum oxide thin films and application as gate dielectric in GZTO solution-based TFTs." *ACS Appl. Mater. Interfaces.,* 6, 19592-19599.

Brinker, C. J. and Scherer, G. W. (2013). Sol-gel science: the physics and chemistry of sol-gel processing. *Academic press.*

Bong, J.K., Hung, J.K., Tae, S.Y., Yong, S.K., Doo, H.L., Youngmin, C. (2011). "Solution processed IZTO thin film transistor on silicon nitride dielectric layer." *J. Ind. Eng. Chem.,* 17, 96-99.

Bukke, R. N., Avis, C., Naik, M. N. and Jang, J. (2018). "Remarkable Increase in Field Effect Mobility of Amorphous IZTO Thin-Film Transistors With Purified ZrO_x Gate Insulator." *IEEE Electron Device Lett.,* 39, 371-374.

Burstein, E. (1954). "Anomalous optical absorption limit in InSb." *Phys. Rev.,* 93, 632-633.

Caironi, M. and Noh, Y. Y. (2015). Large area and flexible electronics. *John Wiley & Sons*.

Calnan, S. and Tiwari, A. (2010). "High mobility transparent conducting oxides for thin film solar cells." *Thin solid Films.,* 518, 1839-1849.

Carcia, P., Mclean, R., Reilly, M. and Nunes jr, G. (2003). "Transparent ZnO thin-film transistor fabricated by rf magnetron sputtering." *Appl. Phys. Lett.,* 82, 1117-1119.

Carlos, E., Branquinho, R., Kiazadeh, A., Barquinha, P., Martins, R. and Fortunato, E. (2016). "UV-Mediated Photochemical Treatment for Low-Temperature Oxide-Based Thin-Film Transistors." *ACS Appl. Mater. Interfaces.,* 8, 31100-31108.

Chang, Y. J., Lee, D. H., Herman, G. and Chang, C.-H. (2007). "High-performance, spin-coated zinc tin oxide thin-film transistors." *Electrochem. Solid-State Lett.,* 10, H135-H138.

Chen, X., Han, X. and Shen, Q. D. (2017). "PVDF-Based Ferroelectric Polymers in Modern Flexible Electronics." *Adv. Electron. Mater.,* 3, 1600460.

Chen, Y., Wang, B., huang, W., Zhang, X., Wang, G., Leonardi, M. J., Huang, Y., Lu, Z., Marks, T. J. and Facchetti, A. (2018a). "Nitroacetylacetone as a Cofuel for the Combustion Synthesis of High-Performance Indium–Gallium–Zinc Oxide Transistors." *Chem. Mater.,* 30, 3323-3329.

Chen, Y., Wang, B., Huang, W., Zhang, X., Wang, G., Leonardi, M. J., Huang, Y., Lu, Z., Marks, T. J. and Facchetti, A. (2018b). "Nitroacetylactone as a (co) Fuel for the Combustion Synthesis of High-Performance Indium-Gallium-Zinc Oxide Transistors." *Chem. Mater.,* 30, 3323-3329.

Choi, B., Im, H., Song, J. and Yoon, K. (1990). "Optical and electrical properties of Ga_2O_3 doped ZnO films prepared by rf sputtering." *Thin solid films.,* 193, 712-720.

Choi, H., Kim, S. H. and Jang, J. (2004). "Self-organized organic thin-film transistors on plastic." *Adv. Mater.,* 16, 732-736.

Chopra, K., Major, S. and Pandya, D. (1983). "Transparent conductors - a status review." *Thin solid films.,* 102, 1-46.

Clark, D., Fok, T., Roberts, G. and Sykes, R. (1980). "An investigation by electron spectroscopy for chemical analysis of chemical treatments of the (100) surface of n-type InP epitaxial layers for Langmuir film deposition." *Thin solid films.,* 70, 261-283.

Cochran, E. A., Park, D.-H., Kast, M. G., Enman, L. J., Perkins, C. K., Mansergh, R. H., Keszler, D. A., Johnson, D. W. and Boettcher, S. W. (2017). "Role of Combustion Chemistry in Low-Temperature Deposition of Metal Oxide Thin Films from Solution." *Chem. Mater.,* 29, 9480-9488.

De Wit, J., Vanunen, G. and Lahey, M. (1977). "Electron concentration and mobility in In_2O_3." *J. Phys. Chem. Solids*., 38, 819-824.

Deegan, R. D., Bakajin, O., Dupont, T. F., Huber, G., Nagel, S. R. and Witten, T. A. (1997). "Capillary flow as the cause of ring stains from dried liquid drops." *Nature.,* 389, 827-829.

Dekkers, M., Rijnders, G. and Blank, D. H. (2007). "$ZnIr_2O_4$, a p-type transparent oxide semiconductor in the class of spinel zinc-d 6-transition metal oxide." *Appl. Phys. Lett.,* 90, 021903.

Denton, E., Rawson, H. and Stanworth, J. (1954). "Vanadate glasses." *Nature.,* 173, 1030.

Dimitrakopoulos, C. D. and Malenfant, P. R. (2002). "Organic thin film transistors for large area electronics." *Adv. Mater.,* 14, 99-117.

Dimitrakopoulos, C. D. and Mascaro, D. J. (2001). "Organic thin-film transistors: A review of recent advances." *IBM Journal of Research and Development.* 45, 11-27.

Dippel, A.-C., Schneller, T., Gerber, P. and Waser, R. (2007). "Morphology control of highly-transparent indium tin oxide thin films prepared by a chlorine-reduced metallo-organic decomposition technique." *Thin Solid Films.,* 515, 3797-3801.

Dou, Y., Egdell, R., Walker, T., Law, D. and Beamson, G. (1998). "N-type doping in CdO ceramics: a study by EELS and photoemission spectroscopy." *Surf. Sci.,* 398, 241-258.

Edgar, L. J. (1930). "Method and apparatus for controlling electric currents." Google Patents.

Edgar, L. J. (1933). "Device for controlling electric current." Google Patents.

Everaerts, K., Zeng, L., Hennek, J. W., Camacho, D. I., Jariwala, D., Bedzyk, M. J., Hersam, M. C. and Marks, T. J. (2013). "Printed indium gallium zinc oxide transistors. Self-assembled nanodielectric effects on low-temperature combustion growth and carrier mobility." *ACS Appl. Mater. Interfaces.,* 5, 11884-11893.

Exarhos, G. J. and Zhou, X. D. (2007). "Discovery-based design of transparent conducting oxide films." *Thin Solid Films.,* 515, 7025-7052.

Faber, H., Lin, Y. H., Thomas, S. R., Zhao, K., Pliatsikas, N., Mclachlan, M. A., Amassian, A., Patsalas, P. A. and Anthopoulos, T. D. (2014). "Indium oxide thin-film transistors processed at low temperature via ultrasonic spray pyrolysis." *ACS Appl. Mater. Interfaces.,* 7, 782-790.

Facchetti, A. and Marks, T. (2010). Transparent electronics: from synthesis to applications. *John Wiley & Sons.*

Fan, J. C. and Goodenough, J. B. (1977). "X-ray photoemission spectroscopy studies of Sn-doped indium-oxide films." *J. Appl. Phys.,* 48, 3524-3531.

Fan, Z., Wang, D., Chang, P.-C., Tseng, W. Y. and L U, J. G. (2004). "ZnO nanowire field-effect transistor and oxygen sensing property." *Appl. Phys. Lett.,* 85, 5923-5925.

Fergus, J. (2003). "Doping and defect association in oxides for use in oxygen sensors." *J. Mater. Sci.,* 38, 4259-4270.

Fortunato, E., Barquinha, P. and Martins, R. (2012). "Oxide semiconductor thin-film transistors: a review of recent advances." *Adv. Mater.,* 24, 2945-2986.

Fortunato, E., Ginley, D., Hosono, H. and Paine, D. C. (2007). "Transparent conducting oxides for photovoltaics." *MRS bulletin.,* 32, 242-247.

Frank, G. and Köstlin, H. (1982). "Electrical properties and defect model of tin-doped indium oxide layers." *Appl. Phys. A.,* 27, 197-206.

Furubayashi, Y., Hitosugi, T., Yamamoto, Y., Inaba, K., Kinoda, G., Hirose, Y., Shimada, T. and Hasegawa, T. (2005). "A transparent metal: Nb-doped anatase TiO$_2$." *Appl. Phys. Lett.,* 86, 252101.

Gonzalez Aviles, G. B. (2003). "Studies on the defect structure of indium-tin oxide using X-ray and neutron diffraction." *ProQuest Dissertations And Theses, ISBN: 9780496356782.*

Gordon, L. (1952). "Precipitation from homogeneous solution." *Anal. Chem.,* 24, 459-462.

Gordon, L., Salutsky, M. L., Willard, H. H. and Rice, S. (1959). "Precipitation from homogeneous solution." *Phys. Today.,* 12, 60.

Gordon, R. G. (2000). "Criteria for choosing transparent conductors." *MRS bulletin.* 25, 52-57.

Gupta, A., Mandal, S., Katiyar, M. and Mohapatra, Y. N. (2012). "Film processing characteristics of nano gold suitable for conductive application on flexible substrates." *Thin Solid Films.* 520, 5664-5670.

Gupta, R., Ghosh, K., Mishra, S. and Kahol, P. (2008). "High mobility Ti-doped In_2O_3 transparent conductive thin films." *Mater. Lett..* 62, 1033-1035.

Hamberg, I., Granqvist, C. G., Berggren, K. F., Sernelius, B. E. and Engström, L. (1984). "Band-gap widening in heavily Sn-doped In_2O_3." *Phys. Rev. B.,* 30, 3240.

Hartnagel, H., Dawar, A., Jain, A. and Jagadish, C. (1995). Semiconducting transparent thin films. *Institute of Physics Bristol.*

Harvey, S. P., Mason, T. O., Buchholz, D. B., Chang, R. P., Körber, C. and Klein, A. (2008a). "Carrier Generation and Inherent Off-Stoichiometry in Zn, Sn Codoped Indium Oxide (ZITO) Bulk and Thin-Film Specimens." *J. Am. Ceram. Soc.,* 91, 467-472.

Harvey, S. P., poeppelmeier, K. R. and Mason, t. O. (2008b). "Subsolidus Phase Relationships in the ZnO–In_2O_3–SnO_2 system." *J. Am. Ceram. Soc.,* 91, 3683-3689.

Hennek, J. W., Kim, M. G., Kanatzidis, M. G., Facchetti, A. and Marks, T. J. (2012). "Exploratory combustion synthesis: Amorphous indium yttrium oxide for thin-film transistors." *J. Am. Chem. Soc.,* 134, 9593-9596.

Hennek, J. W., Smith, J., Yan, A., Kim, M. G., Zhao, W., Dravid, V. P., Facchetti, A. and Marks, T. J. (2013). "Oxygen "getter" effects on microstructure and carrier transport in low temperature combustion-processed a-$In_x ZnO$ (x = Ga, Sc, Y, La) transistors." *J. Am. Chem. Soc.,* 135, 10729-10741.

Heo, J. H., Jung, K. Y., Kwak, D. J., Lee, D. K. and Sung, Y. M. (2009). "Fabrication of titanium-doped indium oxide films for dye-sensitized solar cell application using reactive RF magnetron sputter method." *IEEE Transactions on Plasma Science.* 37, 1586-1592.

Heward, W. J. and Swenson, D. J. (2007). "Phase equilibria in the pseudo-binary In_2O_3-SnO_2 system." *J. Mater. Sci.,* 42, 7135-7140.

Hodes, G. (2002). Chemical solution deposition of semiconductor films. *CRC press, Boca Raton.*

Hoel, C. A., Mason, T. O., Gaillard, J. F. and Poeppelmeier, K. R. (2010). "Transparent conducting oxides in the ZnO-In_2O_3-SnO_2 system." *Chem. Mater.,* 22, 3569-3579.

Hosono, H. (2006). "Ionic amorphous oxide semiconductors: Material design, carrier transport, and device application." *J. Non-Cryst. Solids.,* 352, 851-858.

Hosono, H., Kamiya, T. and Hirano, M. (2006). "Function cultivation of transparent oxides utilizing built-in nanostructure." *Bull. Chem. Soc. Jpn.,* 79, 1-24.

Hosono, H., Nomura, K., Ogo, Y., Uruga, T. and Kamiya, T. (2008). "Factors controlling electron transport properties in transparent amorphous oxide semiconductors." *J. Non-Cryst. Solids.,* 354, 2796-2800.

Hosono, H., Yamashita, Y., Ueda, N., Kawazoe, H. and Shimidzu, K. I. (1996a). "New amorphous semiconductor: $2CdO·PbO_x$." *Appl. Phys. Lett.,* 68, 661-663.

Hosono, H., Yasukawa, M. and Kawazoe, H. (1996b). "Novel oxide amorphous semiconductors: Transparent conducting amorphous oxides." *J. Non-Cryst. Solids.,* 203, 334-344.

Hu, H. and Larson, R. G. (2006). "Marangoni effect reverses coffee-ring depositions." *J. Phys. Chem. B.,* 110, 7090-7094.

Hu, J. and Gordon, R. G. (1991). "Textured fluorine-doped ZnO films by atmospheric pressure chemical vapor deposition and their use in amorphous silicon solar cells." *Sol. cells.,* 30, 437-450.

Hu, J. and Gordon, R. G. (1992). "Textured aluminum-doped zinc oxide thin films from atmospheric pressure chemical-vapor deposition." *J. Appl. Phys.,* 71, 880-890.

Huang, H. C. and Hsieh, T. E. (2010). "Highly stable precursor solution containing ZnO nanoparticles for the preparation of ZnO thin film transistors." *Nanotechnology.,* 21, 295707.

Jain, S., Adiga, K. and Verneker, V. P. (1981). "A new approach to thermochemical calculations of condensed fuel-oxidizer mixtures." *Combust. Flame.,* 40, 71-79.

Jeong, S., Lee, J. Y., Lee, S. S., Choi, Y. and Ryu, B. H. (2011). "Impact of metal salt precursor on low-temperature annealed solution-derived Ga-doped In_2O_3 semiconductor for thin-film transistors." *J. Phys. Chem. C.,* 115, 11773-11780.

Jin, S., Yang, Y., Medvedeva, J. E., Ireland, J. R., Metz, A. W., Ni, J., Kannewurf, C. R., Freeman, A. J. and Marks, T. J. (2004). "Dopant ion size and electronic structure effects on transparent conducting oxides. Sc-doped CdO thin films grown by MOCVD." *J. Am. Chem. Soc.,* 126, 13787-13793.

Jin, S., Yang, Y., Medvedeva, J. E., Wang, L., Li, S., Cortes, N., Ireland, J. R., Metz, A. W., Ni, J. and Hersam, M. C. (2007). "Tuning the properties of transparent oxide conductors. Dopant ion size and electronic structure effects on CdO-based transparent conducting oxides. Ga-and In-doped CdO thin films grown by MOCVD." *Chem. Mater.,* 20, 220-230.

Kagan, C., Mitzi, D. and Dimitrakopoulos, C. (1999). "Organic-inorganic hybrid materials as semiconducting channels in thin-film field-effect transistors." *Science.,* 286, 945-947.

Kamiya, T. and Hosono, H. (2005). "Creation of new functions in transparent oxides utilizing nanostructures embedded in crystal and artificially encoded by laser pulses." *Semicond. Sci. Technol.,* 20, S92.

Kamyshny, A., Benmoshe, M., Aviezer, S. and Magdassi, S. (2005). "Ink-Jet Printing of Metallic Nanoparticles and Microemulsions." *Macromol. Rapid Commun.,* 26, 281-288.

Kamyshny, A. and Magdassi, S. (2014). "Conductive nanomaterials for printed electronics." *Small.,* 10, 3515-3535.

Kang, Y. H., Jeong, S., Ko, J. M., Lee, J. Y., Choi, Y., Lee, C. and Cho, S. Y. (2014). "Two-component solution processing of oxide semiconductors for thin-film transistors via self-combustion reaction." *J. Mater. Chem. C.,* 2, 4247-4256.

Kawazoe, H., Yanagi, H., Ueda, K. and Hosono, H. (2000). "Transparent p-type conducting oxides: design and fabrication of pn heterojunctions." *MRS bulletin.,* 25, 28-36.

Kawazoe, H., Yasukawa, M., Hyodo, H., Kurita, M., Yanagi, H. and Hosono, H. (1997). "P-type electrical conduction in transparent thin films of $CuAlO_2$." *Nature.,* 389, 939.

Khastgir, D., Maiti, H. and Bandyopadhyay, P. (1988). "Polystyrene-titania composite as a dielectric material." *Mater. Sci. Eng.,* 100, 245-253.

Kim, H., Gilmore, C., Pique, A., Horwitz, J., Mattoussi, H., Murata, H., Kafafi, Z. and Chrisey, D. (1999). "Electrical, optical, and structural properties of indium–tin–oxide thin films for organic light-emitting devices." *J. Appl. Phys.,* 86, 6451-6461.

Kim, M. G., Kanatzidis, M. G., Facchetti, A. and Marks, T. J. (2011b). "Low-temperature fabrication of high-performance metal oxide thin-film electronics via combustion processing." *Nat. Mater.,* 10, 382-388.

Kim, M. G., Kim, H. S., Ha, Y. G., He, J., Kanatzidis, M. G., Facchetti, A. and Marks, T. J. (2010). "High-performance solution-processed amorphous zinc− indium− tin oxide thin-film transistors." *J. Am. Chem. Soc.,* 132, 10352-10364.

Kim, M., Jeong, J. H., Lee, H. J., Ahn, T. K., Shin, H. S., Park, J. S., Jeong, J. K., Mo, Y. G. and Kim, H. D. (2007). "High mobility bottom gate InGaZnO thin film transistors with SiOx etch stopper." *Appl. Phys. Lett.,* 90, 212114.

Kim, S. H., Hong, K., Xie, W., Lee, K. H., Zhang, S., Lodge, T. P. and Frisbie, C. D. (2013a). "Electrolyte-gated transistors for organic and printed electronics." *Adv. Mater.,* 25, 1822-1846.

Kim, S. Y., Ahn, C. H., Lee, J. H., Kwon, Y. H., Hwang, S., Lee, J. Y. and Cho, H. K. (2013b). "p-Channel oxide thin film transistors using solution-processed copper oxide." *ACS Appl. Mater. Interfaces.,* 5, 2417-2421.

Kim, Y. H., Heo, J. S., Kim, T. H., Park, S., Yoon, M. H., Kim, J., Oh, M. S., Yi, G. R., Noh, Y. Y. and Park, S. K. (2012). "Flexible metal-oxide devices made by room-temperature photochemical activation of sol–gel films." *Nature.,* 489, 128.

Klasens, H. and Koelmans, H. (1964). "A tin oxide field-effect transistor." *Solid State Electron.,* 7, 701-702.

Lany, S. and Zunger, A. (2007). "Dopability, intrinsic conductivity, and nonstoichiometry of transparent conducting oxides." *Phys. Rev. Lett.,* 98, 045501.

Lee, D. H., Chang, Y. J., Stickle, W. and Chang, C. H. (2007). "Functional porous tin oxide thin films fabricated by inkjet printing process." *Electrochem. Solid-State Lett.,* 10, K51-K54.

Lee, J. H., Kim, S. H., Kim, G. H., Lim, S. C., Lee, H., Jang, J. and Zyung, T. (2003). "Pentacene thin film transistors fabricated on plastic substrates." *Synth. Met.,* 139, 445-451.

Lee, S. W. and Joo, S. K. (1996). "Low temperature poly-Si thin-film transistor fabrication by metal-induced lateral crystallization." *IEEE Electron Device Lett.,* 17, 160-162.

Lewis, J. A. (2000). "Colloidal processing of ceramics." *J. Am. Ceram. Soc.,* 83, 2341-2359.

Li, C., Li, Y., Wu, Y., Ong, B. S. and Loutfy, R. O. (2007). ZnO field-effect transistors prepared by aqueous solution-growth ZnO crystal thin film. *AIP.,* 102, 076101

Liu, A., Zhu, H., Sun, H., Xu, Y. and Noh, Y. Y. (2018). "Solution Processed Metal Oxide High-κ Dielectrics for Emerging Transistors and Circuits." *Adv. Mater.,* 1706364.

Liu, Y., Guan, P., Zhang, B., Falk, M. L. and Katz, H. E. (2013). "Ion dependence of gate dielectric behavior of alkali metal ion-incorporated aluminas in oxide field-effect transistors." *Chem. Mater.,* 25, 3788-3796.

Lu, X., Lemmon, J. P., Sprenkle, V. and YANG, Z. (2010). "Sodium-beta alumina batteries: status and challenges." *The Journal of The Minerals, Metals & Materials Society.,* 62, 31-36.

Magdassi, S. (2010). "In the chemistry of inkjet inks." *Magdassi, S., Ed. World Scientific Publishing Co. Pte. Ltd.: Hackensack, NJ.*

Mamazza, R., Morel, D. L. and Ferekides, C. S. (2005). "Transparent conducting oxide thin films of Cd_2SnO_4 prepared by RF magnetron co-sputtering of the constituent binary oxides." *Thin Solid Films.* 484, 26-33.

Manjunath, G., Anusha, P., Salian, A., Gupta, B. and Mandal, S. (2018). "Effect of O_2, N_2 and H_2 on annealing of pad printed high conductive Ag-Cu nano-alloy electrodes." *Mater Res Express.,* 5, 014014.

Marezio, M. (1966). "Refinement of the crystal structure of In_2O_3 at two wavelengths." *Acta Crystallogr.,* 20, 723-728.

Martins, R., Raniero, L., Pereira, L., Costa, D., Aguas, H., Pereira, S., Silva, L., Gonçalves, A., Ferreira, I. and Fortunato, E. (2009). "Nanostructured silicon and its application to solar cells, position sensors and thin film transistors." *Philosophical Magazine.* 89, 2699-2721.

Mason, T., Gonzalez, G., Kammler, D., Mansourianhadavi, N. and Ingram, B. (2002). "Defect chemistry and physical properties of transparent conducting oxides in the $CdO-In_2O_3-SnO_2$ system." *Thin Solid Films.* 411, 106-114.

Medvedeva, J. E. (2006). "Magnetically mediated transparent conductors: In_2O_3 doped with Mo." *Phys. Rev. Lett.,* 97, 086401.

Medvedeva, J. E. (2007). "Unconventional approaches to combine optical transparency with electrical conductivity." *Appl. Phys. A.,* 89, 43-47.

Medvedeva, J. E. and Hettiarachchi, C. L. (2010). "Tuning the properties of complex transparent conducting oxides: Role of crystal symmetry, chemical composition, and carrier generation." *Phys. Rev. B.* 81, 125116.

Meyers, S. T., Anderson, J. T., Hung, C. M., Thompson, J., Wager, J. F. and Keszler, D. A. (2008). "Aqueous inorganic inks for low-temperature fabrication of ZnO TFTs." *J. Am. Chem. Soc.,* 130, 17603-17609.

Minami, T. (2000). "New n-type transparent conducting oxides." *MRS bulletin.* 25, 38-44.

Morozova, L. and Komarov, A. (1995). "Solid solutions based on cadmium oxide in the CdO-In_2O_3 system." *Russ. J. Appl. Chem.,* 68, 1240-1242.

Moss, T. (1954). "The interpretation of the properties of indium antimonide." *Proceedings of the Physical Society. Section B.* 67, 775.

Mryasov, O. and Freeman, A. (2001). "Electronic band structure of indium tin oxide and criteria for transparent conducting behavior." *Phys. Rev. B.* 64, 233111.

Nomura, K., Kamiya, T., Ohta, H., Shimizu, K., Hirano, M. and Hosono, H. (2008). "Relationship between non-localized tail states and carrier transport in amorphous oxide semiconductor, In–Ga–Zn–O." *Phys. Status Solidi A.,* 205, 1910-1914.

Nomura, K., Ohta, H., Takagi, A., Kamiya, T., Hirano, M. and Hosono, H. (2004). "Room-temperature fabrication of transparent flexible thin-film transistors using amorphous oxide semiconductors." *Nature.* 432, 488-492.

Norris, B., Anderson, J., Wager, J. and Keszler, D. (2003). "Spin-coated zinc oxide transparent transistors." *J. Phys. D: Appl. Phys.,* 36, L105.

Ohta, H. and Hosono, H. (2004). "Transparent oxide optoelectronics." *Mater. Today.,* 7, 42-51.

Okamura, H. and Bowen, H. K. (1986). "Preparation of alkoxides for the synthesis of ceramics." *Ceram. Int.,* 12, 161-171.

Orita, M., Ohta, H., Hirano, M., Narushima, S. and Hosono, H. (2001). "Amorphous transparent conductive oxide $InGaO_3(ZnO)_m$ ($m \leq 4$): a-Zn4s conductor." *Philosophical magazine B.* 81, 501-515.

Ortiz, R. P., Facchetti, A. and Marks, T. J. (2009). "High-k organic, inorganic, and hybrid dielectrics for low-voltage organic field-effect transistors." *Chem. Rev.,* 110, 205-239.

Owings, R. R., Exarhos, G. J., Windisch, C. F., Holloway, P. H. and Wen, J. G. (2005). "Process enhanced polaron conductivity of infrared transparent nickel–cobalt oxide." *Thin Solid Films.* 483, 175-184.

Pal, B. N., Dhar, B. M., See, K. C. and Katz, H. E. (2009). "Solution-deposited sodium beta-alumina gate dielectrics for low-voltage and transparent field-effect transistors." *Nature Mater.,* 8, 898-903.

Palmer, G., Poeppelmeier, K. and Mason, T. (1997a). "Conductivity and transparency of ZnO/SnO_2-cosubstituted In_2O_3." *Chem. Mater.,* 9, 3121-3126.

Palmer, G., Poeppelmeier, K. R. and Mason, T. O. (1997b). "$Zn_{2-x}Sn_{1-x}In_{2x}O_{4-\delta}$: An indium-substituted spinel with transparent conducting properties." *J. Solid State Chem.,* 134, 192-197.

Park, K. B., Seon, J. B., Kim, G. H., Yang, M., Koo, B., Kim, H. J., Ryu, M. K. and Lee, S. Y. (2010). "High electrical performance of wet-processed indium zinc oxide thin-film transistors." *IEEE Electron Device Lett.,* 31, 311-313.

Park, S. K., Kim, Y. H., Kim, H. S. and Han, J. I. (2009). "High performance solution-processed and lithographically patterned zinc–tin oxide thin-film transistors with good operational stability." *Electrochem. Solid-State Lett.,* 12, H256-H258.

Parthiban, S., Gokulakrishnan, V., Elangovan, E., Goncalves, G., Ramamurthi, K., Fortunato, E. and Martins, R. (2012). "High mobility and visible–near infrared transparent titanium doped indium oxide thin films produced by spray pyrolysis." *Thin Solid Films.* 524, 268-271.

Pasquarelli, R. M., Ginley, D. S. and Ohayre, R. (2011). "Solution processing of transparent conductors: from flask to film." *Chem. Soc. Rev.,* 40, 5406-5441.

Patil, K., Hegde, M., Rattan, T. and Aruna, S. (2008a). "Chemistry of nanocrystalline oxide materials-combustion synthesis, properties and applications." *World Scientific Publishing Co. Pte. Ltd. Singapore*.

Pechini, M. P. (1967). "Method of preparing lead and alkaline earth titanates and niobates and coating method using the same to form a capacitor." Google Patents.

Perednis, D. and Gauckler, L. J. (2005). "Thin film deposition using spray pyrolysis." *J. Electroceramics.* 14, 103-111.

Perelaer, J., Smith, P. J., Mager, D., Soltman, D., Volkman, S. K., Subramanian, V., Korvink, J. G. and Schubert, U. S. (2010). "Printed electronics: the challenges involved in printing devices, interconnects, and contacts based on inorganic materials." *J. Mater. Chem.,* 20, 8446-8453.

Pierre, A. C. 1998. General Introduction. "Introduction to Sol-Gel Processing." *Springer, Boston MA*.

Pinna, N. and Niederberger, M. (2008). "Surfactant-free nonaqueous synthesis of metal oxide nanostructures." *Angew. Chem.,* 47, 5292-5304.

Prins, M., Grosse-holz, K. O., Müller, G., Cillessen, J., Giesbers, J., Weening, R. and Wolf, R. (1996). "A ferroelectric transparent thin-film transistor." *Appl. Phys. Lett.,* 68, 3650-3652.

Rakhshani, A., Makdisi, Y. and Ramazaniyan, H. (1998). "Electronic and optical properties of fluorine-doped tin oxide films." *J. Appl. Phys.,* 83, 1049-1057.

Reed, T. B. (1971). "Free energy of formation of binary compounds: an atlas of charts for high-temperature chemical calculations." *Biomass Energy Foundation Press*.

Roth, A. and Williams, D. (1981). "Properties of zinc oxide films prepared by the oxidation of diethyl zinc." *J. Appl. Phys.,* 52, 6685-6692.

Salgueiro, D., Kiazadeh, A., Branquinho, R., Santos, L., Barquinha, P., Martins, R. and Fortunato, E. (2017). "Solution based zinc tin oxide TFTs: the dual role of the organic solvent." *J. Phys. D: Appl. Phys.,* 50, 065106.

Salian, A., Pujar, P. and Mandal, S. (2019). "Facile in situ formation of high conductive Ag and Cu_xO_y composite films: a role of aqueous spray combustion." *J. Mater. Sci.: Mater. Electron.* 30, 2888-2897.

Sanchez-rodriguez, D., Farjas, J., Roura, P., Ricart, S., Mestres, N., Obradors, X. and Puig, T. (2013). "Thermal analysis for low temperature synthesis of oxide thin films from chemical solutions." *J. Phys. Chem. C.,* 117, 20133-20138.

Sanctis, S., Hoffmann, R. C., Koslowski, N., Foro, S., Bruns, M. and Schneider, J. J. (2018). "Aqueous Solution Processing of Combustible Precursor Compounds into Amorphous Indium Gallium Zinc Oxide (IGZO) Semiconductors for Thin Film Transistor Applications." *Chemistry-An Asian Journal.,* 13, 3912-3919.

Schmalzried, H. (1964). "FA Kröger: The Chemistry of Imperfect Crystals, North-Holland Publishing Company-Amsterdam 1964. 1039 Seiten. Preis: *Berichte der Bunsengesellschaft für physikalische Chemie.* 68, 608-608.

Schneller, T., Waser, R., Kosec, M. and Payne, D. (2013). Chemical solution deposition of functional oxide thin films. *Springer Vienna.*

Schroder, D. K. (2006). Semiconductor material and device characterization. *John Wiley & Sons.*

Seager, C., Mcintyre, D., Warren, W. and Tuttle, B. (1996). "Charge trapping and device behavior in ferroelectric memories." *Appl. Phys. Lett.,* 68, 2660-2662.

Seo, D. J. and Park, S. H. (2005). "Structural, electrical and optical properties of In_2O_3:Mo films deposited by spray pyrolysis." *Physica B: Condensed Matter.,* 357, 420-427.

Shaw, J. M. and Seidler, P. F. (2001). "Organic electronics: introduction." *IBM Journal of Research and Development.* 45, 3-9.

Soltman, D., Smith, B., Kang, H., Morris, S. and SubramaniaN, V. (2010). "Methodology for inkjet printing of partially wetting films." *Langmuir.,* 26, 15686-15693.

Soltman, D. and Subramanian, V. (2008). "Inkjet-printed line morphologies and temperature control of the coffee ring effect." *Langmuir.,* 24, 2224-2231.

Spear, W. and Lecomber, P. (1975). "Substitutional doping of amorphous silicon." *Solid State Commun.,* 17, 1193-1196.

Talapin, D. V., Lee, J. S., Kovalenko, M. V. and Shevchenko, E. V. (2009). "Prospects of colloidal nanocrystals for electronic and optoelectronic applications." *Chem. Rev.,* 110, 389-458.

Tickle, A. T. (1969). "An Approach to Microelectronics." *Wiley, New York.*

Todorov, T. K., Reuter, K. B. and Mitzi, D. B. (2010). "High-efficiency solar cell with earth-abundant liquid-processed absorber." *Adv. Mater.,* 22, E156-E159.

Van Hest, M., Dabney, M., Perkins, J. and Ginley, D. (2006). "High-mobility molybdenum doped indium oxide." *Thin Solid Films.,* 496, 70-74.

Van Hest, M., Dabney, M., Perkins, J., Ginley, D. and Taylor, M. (2005). "Titanium-doped indium oxide: A high-mobility transparent conductor." *Appl. Phys. Lett.,* 87, 032111.

Varma, A., Mukasyan, A. S., Rogachev, A. S. and Manukyan, K. V. (2016). "Solution combustion synthesis of nanoscale materials." *Chem. Rev.,* 116, 14493-14586.

Vegard, L. (1921). "Die konstitution der mischkristalle und die raumfüllung der atome." *Zeitschrift für Physik*. 5, 17-26.

Vuillaume, D., Boulas, C., Collet, J., Davidovits, J. and Rondelez, F. (1996). "Organic insulating films of nanometer thicknesses." *Appl. Phys. Lett.,* 69, 1646-1648.

Wager, J. F. (2014). "Flat-Panel-Display Backplanes: LTPS or IGZO for AMLCDs or AMOLED Displays?" *Information Display*. 30, 26-29.

Wager, J. F. (2016). "Oxide TFTs: A progress report." *Information Display.,* 32, 16-21.

Wallmark, J. T. and Johnson, H. (1966). "Field-effect Transistors: Physics, Technology and Aplications." *Prentice Hall*.

Wang, B., Yu, X., Guo, P., Huang, W., Zeng, L., Zhou, N., Chi, L., Bedzyk, M. J., Chang, R. P. and Marks, T. J. (2016a). "Solution-Processed All-Oxide Transparent High-Performance Transistors Fabricated by Spray-Combustion Synthesis." *Adv. Electron. Mater.,* 2, 1500427.

Wang, B., Zeng, L., Huang, W., Melkonyan, F. S., Sheets, W. C., Chi, L., Bedzyk, M. J., Marks, T. J. and Facchetti, A. (2016b). "Carbohydrate-Assisted Combustion Synthesis To Realize High-Performance Oxide Transistors." *J. Am. Chem. Soc.,* 138, 7067-7074.

Wang, Z., Nayak, P. K., Caraveo-Frescas, J. A. and Alshareef, H. N. (2016c). "Recent developments in p-Type oxide semiconductor materials and devices." *Adv. Mater.*. 28, 3831-3892.

Weimer, P. K. (1962). "The TFT a new thin-film transistor." *Proceedings of the IRE*. 50, 1462-1469.

Westin, G., Kritikos, M. and Wijk, M. (1998). "Synthesis and properties of erbium isopropoxides: Structural characterization of $Er_5O(OPr^i)_{13}$." *J. Solid State Chem.,* 141, 168-176.

Wong, H. (2011). Nano-CMOS gate dielectric engineering. CRC Press.

Wyckoff, R. (1963). "Interscience Publishers, New York, New York rocksalt structure." *Crystal structures.,* 1, 85-237.

Xiong, G., Jones, G., Rungsawang, R. and Anderson, D. (2010). "Non-aqueous solution processed ZnO thin film transistors." *Thin Solid Films.,* 518, 4019-4023.

Yang, H. and Jiang, P. (2010). "Large-scale colloidal self-assembly by doctor blade coating." *Langmuir.,* 26, 13173-13182.

Yang, J., Wang, B., Zhang, Y., Ding, X. and Zhang, J. (2018). "Low-temperature combustion synthesis and UV treatment processed p-type Li:NiO$_x$ active semiconductors for high-performance electronics." *J. Mater. Chem. C*., 6, 12584-12591.

Yang, Y., Jin, S., Medvedeva, J. E., Ireland, J. R., Metz, A. W., NI, J., Hersam, M. C., Freeman, A. J. and Marks, T. J. (2005). "CdO as the archetypical transparent conducting oxide. Systematics of dopant ionic radius and electronic structure effects on charge transport and band structure." *J. Am. Chem. Soc.,* 127, 8796-8804.

Yasukawa, M., Hosono, H., Ueda, N. and Kawazoe, H. (1995). "Novel transparent and electroconductive amorphous semiconductor: Amorphous AgSbO$_3$ film." *Jpn. J. Appl. Phys.,* 34, L281.

Yu, X., Smith, J., Zhou, N., Zeng, L., Guo, P., Xia, Y., Alvarez, A., Aghion, S., Lin, H. and Yu, J. (2015). "Spray-combustion synthesis: Efficient solution route to high-performance oxide transistors." *Proceedings of the National Academy of Sciences.,* 112, 3217-3222.

Zhang, B., Liu, Y., Agarwal, S., Yeh, M. L. and Katz, H. E. (2011). "Structure, sodium ion role, and practical issues for β-alumina as a high-k solution-processed gate layer for transparent and low-voltage electronics." *ACS Appl. Mater. Interfaces.,* 3, 4254-4261.

Zhang, D., Li, C., Han, S., Liu, X., Tang, T., Jin, W. and Zhou, C. (2003). "Electronic transport studies of single-crystalline In2O3 nanowires." *Appl. Phys. Lett.,* 82, 112-114.

Zhou, Y., Han, S. T., Xu, Z. X. and Roy, V. (2012). "Polymer–nanoparticle hybrid dielectrics for flexible transistors and inverters." *J. Mater. Chem.,* 22, 4060-4065.

Page left intentionally blank

LIST OF PUBLICATIONS

PATENTS

Pavan Pujar, Komalakrushna Hadagalli, Shakya Kaushal Rajendraprasad, Dipti Gupta, Saumen Mandal, "Method and system for fabricating a porous ceramic structure using combustible pore former," Indian patent. Application Number: 201841033533, filed on 6th September 2018.

Saumen Mandal, Bikesh Gupta, **Pavan Pujar**, Komalakrushna Hadagalli, Robbi Vivek Vardhan, "Fabrication of High Conductive Metallic Films at Low Temperature," Indian Patent. Application Number: 201741005384, published on 17th August 2018.

PUBLICATIONS IN PEER-REVIEWED JOURNALS

Pavan Pujar, Srinivas Gandla, Mukesh Singh, Bikesh Gupta, Kartick Tarafder, Dipti Gupta, Yong-Young Noh and Saumen Mandal, 'Development of low temperature stoichiometric solution combustion derived transparent conductive ternary zinc tin co-doped indium oxide electrodes,' RSC Advances 7 (2017) 48253.

Pavan Pujar, Robbi Vivek Vardhan, Dipti Gupta, Saumen Mandal, 'A balancing between super transparency and conductivity of solution combustion derived titanium doped indium oxide: effect of charge carrier density and mobility,' Thin Solid Films 660 (2018) 267.

Pavan Pujar, P. Anusha, Dipti Gupta, Saumen Mandal, 'Investigation of sintering kinetics and morphological evolution of silver films from nano-dispersion,' Applied Physics A: Materials Science & Processing 124 (2018) 831.

Pavan Pujar, Dipti Gupta, Saumen Mandal, 'High-performance low voltage operation of indium zinc tin oxide thin film transistors using chemically derived sodium β-alumina dielectric', Journal of Materials Science: Materials in Electronics 30 (2019) 9097.

Pavan Pujar, Bikesh Gupta, Pradyut Sengupta, Dipti Gupta, Saumen Mandal, 'Sodium incorporated alumina - A versatile anisotropic ceramic', Journal of the European Ceramic Society 39 (2019) 4473.

CONFERENCE PRESENTATIONS

Pavan Pujar, Kartick Tarafder, Dipti Gupta, Yong-Young Noh and Saumen Mandal, 'Zinc and tin co-doped ternary indium oxide as a transparent conducting oxide developed through combustible precursor with a minimal thermal investment' International Union of Material Research Societies-International Conference on Electronic Materials (IUMRS-ICEM) 2018, Daejeon, South Korea (Oral presentation).

Pavan Pujar, Ashritha Salian, Bikesh Gupta, Majunath G, Dipti Gupta, Saumen Mandal 'Distinct technologies featuring nanoparticles and molecular precursors of silver to deposit electrodes for optoelectronic devices,' Fourth International Conference on Nanomaterials: Synthesis, Characterization and Applications 2019, Mahatma Gandhi University, Kottayam, India (Invited talk).

Pavan Pujar, Dipti Gupta and Saumen Mandal 'Compositionally altered zinc and tin co-doped indium oxide as both transparent conductor and semiconductor for optoelectronic devices' Advanced Ceramics and Nanomaterials for Sustainable Development (ACeND) 2018, Bengaluru, India (Oral presentation).

Pavan Pujar, Mayur Goti, Kartick Tarafder and Saumen Mandal, 'Formulation of amorphous Indium Zinc Tin Oxide nanoparticles based semiconducting ink using auto-combustion synthesis,' International Conference on Ceramic and Advanced Materials for Energy and Environment (CAMEE) 2015, Bengaluru, India (Oral presentation).

Pavan Pujar, Bikesh Gupta, Vandana Singh, Kartick Tarafder, Dipti Gupta, Saumen Mandal 'Low temperature fabrication of tin doped indium oxide transparent thin films through solution combustion processing without an external fuel,' International conference (ICRAN) 2016, Delhi, India (poster presentation).

BIO DATA

Name	:	Pavan Pujar
Father's name	:	Bhimasen
Date of birth	:	24th December 1990
Permanent address	:	Mantralaya Niwas
		Near Rayar Math
		Malmaddi
		Dharwad – 580007
		Karnataka, India.
Mobile	:	+91-9591705032
E-mail	:	p.b.pujar@gmail.com

Academic qualification:

Bachelor of Engineering (B.E.) in Mechanical Engineering from Basaveshwar Engineering College Bagalkot, Karnataka (CGPA: 9.21 out of 10).

Masters of Technology (M.Tech.) in Materials Engineering from National Institute of Technology Karnataka (NITK) Surathkal (CGPA: 9.14 out of 10).